IMAGING CHARGE CARRIER AND ACOUSTIC PHONON DYNAMICS IN SEMICONDUCTOR NANOMATERIALS USING ULTRAFAST PUMP-PROBE MICROSCOPY

Erika Marie Van Goethem

A dissertation submitted to the faculty of the University of North Carolina at Chapel Hill in partial fulfillment of the requirements for the degree of Doctor of Philosophy in the Department of Chemistry in the College of Arts and Sciences.

Chapel Hill
2018

Approved by:

John M. Papanikolas

Joanna M. Atkin

James F. Cahoon

Andrew M. Moran

Scott C. Warren

ABSTRACT

Erika Marie Van Goethem: Imaging Charge Carrier and Acoustic Phonon Dynamics in
Semiconductor Nanomaterials using Ultrafast Pump-Probe Microscopy
(Under the direction of John M. Papanikolas)

Future advancement of nanotechnology is dependent on our capabilities to design novel

and ever increasingly complex nanomaterials. In order to manipulate the electronic and optical

properties of these materials in an efficient way, we need a fundamental understanding of the

physics of how structural features alter the properties of these nanomaterials. Nanostructures that

are produced under identical conditions can have vastly different properties, and they can even

have variations among different spatial locations within the same structure.   This heterogeneity

can have a significant impact on the properties, dynamics, and performance of nanoscale devices.

As a result, it is important to understand dynamics in individual nanostructures. Most analytical

techniques, however, probe dynamics in an ensemble of structures and thereby obscuring

dynamics and making quantitative conclusions difficult.

Pump-probe microscopy overcomes these limitations by combining the high-temporal

resolution of pump-probe spectroscopy and the high-spatial resolution of optical microscopy.

With combined spatial and temporal resolution, the microscope collects data from spatially

distinct locations on individual nanostructures with a high throughput. Additionally, using

computer controlled scanning mirrors with the microscope allows us to spatially separate the

excitation and probe spots at the sample to allow the direct visualization of charge carrier and

acoustic lattice motion on the nanoscale without the need for physical contact or active electrical connection.

Here, this microscope has been used to image electron diffusion and thermal transport, as well as acoustic phonon propagation in germanium nanowires. Additionally, it has been employed to study exciton and free charge carrier dynamics in tungsten disulfide and tungsten diselenide nanoflakes. The propagation of a shear mode is captured in suspended tungsten diselenide nanoflakes using the spatially-separated pump-probe imaging configuration.

To my parents, I couldn't have done this without you.

Thank you for all your love and support along the way.

ACKNOWLEDGMENTS

I would like to express my deepest gratitude to my research advisor, Dr. John Papanikolas. Joining his lab was easily one of the best decisions I've ever made and I will always be grateful for his guidance, patience, and his support throughout my graduate studies. He has helped me grow not only as a scientist but as a person and created this supportive environment for his students to build the confidence they need to succeed in life. Additional recognition is required for Dr. James Cahoon for his guidance and the rest of his group for providing silicon and germanium nanowire samples on our projects.

I would also like to thank Dr. Michelle Gabriel for training me on the spatially-separated microscope, and for her help when I first joined the Papanikolas group. Extra thanks go to Emma for her unending patience with training me on all the experiments and equipment in the lab when I first joined the group and mentoring over the years. I'd also like to thank all of the members of the Papanikolas group, especially Dr. Melissa Gish, Leah Bowers, Dr. Lenzi Williams, and Jason Malizia for their help and advice with the various microscopy projects and surprisingly, for actually keeping me sane.

Additionally, I would also like to acknowledge Tyler Motley, Wesley Swords, Kelley Rountree, and Kelsey Brereton for being my friends from the very first week of graduate school. We have made so many great memories together, you guys made graduate school worth sticking out. I would like to thank Elyssa Kayser for being my best friend and always being available any time I need reassuring that I could make it through my Ph.D. Infinite thanks to my family, for their

TABLE OF CONTENTS

LIST OF TABLES

LIST OF FIGURES

LIST OF ABBREVIATIONS AND SYMBOLS

AFM   atomic force microscopy

AOM   acousto-optic modulator

A_{ref} amplitude of the reference frequency for lock-in detection

A_{sig} amplitude of the signal in lock-in detection

BBO   beta barium borate

CB   conduction band

C_L longitudinal speed of sound in a material

C_P specific heat capacity

CVD   chemical vapor deposition

CW   continuous wave

d   diameter (Ch. 3)

d   nanoflake thickness (Ch. 5)

D_c carrier diffusion constant

D_T thermal diffusivity

DRIE   deep reactive ion etch

E   Young's modulus

FFT   fast Fourier transform

FWHM	full-width-at-half-maximum
GS	ground state
I	intensity
J_n	Bessel function
k	thermal conductivity
LA	longitudinal acoustic phonon mode
MSP	microspectrophotometer
NA	numerical aperture
NF	nanoflake
NW	nanowire
PMT	photomultiplier tube
PSD	phase sensitive detection
RF	radio frequency
RBM	radial breathing mode
SEM	scanning electron microscopy
SFG	sum frequency generation
SHG	second harmonic generation
SOPP	spatially-overlapped pump-probe

SSPP	spatially-separated pump-probe
TA	transient absorption
TMDC	transition metal dichalcogenide
VB	valence band
VLS	vapor-liquid-solid
VS	virtual state
Δx	spatial separation of the pump and probe beams
Δt	pump-probe delay time
Γ_C	full-width at half-maximum of carrier diffusion profiles
Γ_T	full-width at half-maximum of thermal diffusion profiles
γ_{pu}	spatial full-width at half-maximums of the pump pulse
γ_{pr}	spatial full-width at half-maximums of the probe pulse
λ	wavelength
ν	Poisson's ratio
ξ_n	eigenvalue for the breathing mode
ρ	density
τ_c	electron-hole recombination lifetime
τ_T	thermal dissipation lifetime

τ_{Avg} exciton relaxation lifetime

ϕ_{ref} phase component of the lock-in reference frequency

ϕ_{sig} phase component of the signal frequency in lock-in detection

ψ_{ref} waveform for the reference frequency for a lock-in detector

ψ_{sig} waveform of the chopped pump pulse train in lock-in detection

ω_{br} angular frequency of breathing mode

ω_{LA} angular frequency of longitudinal acoustic mode

ω_{ref} angular frequency of the lock-in reference frequency

ω_{sig} angular frequency of the signal waveform in lock-in detection

CHAPTER 1: INTRODUCTION

1.1. Motivation

As materials shrink in size from bulk to the nanoscale, their properties deviate from their bulk counterparts and, consequently, reveal unique applications for nanoscale devices. Ultrafast dynamics play an essential role in the performance of many emerging semiconductor nanotechnologies.[1-3] As a consequence of their small size, surface defects dramatically degrade the electronic and optical properties of semiconductors when the size of the materials are reduced to the nanoscale.[4-7] In semiconductor nanowires, the surface contains a higher defect density than the core, decreasing the charge carrier lifetime.[8] In contrast, two-dimensional transition metal dichalcogenide (TMDC) materials, have an X-M-X structure where M is a transition metal (Mo, W, Re, etc.) and X is a chalcogen atom (S, Se, or Te), have a significantly lower density of defects at the basal surface than traditional bulk semiconductors as a result of the layers being held together by Van der Waals interactions.[5, 9-11] The edges of the layers have dangling bonds that often have defects, which enable catalytic activity[12] or limit device performance[13].

1.2. Impact of Heterogeneity

Heterogeneity within samples of nanostructures (such as variation in grain boundaries, morphology, orientation, thickness, defect concentration, and strain) strongly affect the electronic and optical properties of a material and can drastically alter the measured

experimental response.[4, 8, 14] That is, every structure is different, so even a first-order kinetic response is observed as a multiexponential decay in an ensemble measurement (*e.g.*, pump-probe spectroscopy).[15, 16]

Acoustic phonons result from the non-radiative recombination of excited charge carriers.[17-25] When the recombination time is shorter than the period of vibration, a short laser pulse impulsively excites the structure, producing a wave packet that evolves in time and space that results in vibrational oscillations (*e.g.*, coherence).[26] The coherent phonon frequency is used to determine the elastic properties of nanostructures, which are highly dependent on geometry.[16, 17, 22, 26-47] Variations in diameter (often found in ensemble samples)[14, 48] results in the coherence dying out over time because each NW generates a slightly different phonon frequency that interferes; obscuring of the true acoustic phonon frequency.[15, 16, 49]

Time-resolved spectroscopic techniques are commonly used to characterize electronic, mechanical, and optoelectronic properties in semiconductor nanomaterials, such as electron and vibration dynamics on ultrafast (sub-picosecond) timescales.[14, 48, 50-52] These methods typically average over ensembles that contain structures with a variety of sizes, shapes, compositions, and conformations.[3, 5] These techniques reveal multiexponential decay components, which are attributed to different pathways for excited state decay. The limited spatial resolution impedes the ability to correlate device performance with specific structural features. Disentangling dynamics arising from inhomogeneous samples presents a barrier for the designing of new nanoscale devices.

1.3. Advantage of Microscopy

High spatial resolution pump-probe microscopy is needed to interrogate the physics of localized regions on single nanostructures to disentangle the intrinsic kinetic pathways from those arising from various structural features. Excitation of nanostructures that are smaller than the laser spot size uniformly excites the entire structure, generating excited state dynamics that are an average of the entire structure.[18,19] When the pump and probe spot sizes are smaller than the nanostructure, the pump pulse creates a localized excitation where the photogenerated carriers and phonons can travel out of the initial excitation spot through the nanostructure. This allows for the investigation of transport dynamics (*i.e.* electron diffusion, thermal conductivity, phonon propagation) through a single structure.[26,27]

1.4. Chapter Overview

While this chapter (**Chapter 1**) provides the rationale behind this work and an introduction to temporally and spatially-resolved microscopy, the next chapters take a more in-depth look at diffraction-limited pump-probe microscopy with specific emphasis on transient absorption microscopy. **Chapter 2** is devoted to the details of our home-built ultrafast pump-probe microscopy technique and the microscope itself since its application comprises a major component of this dissertation work. **Chapter 3** details the results of extracting carrier and thermal diffusion from the vibrational motion in germanium nanowires using the spatially-separated pump-probe microscopy technique. Spatially-separated transients reveal acoustic phonon propagation in suspended Ge NW. In **Chapter 4,** the microscope is used to study a more complex semiconductor nanostructure; two-dimensional transition metal dichalcogenide materials. In these experiments, spatial heterogeneity in the

exciton and free carriers dynamics are observed, along with the formation of exciton-polaritons. **Chapter 5** demonstrates the versatility of the spatially-separated pump-probe microscope by detailing its application to the study of the propagation of coherent acoustic phonon modes in tungsten disulfide and tungsten diselenide nanoflakes. The last chapter of this dissertation, **Chapter 6**, includes a brief summary of this work and future directions.

REFERENCES

1.   Kennedy, T.; Mullane, E.; Geaney, H.; Osiak, M.; O'Dwyer, C.; Ryan, K. M., High-Performance Germanium Nanowire-Based Lithium-Ion Battery Anodes Extending over 1000 Cycles through in Situ Formation of a Continuous Porous Network. *Nano Lett.* **2014,** *14* (2), 716-23.

2.   Kennedy, T.; Brandon, M.; Ryan, K. M., Advances in the Application of Silicon and Germanium Nanowires for High-Performance Lithium-Ion Batteries. *Adv. Mater.* **2016,** *28* (27), 5696-704.

3.   Grumstrup, E. M.; Gabriel, M. M.; Cating, E. E. M.; Van Goethem, E. M.; Papanikolas, J. M., Pump–Probe Microscopy: Visualization and Spectroscopy of Ultrafast Dynamics at the Nanoscale. *Chem. Phys.* **2015,** *458*, 30-40.

4.   Mahajan, S., Defects in Semiconductors and Their Effects on Devices. *Acta Mater.* **2000,** *48* (1), 137-149.

5.   Cao, L., Two-Dimensional Transition-Metal Dichalcogenide Materials: Toward an Age of Atomic-Scale Photonics. *MRS Bull.* **2015,** *40* (07), 592-599.

6.   Cao, Z.; Harb, M.; Lardhi, S.; Cavallo, L., Impact of Interfacial Defects on the Properties of Monolayer Transition Metal Dichalcogenide Lateral Heterojunctions. *J Phys Chem Lett* **2017,** *8* (7), 1664-1669.

7.   Cui, Z.; Ke, X.; Li, E.; Wang, X.; Ding, Y.; Liu, T.; Li, M.; Zhao, B., Effect of Vacancy Defect on Optoelectronic Properties of Monolayer Tungsten Diselenide. *Optical and Quantum Electronics* **2017,** *50* (1).

8.   Cating, E. E. M.; Pinion, C. W.; Christesen, J. D.; Christie, C. A.; Grumstrup, E. M.; Cahoon, J. F.; Papanikolas, J. M., Probing Intrawire, Interwire, and Diameter-Dependent Variations in Silicon Nanowire Surface Trap Density with Pump-Probe Microscopy. *Nano Lett.* **2017,** *17* (10), 5956-5961.

9.   Duong, D. L.; Yun, S. J.; Lee, Y. H., Van Der Waals Layered Materials: Opportunities and Challenges. *ACS Nano* **2017,** *11* (12), 11803-11830.

10.   Xiao, J.; Zhao, M.; Wang, Y.; Zhang, X., Excitons in Atomically Thin 2D Semiconductors and Their Applications. *Nanophotonics* **2017,** *6* (6).

11.   Shi, H.; Yan, R.; Bertolazzi, S.; Brivio, J.; Gao, B.; Kis, A.; Jena, D.; Xing, H. G.; Huang, L., Exciton Dynamics in Suspended Monolayer and Few-Layer MoS_2 2D Crystals. *ACS Nano* **2013,** *7* (2), 1072-1080.

12.   Zhang, Y.; Yan, J.; Ren, X.; Pang, L.; Chen, H.; Liu, S., 2d Ws 2 Nanosheet Supported Pt Nanoparticles for Enhanced Hydrogen Evolution Reaction. *Int. J. Hydrogen Energy* **2017,** *42* (8), 5472-5477.

13.   Vogel, E. M.; Robinson, J. A., Two-Dimensional Layered Transition-Metal Dichalcogenides for Versatile Properties and Applications. *MRS Bull.* **2015,** *40* (07), 558-563.

14.   Grumstrup, E. M.; Cating, E. M.; Gabriel, M. M.; Pinion, C. W.; Christesen, J. D.; Kirschbrown, J. R.; Vallorz, E. L.; Cahoon, J. F.; Papanikolas, J. M., Ultrafast Carrier Dynamics of Silicon Nanowire Ensembles: The Impact of Geometrical Heterogeneity on Charge Carrier Lifetime. *J. Phys. Chem. C* **2014,** *118* (16), 8626-8633.

15.   Li, Y.; Clady, R.; Marshall, A. F.; Park, J.; Thombare, S. V.; Chan, G.; Schmidt, T. W.; Brongersma, M. L.; McIntyre, P. C., Ultrafast Carrier Dynamics of a Photo-Excited Germanium Nanowire–Air Metamaterial. *ACS Photonics* **2015,** *2* (8), 1091-1098.

16.   Li, Y.; Clady, R.; Park, J.; Thombare, S. V.; Schmidt, T. W.; Brongersma, M. L.; McIntyre, P. C., Ultrafast Electron and Phonon Response of Oriented and Diameter-Controlled Germanium Nanowire Arrays. *Nano Lett.* **2014,** *14* (6), 3427-31.

17.   Major, T. A.; Lo, S. S.; Yu, K.; Hartland, G. V., Time-Resolved Studies of the Acoustic Vibrational Modes of Metal and Semiconductor Nano-Objects. *J. Phys. Chem. Lett.* **2014,** *5* (5), 866-74.

18.   Pollock, K. L.; Doan, H. Q.; Rustagi, A.; Stanton, C. J.; Cuk, T., Detecting the Photoexcited Carrier Distribution across GaAs/Transition Metal Oxide Interfaces by Coherent Longitudinal Acoustic Phonons. *J Phys Chem Lett* **2017,** *8* (5), 922-928.

19. Zollner, S.; Myers, K. D.; Jensen, K. G.; Dolan, J. M.; Bailey, D. W.; Stanton, C. J., Femtosecond Interband Hole Scattering in Ge Studied by Pump-Probe Reflectivity. *Solid State Commun.* **1997,** *104* (1), 51-55.

20. Giri, P. K.; Kesavamoorthy, R.; Panigrahi, B. K.; Nair, K. G. M., Surface Acoustic Phonon Modes of Ge Nanocrystals Embedded in SiO_2. *Solid State Commun.* **2005,** *136* (1), 36-40.

21. Dong, S.; Lian, J.; Jhon, M. H.; Chan, Y.; Loh, Z. H., Pump-Power Dependence of Coherent Acoustic Phonon Frequencies in Colloidal CdSe/CdS Core/Shell Nanoplatelets. *Nano Lett.* **2017,** *17* (5), 3312-3319.

22. Hu, M.; Wang, X.; Hartland, G. V.; Mulvaney, P.; Juste, J. P.; Sader, J. E., Vibrational Response of Nanorods to Ultrafast Laser Induced Heating: Theoretical and Experimental Analysis. *J. Am. Chem. Soc.* **2003,** *125* (48), 14925-33.

23. Wang, Y.; Guo, L.; Xu, X.; Pierce, J.; Venkatasubramanian, R., Origin of Coherent Phonons in Bi_2Te_3 Excited by Ultrafast Laser Pulses. *Phys. Rev. B* **2013,** *88* (6).

24. Cavalleri, A.; Schoenlein, R. W., Femtosecond X-Rays and Structural Dynamics in Condensed Matter. In *Ultrafast Dynamical Processes in Semiconductors*, Tsen, K.-T., Ed. Springer Berlin Heidelberg: Berlin, Heidelberg, 2004; pp 309-338.

25. Zeiger, H. J.; Vidal, J.; Cheng, T. K.; Ippen, E. P.; Dresselhaus, G.; Dresselhaus, M. S., Theory for Displacive Excitation of Coherent Phonons. *Phys. Rev. B* **1992,** *45* (2), 768-778.

26. Hodak, J. H.; Henglein, A.; Hartland, G. V., Photophysics of Nanometer Sized Metal Particles: Electron−Phonon Coupling and Coherent Excitation of Breathing Vibrational Modes. *J. Phys. Chem. B* **2000,** *104* (43), 9954-9965.

27. Petrova, H.; Perez Juste, J.; Pastoriza-Santos, I.; Hartland, G. V.; Liz-Marzan, L. M.; Mulvaney, P., On the Temperature Stability of Gold Nanorods: Comparison between Thermal and Ultrafast Laser-Induced Heating. *PCCP* **2006,** *8* (7), 814-21.

28. Staleva, H.; Hartland, G. V., Vibrational Dynamics of Silver Nanocubes and Nanowires Studied by Single-Particle Transient Absorption Spectroscopy. *Adv. Funct. Mater.* **2008,** *18* (23), 3809-3817.

29. Staleva, H.; Skrabalak, S. E.; Carey, C. R.; Kosel, T.; Xia, Y.; Hartland, G. V., Coupling to Light, and Transport and Dissipation of Energy in Silver Nanowires. *PCCP* **2009,** *11* (28), 5889-5896.

30. Zijlstra, P.; Tchebotareva, A. L.; Chon, J. W. M.; Gu, M.; Orrit, M., Acoustic Oscillations and Elastic Moduli of Single Gold Nanorods. *Nano Lett.* **2008,** *8* (10), 3493-3497.

31. Su, M. N.; Dongare, P. D.; Chakraborty, D.; Zhang, Y.; Yi, C.; Wen, F.; Chang, W. S.; Nordlander, P.; Sader, J. E.; Halas, N. J.; Link, S., Optomechanics of Single Aluminum Nanodisks. *Nano Lett.* **2017,** *17* (4), 2575-2583.

32. Xu, F.; Guillet, Y.; Ravaine, S.; Audoin, B., All-Optical in-Depth Detection of the Acoustic Wave Emitted by a Single Gold Nanorod. *Phys. Rev. B* **2018,** *97* (16).

33. Hartland, G. V., Optical Studies of Dynamics in Noble Metal Nanostructures. *Chem. Rev.* **2011,** *111* (6), 3858-87.

34. Owrutsky, J. C.; Pomfret, M. B.; Brown, D. J., Coherent Acoustic Oscillations of Nanorods Composed of Various Metals. *J. Phys. Chem. C* **2009,** *113* (25), 10947-10955.

35. Juve, V.; Crut, A.; Maioli, P.; Pellarin, M.; Broyer, M.; Del Fatti, N.; Vallee, F., Probing Elasticity at the Nanoscale: Terahertz Acoustic Vibration of Small Metal Nanoparticles. *Nano Lett.* **2010,** *10* (5), 1853-8.

36. Polli, D.; Lisiecki, I.; Portalès, H.; Cerullo, G.; Pileni, M.-P., Low Sensitivity of Acoustic Breathing Mode Frequency in Co Nanocrystals Upon Change in Nanocrystallinity. *ACS Nano* **2011,** *5* (7), 5785-5791.

37. Wall, S.; Wegkamp, D.; Foglia, L.; Appavoo, K.; Nag, J.; Haglund, R. F., Jr.; Stahler, J.; Wolf, M., Ultrafast Changes in Lattice Symmetry Probed by Coherent Phonons. *Nat. Commun.* **2012,** *3*, 721.

38. Pashkin, A.; Kübler, C.; Ehrke, H.; Lopez, R.; Halabica, A.; Haglund, R. F.; Huber, R.; Leitenstorfer, A., Ultrafast Insulator-Metal Phase Transition in VO_2 Studied by Multiterahertz Spectroscopy. *Phys. Rev. B* **2011,** *83* (19).

39. Lo, S. S.; Major, T. A.; Petchsang, N.; Huang, L.; Kuno, M. K.; Hartland, G. V., Charge Carrier Trapping and Acoustic Phonon Modes in Single CdTe Nanowires. *ACS Nano* **2012,** *6* (6), 5274-5282.

40. Sakuma, H.; Tomoda, M.; Otsuka, P. H.; Matsuda, O.; Wright, O. B.; Fukui, T.; Tomioka, K.; Veres, I. A., Vibrational Modes of GaAs Hexagonal Nanopillar Arrays Studied with Ultrashort Optical Pulses. *Appl. Phys. Lett.* **2012,** *100* (13), 131902.

41. Pfeifer, T.; Kutt, W.; Kurz, H.; Scholz, R., Generation and Detection of Coherent Optical Phonons in Germanium. *Phys. Rev. Lett.* **1992,** *69* (22), 3248-3251.

42. Yu, K.; Major, T. A.; Chakraborty, D.; Devadas, M. S.; Sader, J. E.; Hartland, G. V., Compressible Viscoelastic Liquid Effects Generated by the Breathing Modes of Isolated Metal Nanowires. *Nano Lett.* **2015,** *15* (6), 3964-70.

43. Jean, C.; Belliard, L.; Cornelius, T. W.; Thomas, O.; Toimil-Molares, M. E.; Cassinelli, M.; Becerra, L.; Perrin, B., Direct Observation of Gigahertz Coherent Guided Acoustic Phonons in Free-Standing Single Copper Nanowires. *J. Phys. Chem. Lett.* **2014,** *5* (23), 4100-4.

44. Jean, C.; Belliard, L.; Cornelius, T. W.; Thomas, O.; Pennec, Y.; Cassinelli, M.; Toimil-Molares, M. E.; Perrin, B., Spatiotemporal Imaging of the Acoustic Field Emitted by a Single Copper Nanowire. *Nano Lett.* **2016,** *16* (10), 6592-6598.

45. Hu, M.; Hillyard, P.; Hartland, G. V.; Kosel, T.; Perez-Juste, J.; Mulvaney, P., Determination of the Elastic Constants of Gold Nanorods Produced by Seed Mediated Growth. *Nano Lett.* **2004,** *4* (12), 2493-2497.

46. Shiri, D.; Verma, A.; Khader, M. M., Photoconductive Response of Strained Silicon Nanowires: A Monte Carlo Study. *J. Appl. Phys.* **2014,** *115* (13), 133708.

47.   Yu, K.; Zijlstra, P.; Sader, J. E.; Xu, Q. H.; Orrit, M., Damping of Acoustic Vibrations of Immobilized Single Gold Nanorods in Different Environments. *Nano Lett.* **2013,** *13* (6), 2710-6.

48.   Grumstrup, E. M.; Gabriel, M. M.; Cating, E. M.; Pinion, C. W.; Christesen, J. D.; Kirschbrown, J. R.; Vallorz, E. L.; Cahoon, J. F.; Papanikolas, J. M., Ultrafast Carrier Dynamics in Individual Silicon Nanowires: Characterization of Diameter-Dependent Carrier Lifetime and Surface Recombination with Pump–Probe Microscopy. *J. Phys. Chem. C* **2014,** *118* (16), 8634-8640.

49.   Gan, Y.; Wang, C.; Chen, Z., Ultrafast Laser-Excited Vibration and Elastic Modulus of Individual Gold Nanorods. *Opt. Lett.* **2015,** *40* (3), 340-3.

50.   Ruppert, C.; Chernikov, A.; Hill, H. M.; Rigosi, A. F.; Heinz, T. F., The Role of Electronic and Phononic Excitation in the Optical Response of Monolayer WS_2 after Ultrafast Excitation. *Nano Lett.* **2017,** *17* (2), 644-651.

51.   Breusing, M.; Kuehn, S.; Winzer, T.; Malić, E.; Milde, F.; Severin, N.; Rabe, J. P.; Ropers, C.; Knorr, A.; Elsaesser, T., Ultrafast Nonequilibrium Carrier Dynamics in a Single Graphene Layer. *Phys. Rev. B* **2011,** *83* (15), 153410.

52.   Hong, X.; Kim, J.; Shi, S.-F.; Zhang, Y.; Jin, C.; Sun, Y.; Tongay, S.; Wu, J.; Zhang, Y.; Wang, F., Ultrafast Charge Transfer in Atomically Thin MoS_2/WS_2 Heterostructures. *Nat. Nanotechnol.* **2014,** *9*, 682.

CHAPTER 2: INSTRUMENTATION

2.1. Microscope Description

The work in this dissertation utilizes a femtosecond pump-probe microscopy setup, shown in Figure 2.1 and described previously.[1-9] Using this setup, we can monitor carrier migration and relaxation within individual nanostructures to correlate structure-function relationships to photophysical phenomena. This microscope can operate in two configurations; spatially-overlapped pump-probe (SOPP) mode or spatially-separated pump-probe (SSPP) mode. In the SOPP mode, samples are excited and probe in the same location, collecting temporally resolved excited state dynamics of nanomaterials. With the SSPP mode, samples can be excited in one location and probed in another, enabling the visualization of transport properties in nanomaterials.

Figure 2.1 shows a schematic of our instrument. A solid-state diode-pumped continuous wave (CW) laser (Spectra-Physics: Millennia Pro-15sJ) is used as the primary radiation source. The Millennia uses a diode laser output to pump a neodymium yttrium vanadate crystalline matrix (Nd: YVO_4) resulting in a near-infrared emission at a wavelength of $\lambda = 1064$ nm. The output is then frequency doubled by second-harmonic generation (SHG) in a lithium triborate (LBO; LiB_3O_5) crystal, to output up to 15 W of CW radiation at a wavelength of 532 nm. The 532 nm CW output of the Millennia pumps a sapphire crystalline matrix (Ti: Al_2O_3) in a Ti:sapphire laser (Spectra-Physics: Tsunami). The gain medium of the laser is a sapphire crystalline matrix (Ti: Al_2O_3) where titanium ions (Ti^{3+}) are substituted for a small percentage of

the aluminum (Al^{3+}) ions. Absorption in the gain medium occurs over a broad range of wavelengths from 400 – 600 nm. The resulting stimulated emission generates a laser output tunable over 700 – 1000 nm. The mode-locked pulses are <100 fs with a repetition rate of 80 MHz.
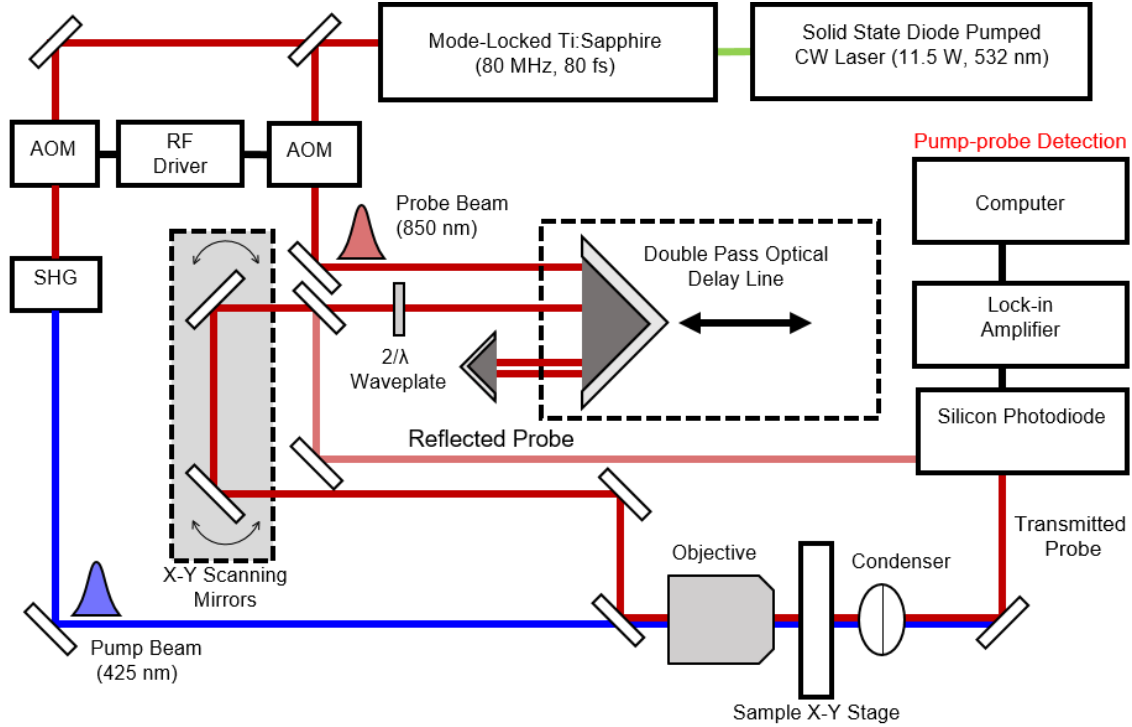
Figure 2.1: Schematic diagram of our pump-probe microscope. The pump and probe pulses are obtained from the output of a Ti:sapphire laser operating at 80 MHz. The beam is split into the two pump and probe pulses. The pump portion is frequency doubled by SHG in a BBO crystal. Both beams are directed through synchronized AOMs to reduce the repetition rate of the pulses. The probe is sent through a mechanical delay stage twice (double pass optical delay line) to vary its arrival time at the sample with respect to that of the pump. The probe beam is also directed through a set of two scanning mirrors to vary the angle of incidence on the back aperture of the objective, enabling its focal position to be adjusted laterally with respect to that of the pump. The pump and probe beams are recombined using a beam splitter and focused to diffraction-limited spots at the sample. Spatially-overlapped imaging is achieved by raster scanning the sample stage across the objective focal point, while spatially-separated imaging is achieved by raster scanning the position of the probe with respect to the pump while holding the delay stage fixed. The change in transmitted (or reflected) probe intensity is monitored with a balanced photodetector and lock-in amplifier.

12

For the experiments discussed in this work, the output of the Ti:sapphire laser is tuned to 850 nm. The Ti:sapphire laser output is split into two beams; one is used as the probe and the remainder is frequency doubled using second harmonic generation (SHG) in a β-barium borate (BBO) crystal to produce the 425 nm pump beam. The pump and probe beams each pass through a dedicated acousto-optic modulator (AOM) to reduce the repetition rate of the laser to 1-4 MHz. This step ensures that the sample relaxes to its equilibrium state before the next pump-probe pulse pair arrives. Two radio frequency (RF) drivers (Gooch & Housego: 64381.9-SYN-9.5-1 for the probe AOM and Gooch & Housego: R31389.5-5AS for the pump AOM) are used to control the AOMs (Gooch & Housego: 17389.93-FOA) The drivers are synchronized to the output of the electronics module from the Ti:Sapphire laser (Spectra-Physics: 3995) and a delay generator (SRS-645DG).

The probe is passed through a mechanical delay stage twice using a retroreflector to vary its arrival time at the sample with respect to the pump. Sending the probe through the delay stage twice allows dynamics to be measured from 0-3 ns after the arrival of the pump pulse at the sample. The sample is positioned using a moveable x-y stage (Queensgate Instruments: NPS-XY-100A). Computer controlled mirrors vary the angle of incidence of the probe beam as it enters the back of the objective, allowing the probe beam to be focused to a point on the sample that is laterally offset relative to the pump. Before focusing, the pump and probe beams are recombined with a dichroic beam-splitter and directed onto the back aperture of a 100x microscope objective with a numerical aperture (NA) of 0.8. Focusing is achieved by adjusting the height of the objective using a nanopiezo-actuated stage, enabling remote controlled focusing of the two laser pulses to diffraction-limited spot sizes. In the case of a 425 nm pump pulse and an 850 nm probe pulse, additional steps are taken to ensure that both colors reach a focal point in

the same plane. This is achieved by slightly decollimating the pump light before the objective. Spatial overlap of the pump and probe pulses is achieved by transmission imaging a structure with the pump and probe. The probe transmission image is shifted laterally to overlay on the pump transmission image by adjusting the angle of incidence on the back of the objective.

In transmission mode, a condenser lens with a higher numerical aperture than the objective collects the transmitted light after passing through the sample. With reflective mode, the light is focused by the microscope objective onto the sample and the light reflected off the sample surface is recollected back through the objective and directed onto a second photodetector. In both transmission and reflective mode, the pump light is removed by spectral filters and the intensity of the probe beam (I) is measured using a balanced photodetector. Pump-induced changes in the probe beam (ΔI) are extracted through the use of a lock-in detector (SRS: SR830), where the pump AOM is inhibited at a 50% duty cycle to modulate the pump beam at 16 kHz. This frequency also serves as the reference for the lock-in detector, which will be discussed in more detail below. This transient absorption microscopy technique is capable of detecting $\Delta I/I \sim 5 \times 10^{-5}$.

2.1.1. Pump Wavelength Generation

To generate the high energy pump pulses (425 nm), the output from the pump pulse picker (850 nm) is frequency doubled through SHG in a BBO crystal. In SHG, two photons of the same frequency are "added" together in a nonlinear crystal ($\hbar\omega_2 = \hbar\omega_1 + \hbar\omega_1$, Figure 2.2A) to generate a new photon with twice the energy as the initial photons. The energy level scheme shown in Figure 2.2B describes how the two low energy photons cause an instantaneous transition from the ground state (GS) of the BBO to a virtual state (VS) that can give off the new

photon with that energy difference. This nonlinear process is highly sensitive to phase-matching

of the two low energy photons ($2\omega_1$) to be efficient. The crystal can be rotated relative to the

fundamental beam to adjust the phase matching of the fundamental photons and maximize the

power of the second harmonic beam.
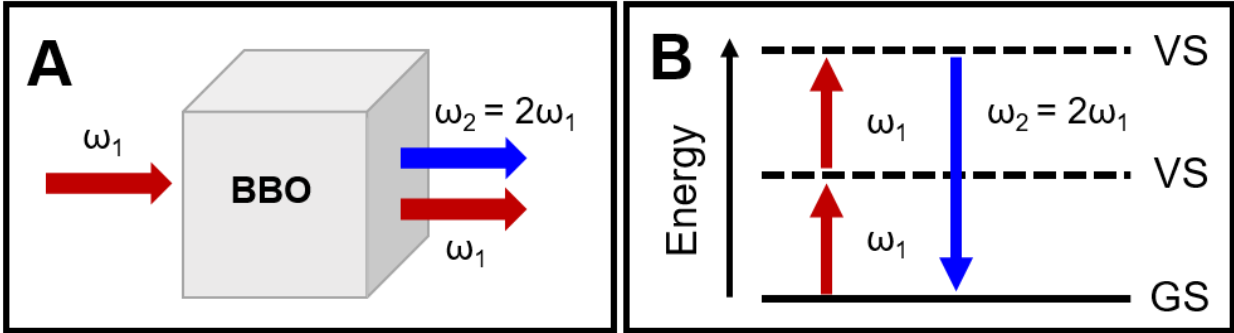
Figure 2.2: Illustration of second harmonic generation in BBO. **(A)** The 850 nm (ω_1) beam is focused into the BBO crystal to generate the pump beam with a wavelength of 425 nm (ω_2). **(B)** Energy level diagram describing SHG. Two photons with the same frequency (ω_1) interact to output a new photon with twice the energy (ω_2) as the incoming photons.

2.1.2. Performance Characteristics

Emission detection was used to measure the performance characteristics of the

microscope (temporal resolution and spatial resolution).[5] The microscope is capable of emission

detection or in a backward-scatter mode (not shown in Figure 2.1) where fluorescence from

emissive samples is recollected by the microscope objective, focused on the slit of a

monochromator, and detected by a photomultiplier tube (PMT).
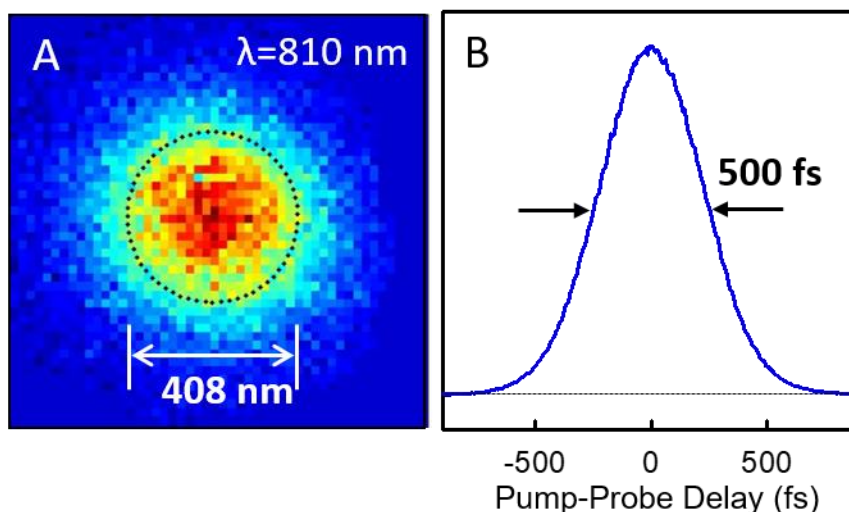
Figure 2.3: Microscope resolution. **(A)** Two-photon emission image of a 100 nm nanoparticle with 810 nm excitation. The emission feature size suggests that the lateral resolution is approximately 410 nm. **(B)** Cross-correlation of the pump and probe pulses in the microscope obtained by monitoring the sum-frequency signal generated by a ZnO crystal. Adapted from ref #5.

Two-photon fluorescence of a quantum dot (Figure 2.3A) is used to determine the diffraction-limited spatial resolution of the microscope because the quantum dot acts as point source emitter. Emission from quantum dots was collected while the sample stage is raster scanned across the focal point of the excitation pulses (810 nm). The emission profile of a single dot is a 2D Gaussian with a full-width-at-half-maxiumum (FWHM) of ~400 nm showing the microscope spatial resolution.[5]

Taking a cross-correlation of the pump and probe beams, shown in Figure 2.3B, estimates the time resolution of the microscope.[5] The pump and probe beams are focused onto a single point within a zinc oxide (ZnO) crystal generating sum frequency generation (SFG). SFG is an

instantaneous nonlinear process that occurs only when the pump and probe beams are focused and overlapped spatially and temporally within a nonlinear crystal. The monochromator is tuned to the sum frequency and is detected using the PMT while the delay stage is scanned. The signal takes the shape of a Gaussian peak from the crossing of the two pulses temporally where the time resolution is taken as the FWHM of the Gaussian. The resulting time resolution of our microscope is ~500 fs.

2.1.3. Transient Absorption

The basic operating principle of the pump-probe technique is illustrated in Figure 2.4. Pump-probe techniques can operate in transient reflectivity or transient absorption mode, the experiments presented in this work were carried out in transient absorption or transient reflectivity configuration illustrated in Figures 2.4 and 2.5, respectively. An initial pump pulse excites the sample, giving rise to a change in its absorption and/or reflectivity properties. The probe pulse measures a dynamic response in a sample due to an excitation pump pulse. The dynamic response is measured over different pump-probe delays by scanning the mechanical delay stage. In transient absorption pump-probe technique, the change in the samples absorption and/or reflection properties gives rise to a change in transmission of the probe pulse. Figure 2.4A, the probe pulse arrives at the sample before the pump, and therefore, no change in probe intensity is observed. A spike in signal appears just after (or quasi-simultaneously with) the pump and probe pulses due to sample excitation (Figure 2.4B). As pump-probe delay grows longer, the sample relaxes back to its equilibrium state. The changes are monitored by a decrease in probe intensity over time (Figure 2.4C).
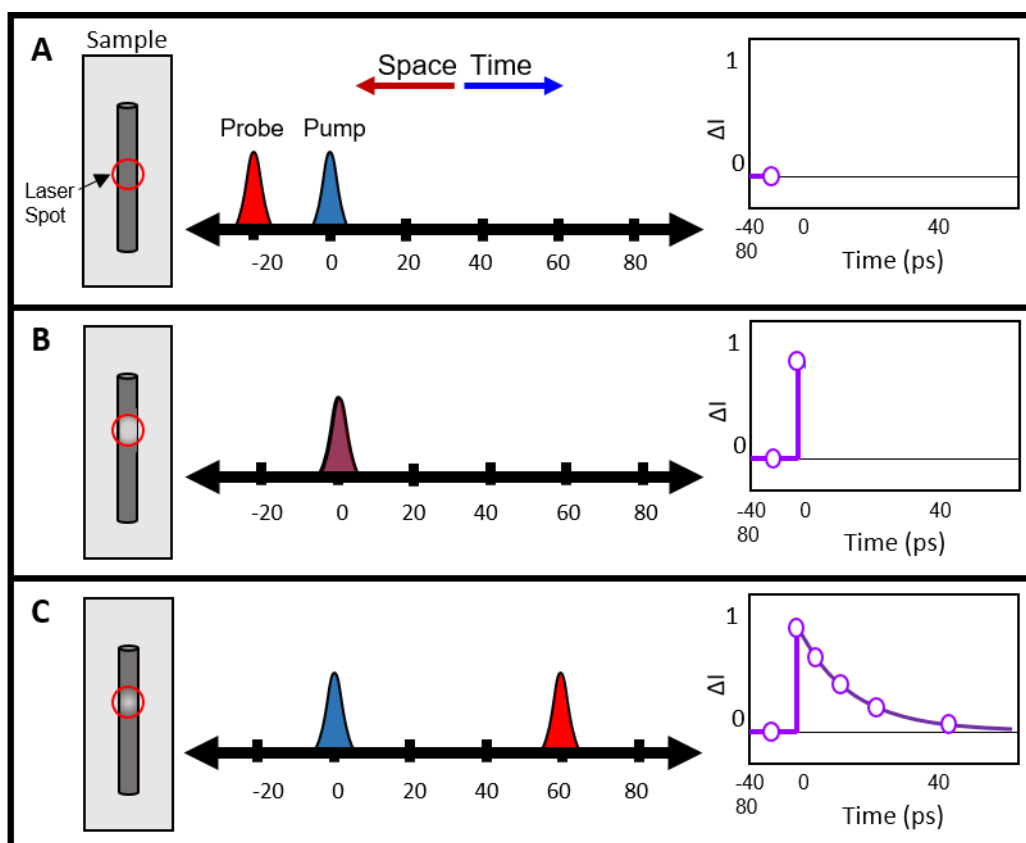
Figure 2.4: Diagram of transient absorption. (**A**) The transient absorption experiment is comprised of two pulses, a pump (blue) a probe (red), which the probe's arrival is scanned in time relative to the pump pulse. In this diagram, time progresses to the right (blue arrow) and the spatial coordinate is to the left (red arrow) such that in the top configuration the probe pulse hits the sample before the pump pulse. In this configuration, the sample exhibits no pump-induced change in optical properties and the measured change in probe transmission is zero (plot on far right). (**B**) After the pump pulse excites the sample, a change in transmission properties of the probe occurs. In this case, the sample transmits more probe light after excitation and a maximum in signal is seen just after the pump pulse arrives at the sample. (**C**) As the probe pulse is delayed further in time, the sample begins to relax back to its equilibrium position and a decrease in pump-induced transmission is observed. After the sample has had sufficient time to completely relaxed, the observed signal response is back at baseline.

2.1.4. Transient Reflectivity

In the transient reflectivity pump-probe technique, the change in the sample's reflectivity gives rise to a change in reflection of the probe pulse. Figure 2.5A, the probe pulse arrives before the pump, and therefore, no change in probe intensity is observed. A negative going spike in signal appears just after (or with) the pump pulse due to sample excitation (Figure 2.5B). As the pump-probe delay increases, the sample relaxes back to its equilibrium state. The changes are monitored by a decrease in probe intensity over time (Figure 2.5C).
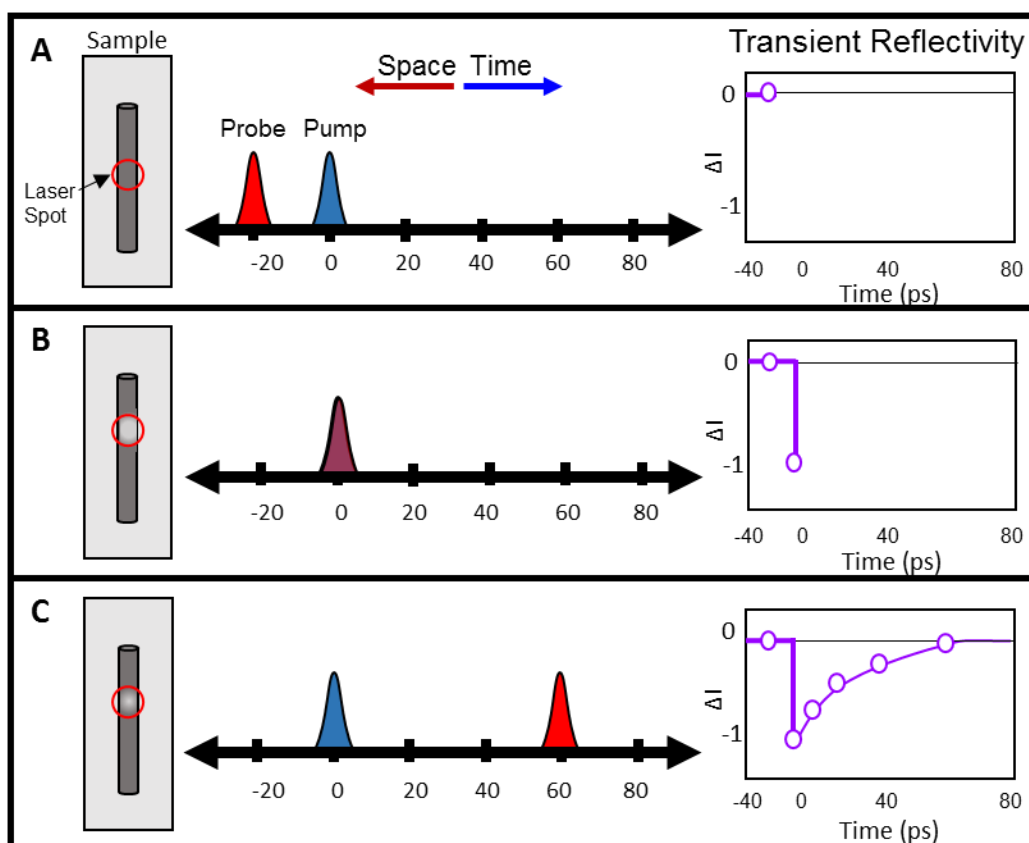
Figure 2.5: Diagram of transient reflectivity. (A) The transient reflectivity experiment is comprised of two pulses, a pump (blue) a probe (red) which is scanned in time relative to the pump pulse. In this diagram, time progresses to the right (blue arrow) and the spatial coordinate is to the left (red arrow) such that in the top configuration the probe pulse hits the sample before the pump pulse. In this configuration, the sample exhibits no pump-induced change in optical properties and the measured change in probe reflection is zero (plot on far right). **(B)** After the pump pulse excites the sample, a change in transmission properties of the probe occurs. In this case, the sample reflects less probe light after excitation and a maximum in signal is seen just after the pump pulse arrives at the sample. **(C)** As the probe pulse is delayed further in time, the sample begins to relax back to its equilibrium position and a decrease in pump-induced reflectivity is observed. After the sample has had sufficient time to completely relaxed, the observed signal response is back at baseline.

2.1.5. Lock-in Detection

Lock-in detection is used to monitor small pump-induced changes in probe transmission (or reflection). The lock-in amplifier extracts a small signal from a noisy environment using

phase sensitive detection (PSD). PSD uses a designated reference frequency and phase to select a single component of the signal and rejects noise signals at all other frequencies. To do this, the lock-in requires a reference signal (ψ_{ref}) that is a square wave output from a function generator. The lock-in converts the square wave to a sine wave with the waveform:

$$\psi_{ref} = A_{ref} \cos(\omega_{ref} t + \phi_{ref}) \qquad [2.1]$$

where A_{ref}, ω_{ref}, and ϕ_{ref} are the amplitude, frequency and phase components of the reference signal. The pump pulse train is also modulated at the same frequency and phase as the lock-in reference using a delay generator with the waveform:

$$\psi_{sig} = A_{sig} \cos(\omega_{sig} t + \phi_{sig}) \qquad [2.2]$$

where A_{sig}, ω_{sig}, and ϕ_{sig} are the amplitude, frequency, and phase components of the signal. Since the lock-in amplifier multiplies the reference frequency by the signal, the resulting in (taking into account a product-sum identity):

$$\psi_{ref}\psi_{sig} = \frac{A_{sig}A_{ref}}{2} \left[\cos\left((\omega_{ref} + \omega_{sig})t + (\phi_{ref} + \phi_{sig})\right)\right]$$

$$+ \frac{A_{sig}A_{ref}}{2} \left[\cos\left((\omega_{ref} - \omega_{sig})t + (\phi_{ref} - \phi_{sig})\right)\right] \qquad [2.3]$$

Multiplying the two waveforms includes components at the sum and difference frequencies. Syncing the pump signal to the same phase and frequency as the reference simplifies the second half of Eq. 2.3 to a DC component. The output of the lock-in produces a DC component, using a low pass filter, where the magnitude is equal to $A_{ref}A_{sig}/2$.
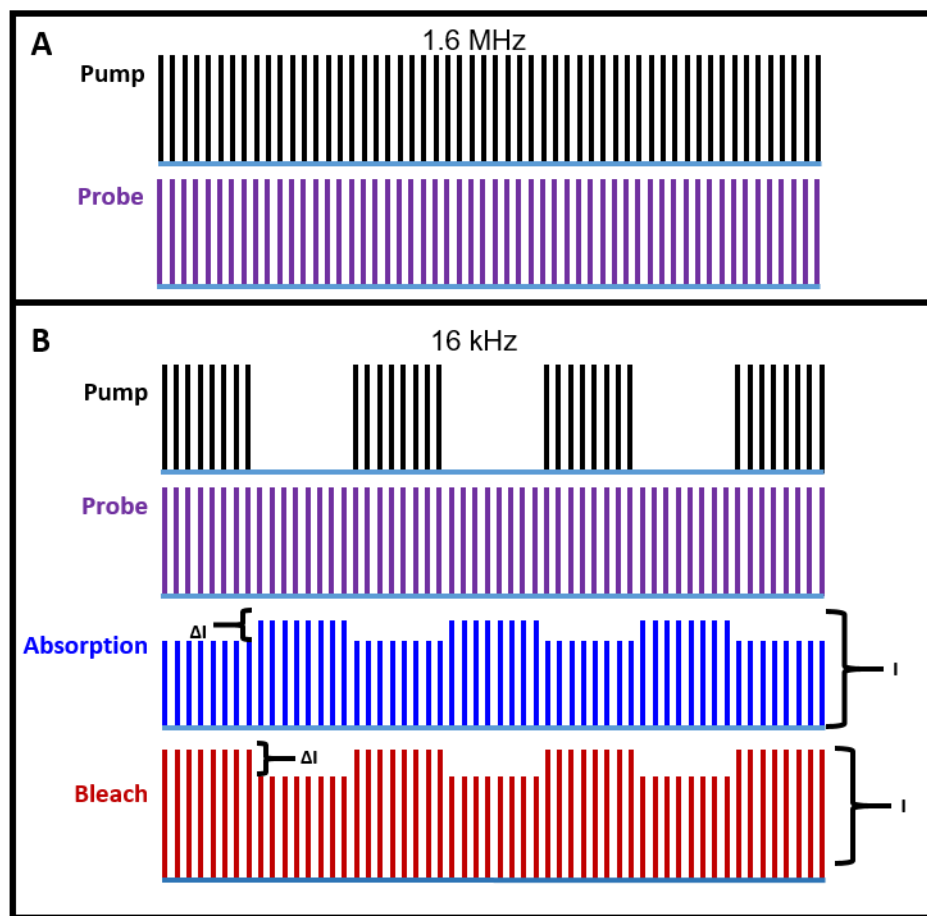
Figure 2.6: Lock-in detection. (A) The pump (black) and probe (purple) pulses are split from the output of the Ti: Sapphire laser and reduced to a repetition rate of 1.6 MHz by a pair of synchronized AOMs. **(B)** The pump AOM is also modulated at a 50% duty cycle to a modulation frequency of 20 KHz which serves as the reference for the AOM. The probe is left unmodulated. While the balance detector measures the entire pulse train (I), the lock-in only outputs signal that is modulated at 16 KHz and therefore only outputs ΔI. If less probe light reaches the detector when the pump pulses are 'on', a decrease, or absorption, of the signal is detected (blue). If more probe light reaches the detector when the pump is 'on', a bleach in signal is observed.

Figure 2.6 provides an illustration of how this works in our experiment. The pump (black) and probe (purple) pulses are split from the output of the Ti:sapphire laser operating at 80 MHz and reduced to a repetition rate of 1.6 MHz by a pair of synchronized AOMs. Only the pump AOM is modulated at a 50% duty cycle to a modulation frequency of 16 kHz, which serves as the reference for the AOM. The probe is left unmodulated. While the balance detector measures the intensity of the entire pulse train (I), the lock-in only outputs signal that is modulated at 16 KHz and therefore only outputs ΔI. If less probe light reaches the detector when the pump pulses are 'on', a decrease, or absorption, of the signal is detected (blue). If more probe light reaches the detector when the pump is 'on', a bleach in signal is observed.

In order to investigate dynamical phenomena occurring at spatially distinct locations from the initial excitation position, previous Papanikolas group members developed a pump-probe microscopy technique that uses a detection scheme that pumps a nanostructure in one position and probing it in another. The following section describes the logistics of the spatially-separated pump-probe configuration.

2.2. Spatially-Separated Alignment and Calibration

The primary foundation behind the SSPP imaging technique is a pair of independent positioning mechanisms for the pump and probe pulses. The pump pulse is focused by the objective and its position on the sample is controlled by adjusting the Queensgate sample x-y stage (Figure 2.1). The probe beam is positioned independently using the x-y scanning mirrors (Figure 2.7), which is comprised of a set of two computer-controlled mirrors with motorized actuators on both the horizontal and vertical axes. In both dimensions, mirror #1 initially adjusts

the angle of the probe beam while mirror #2 compensates to redirect the probe back onto the aperture of the objective.
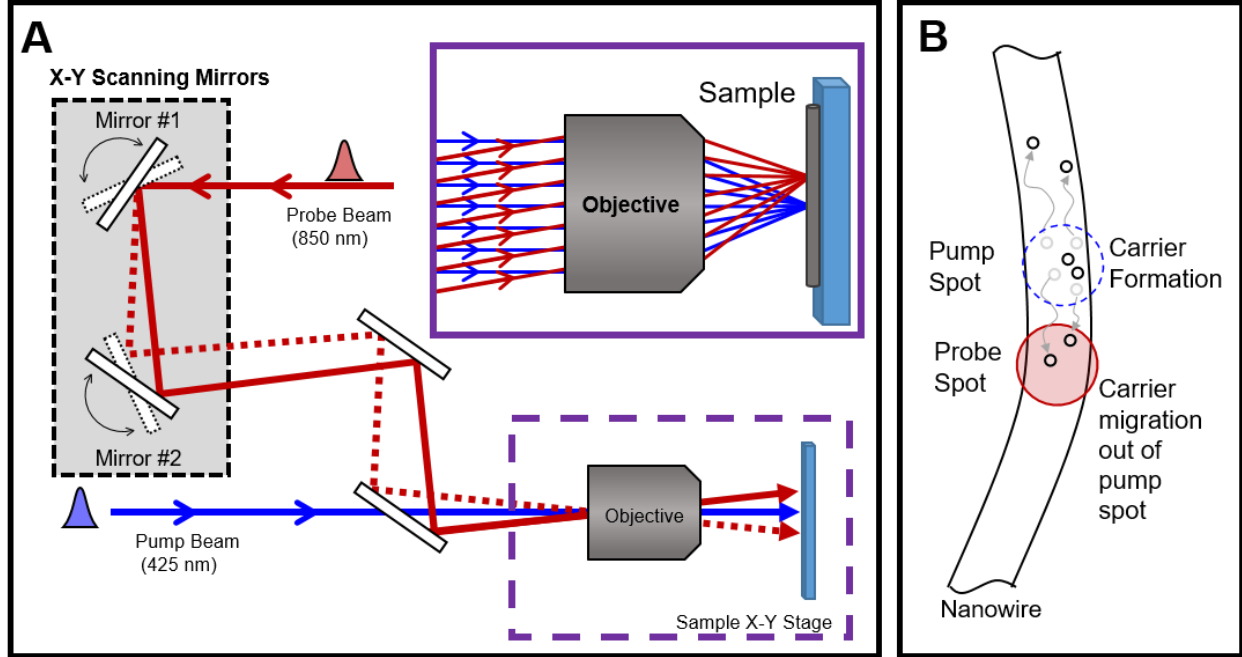
Figure 2.7: Schematic of spatially-separated pump-probe imaging. **(A)** The x-y beam scanner is a set of two computer-controlled mirrors with motorized actuators on both the horizontal and vertical axes. In both dimensions, Mirror #1 initially adjusts the angle of the probe beam while Mirror #2 compensates to redirect the probe beam back onto the back aperture of the objective. Inset is a zoomed in illustration of the pump and probe pulses entering the objective at different angles and focusing onto the sample at different positions. **(B)** The basic concept of the SSPP method. A nanostructure is photoexcited in one location and probed in another location. In this illustration, electrons are excited by the pump pulse and their migration along the axis of the wire is measured via the probe pulse.

Two motion controllers (Newport: ESP 301) control the vertical and horizontal axes of both scanning mirrors. When the pump and probe beams are aligned through the objective at an angle of 0°, they focus to the same position on the sample. The position of each mirror axis (4 total axes) can be set to 0 on the motion controllers independently. The horizontal and vertical axes are then independently calibrated assuming that motion along one axis does not

significantly alter the beam path along the other axis. To address this assumption, gimbal mirror mounts are used to place the center of rotation at the front surface of the optic, so there is no beam translation with rotational adjustments.

The horizontal and vertical axes are calibrated separately (with the other held at the 0 position) using a MATLAB script. The script moves the position of the vertical (or horizontal) axis, of Mirror #1, a set distance away from the zero position and then scans the corresponding vertical (or horizontal) axis of Mirror #2 while monitoring the signal that reaches the detector. Figure 2.8 shows a calibration of the vertical axis where the x and y-axes show the vertical displacement of Mirror #1 and Mirror #2, respectively. The color scale shown to the right of the plot in Figure 2.8 represents the magnitude of the signal at each (x,y) position. For example, when Mirror #1 is at -0.3 mm and Mirror #2 is at -0.25 mm, no signal is measured at the detector because the beam no longer travels through the aperture of the objective. Once Mirror #2 reaches a position near 0.25 mm, the beam is aligned through the objective and transmitted signal is detected. The slope of a linear fit of the maximum signal value at each x position represents the gear ratio of Mirror #2 to Mirror #1. The gear ratio is how far the Mirror #2 motor must move to compensate for the motion of Mirror #1 so that the beam travels through the aperture of the objective. The gear ratios are used as input parameters for another MATLAB script that links Mirror #1 and Mirror #2 such that Mirror #2 automatically moves with adjustments to Mirror #1.

Other input parameters set the mirrors' scan speed and area to be scanned in units of mm of

Mirror #1 actuator travel.
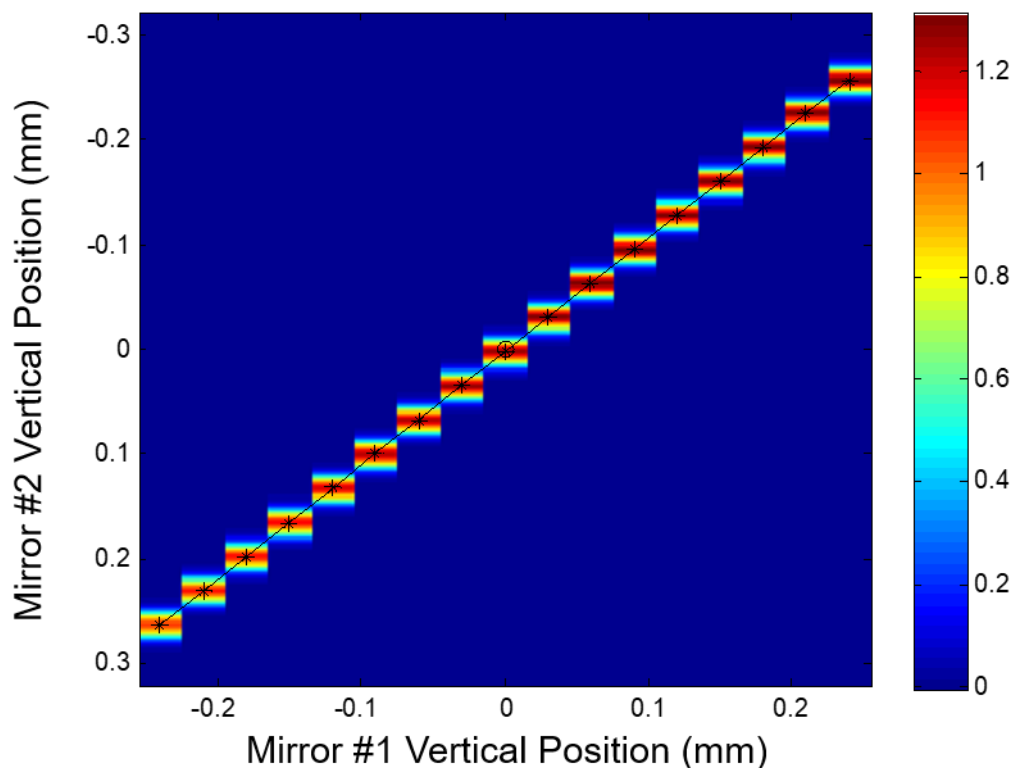
Figure 2.8: Mirror Calibration. A representative calibration plot for the vertical mirror axes. The vertical position of Mirror #1 (x-axis) is scanned from -0.3 mm to 0.3 mm. At each position, the vertical position of Mirror #2 (y-axis) is scanned. The magnitude of the signal at each (x,y) position is represented on the color scale shown to the right. The slope of a linear fit of the maximum signal value at each x position represents the gear ratio of Mirror #2 to Mirror #1.

To correlate mm of actuator movement with microns of movement on the sample, we simply compare the scanning mirror image to an image collected by scanning the Queensgate x-y sample stage with the probe beam fixed at the zero position. Another MATLAB script is used to convert mm of actuator movement to microns of spatial movement across the sample by

multiplying the scanning mirror image by x and y scaling factors so that both images are displayed in units of microns.

2.3. Data Collection Modes

Our pump-probe microscope can operate in two configurations; SOPP and SSPP configurations. These two configurations result in four possible modes of measurement that provide complementary information on the spatial and temporal excited state phenomena in nanomaterials. Figure 2.9 illustrates the spatial and temporal excited state phenomena that are measured in the SOPP and SSPP configurations.
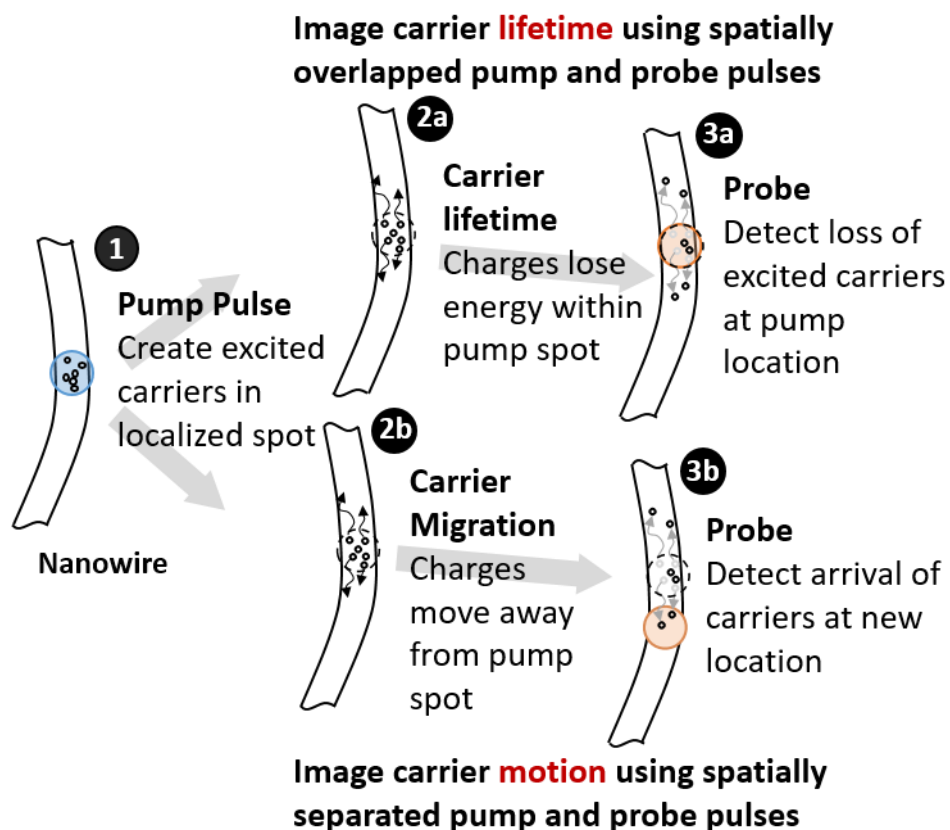
Figure 2.9: Charge carrier dynamics in a semiconductor nanowire. (1) Pump pulse photoexcited charge carriers in a localized spot on the NW (blue circle)**. (2a)** SOPP measures the carrier lifetime within the pump spot. **(2b)** The probe pulse (orange circle) detects the loss of excited carriers within the pump spot or **(3a)** SSPP measures carrier migration out of the pump spot **(3b)** The probe (orange circle) is spatially offset from the pump detects the arrival of carriers at a new location.

The SOPP (Figure 2.9.2a and 2.9.3a) configuration measures the charge carrier lifetime within the localized pump spot on a semiconductor nanowire (or nanoflake). However, the SSPP (Figure 2b and 3b) configuration measures the charge carrier migration outside of the pump spot, allowing the determination of transport dynamics. More details about each mode of data collection are discussed below.

2.3.1. Spatially-Overlapped Pump-Probe Configuration

In the first configuration, the pump and probe beams are spatially overlapped on a specific position on the sample and the pump-probe delay time is scanned using the optical delay stage. The resulting data are similar to the scan illustrated in Figure 2.5. Another example of this operational mode is shown in Figure 2.10A where spatially overlapped pump-probe (SOPP) transients are collected at two different points on a tungsten disulfide nanoflake (WS_2 NF). The points of collection are illustrated in the inset diagram with color-coded circles. Here, the blue trace corresponds to data collected at the NF edge, while the orange trace was collected in the interior of the NF. The spatial resolution of the microscope enables comparison of dynamics at different regions along a single nanostructure. For example, the signal in the NF interior region is much longer lived than the edge regions. This conclusion is further supported by the images in Figure 2.10C.
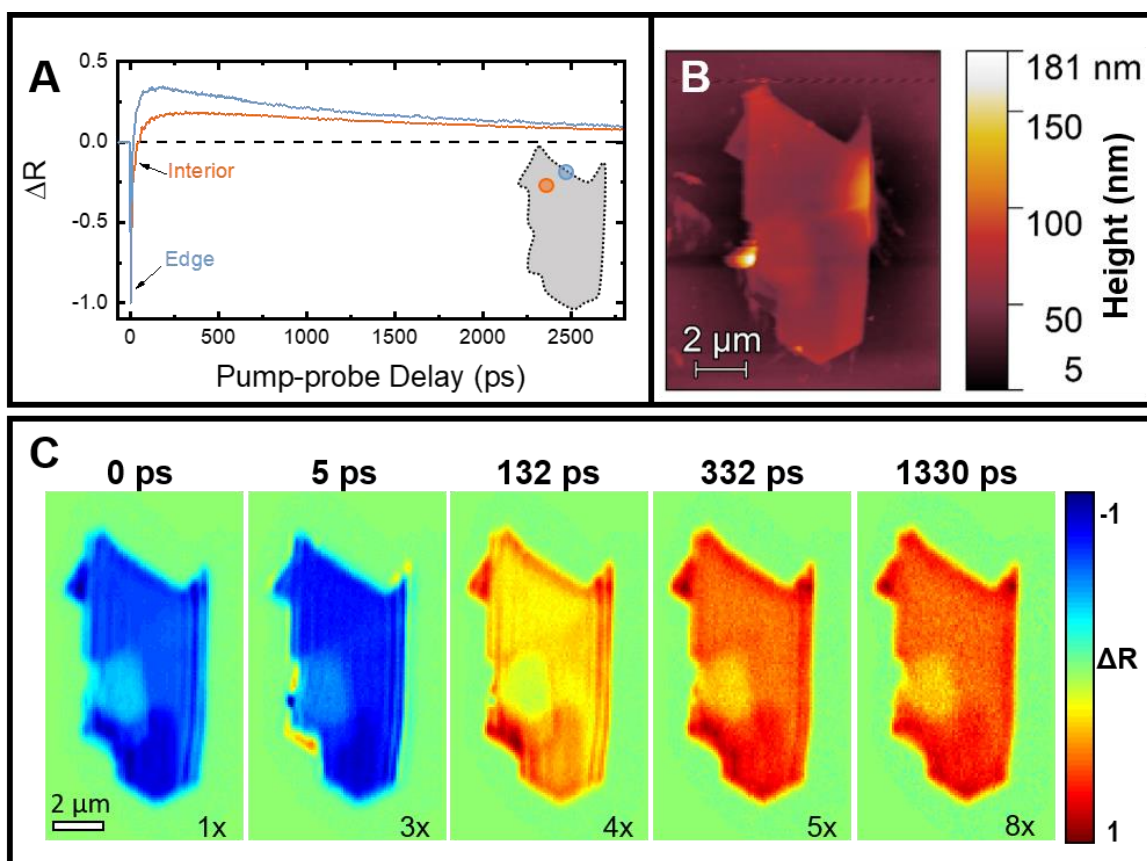
Figure 2.10: SOPP imaging of tungsten disulfide nanoflake. (**A**) Spatially-overlapped transient decay curves for points at the edge and interior of the NF collected in reflective pump-probe mode. Inset is the NF diagram with the location of data collection indicated by colored circles. The blue curve was collected at the edge of the NF, while the orange curve was collected in the flake interior. (B) AFM image of WS_2 NF. (**C**) SOPP images of the WS_2 NF at 0 ps, 5 ps, 132 ps, 332 ps, and 1330 ps pump-probe delays.

The second mode of operation is SOPP imaging, where the pump and probe beams are focused at the same focal point, and the x-y sample stage is raster scanned across the focused beams at fixed pump-probe delays. The spatial variation in the decay kinetics is easily ascertained by collecting images at a series of delay times. This is clear in Figure 2.10C, where one can easily see that in the interior regions of the WS_2 NF, the excited carriers have longer

lifetimes than in the NF edge regions, as corroborated by the SOPP transient delay scans discussed above.

2.3.2. Spatially-Separated Pump-Probe Configuration

The third mode is SSPP imaging. In this mode, the pump is held fixed at a specific position on the sample and the pump-probe delay is set by the optical delay line. The probe is then scanned over the field of view to provide a spatial map of the excitation at a particular time. By collecting a series of frames over several delay times, one can produce "movies" depicting the spatial evolution of the excitation. In Figure 2.11A, the frames depict the spreading and recombination of photoexcited charge carriers (red positive-going signal) and thermal transport (blue negative-going signal) in a single Ge NW whose position is represented by the gray dashed line. Thermal transport takes place on time scales that are significantly longer than the ~2ns delay that can be achieved with an optical delay stage. The synchronized AOMs are used to access pump-probe delays that extend out to 100 ns, allowing us to directly image thermal diffusion. Figure 2.12 illustrates how we can image long-lived thermal transport by select subsequent pump pulse out of the 80 MHz pulse train.

In the fourth mode, the pump and probe beams are separated at a fixed distance (Δx) and the delay stage is scanned, analogous to the SOPP configuration (Figure 2.10A). For pump-probe experiments, it is important to note that although the probe scanning mechanism alters the path of the probe beam, the geometry is such that the excess path length introduced by the tilt of the first mirror is almost completely compensated with the tilt second mirror. As a result, there is little (<0.5 ps) variation in the pump-probe delay as the probe beam is moved.
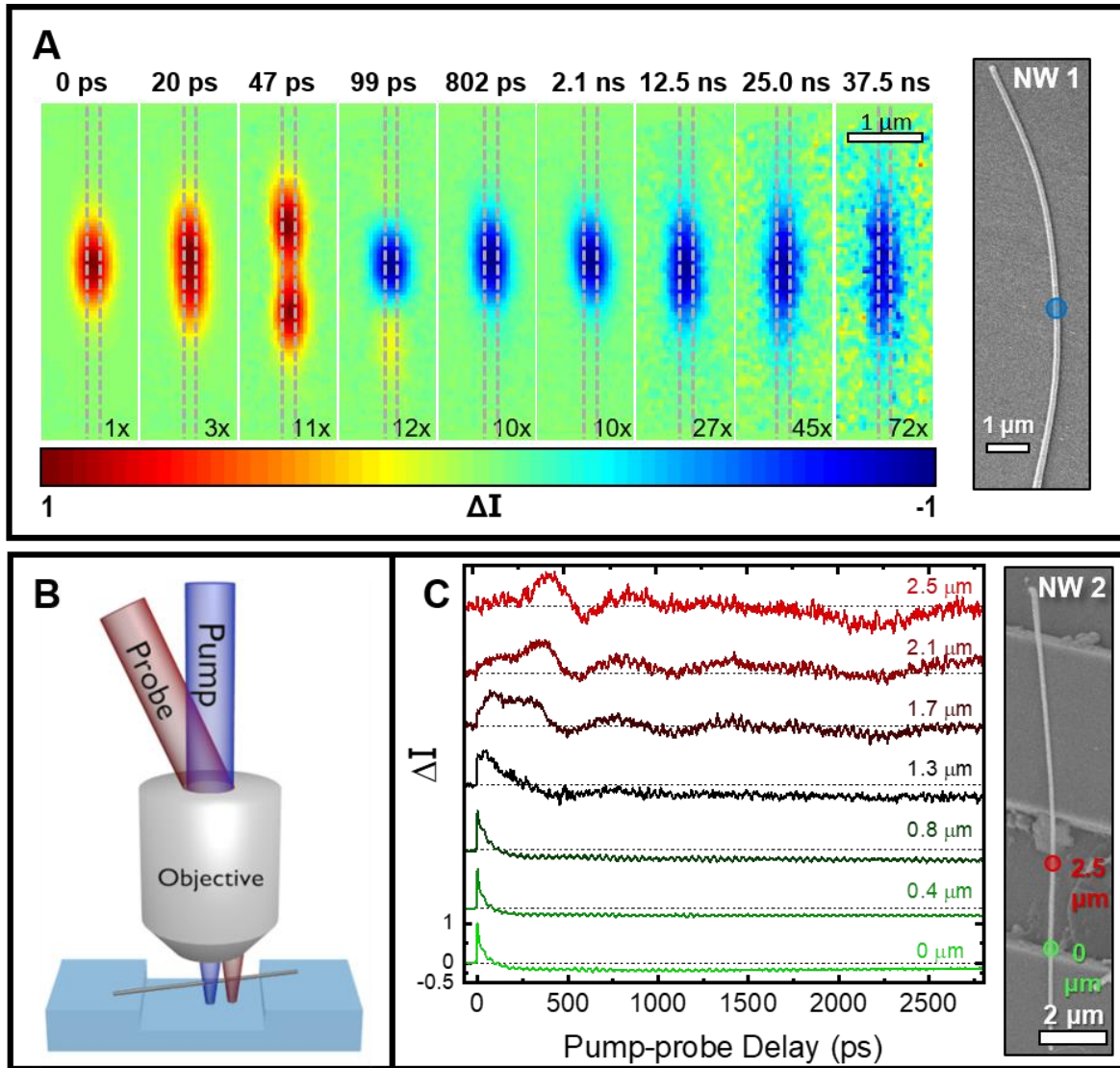
Figure 2.11: Kinetics of charge carrier, thermal, and acoustic phonon transport in Ge NWs. (A) SSPP images collected at delay times denoted above each image on NW1 (in transmission pump-probe mode). The scale bar is 1 μm. Dashed gray lines are guides indicating the location of the NW. Each image is depicted using a normalized color scale with the normalization factor denoted in the lower right corner. Inset is the SEM image of NW1 with the location of data collection indicated by a blue circle. **(B)** Illustration of SSPP imaging and transient configuration. **(C)** SSPP transients collected on suspended NW2 at pump and probe separations (Δx) denoted in the upper right of each transient. The SEM image of NW2 with the location of the probe indicated by a red circle, with the pump (green circle) fixed at the 0 μm location for each trace.

An example of spatially-separated pump-probe (SSPP) transient collection is shown in Figure 2.11C for single a Ge NW. The nanowire is excited by the pump pulse in a single location and the transient data is collected at seven pump-probe spatial separations (Δx) ranging from 0-2.5μm. The green trace corresponds to data collected in the spatially-overlapped configuration (i.e. $\Delta x = 0$ μm) while the rest of the data was collected in SSPP configuration. The delayed rise in signal for the SSPP data corresponds to the time it takes for excited carriers and vibrational motion to travel a distance of Δx. As Δx increases across the trench, a low-frequency phonon mode propagates along the NW axis. In order to observe the propagation of vibrational motion, the NW was suspended across a trench in the substrate. The development process for the trench substrates is described in section 2.4.
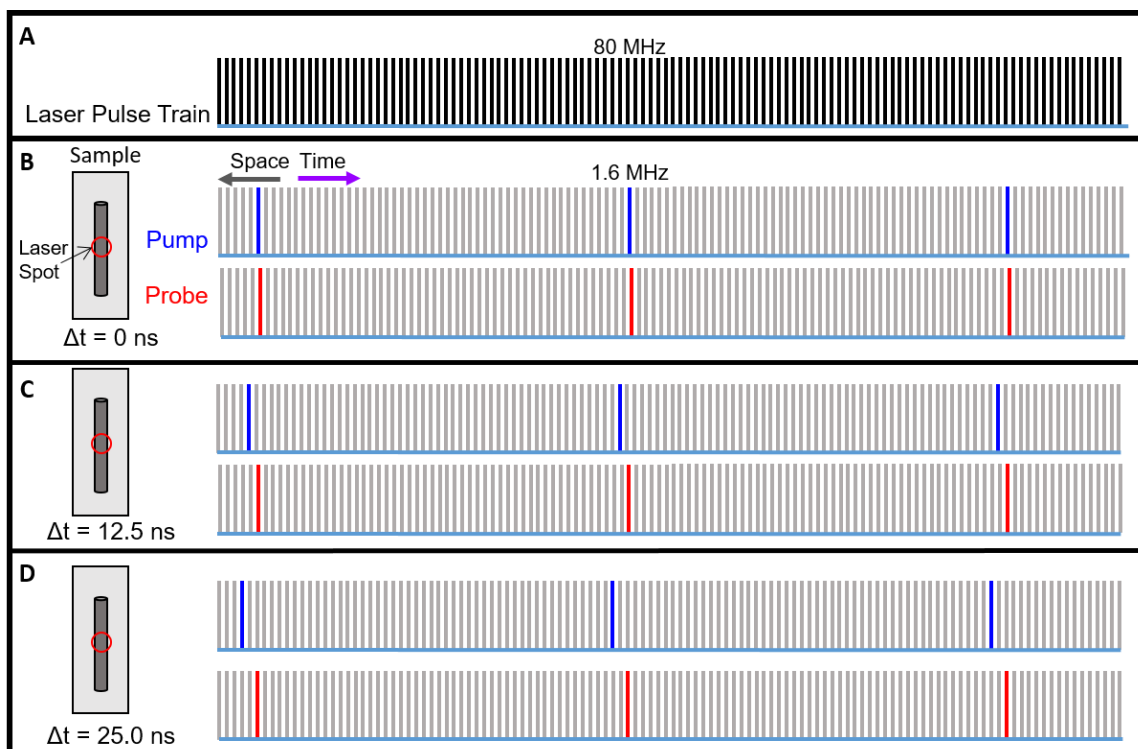
Figure 2.12: Schematic of synchronized AOM pulse picking. (A) The pulse train out of the Tsunami laser with a repetition rate of 80 MHz. **(B)** AOM pulse pickers are synchronized to have a zero-delay between the two pulse trains. The gray pulses are the rejected pulses while the picked pulses are shown in blue or red for the pump and probe AOMs, respectively. **(C)** Picking subsequent pump pulses out of the laser pulse train allows the pump and probe to be offset temporally by 12.5 ns. **(D)** Pulses offset by 25 ns allow for imaging of thermal and long-lived excited state populations on the tens of nanosecond time scale not achievable with the optical delay stage.

Each AOM pulse picker reduces the repetition rate of the laser pulse train to 1.61 MHz. The delay between the pump and probe pulse pickers is set with the delay generator. The AOMs are synchronized so the pump and probe pulse pair arrive at the sample at the same time (shown in Figure 2.12B). Selecting a previous pump pulse in laser pulse train (Figure 2.12C) offsets the temporal delay between the pump and probe pulses by 12.5 ns. This process allows us to image dynamics on the nanoscale time scale in 12.5 ns increments (Figure 2.12D). More details and examples of these experiments will be provided in the following chapters.

2.4. Trench Substrates

To correlate structural features to dynamical phenomena, it is essential to be able to relocate specific nanostructures in an SEM or AFM and image the nanostructure where dynamics were collected. Depositing nanostructures on a registry pattern allows us to relocate the exact location where dynamics were collected in another imaging instrument. Previously, we used gold plated registry patterns to mark out a grid of numbered rows and columns for this purpose. However, the process for creating these substrates was tedious and produced few usable substrates. To image acoustic phonon dynamics in Ge NWs, the NWs needed to be suspended over trenches to reduce the mechanical coupling between the NW and the substrate. Thus, I needed to design a new registry pattern that incorporated trenches into the registry grid.

The trench substrates are made using photolithography and deep reactive ion etching of quartz slides. A custom photomask was designed with two registry grid patterns. Each registry pattern includes numbered rows and lettered columns. The trench registry pattern has periodic trenches ranging in width from 5-15 μm and alternate between being horizontally or vertically aligned with the lettered columns. The other registry pattern only contains the numbered columns and lettered rows for use in other microscopy experiments that do not require suspending nanostructures. This increases the functionality and future applications of the substrates without having to redesign a new photomask.

35
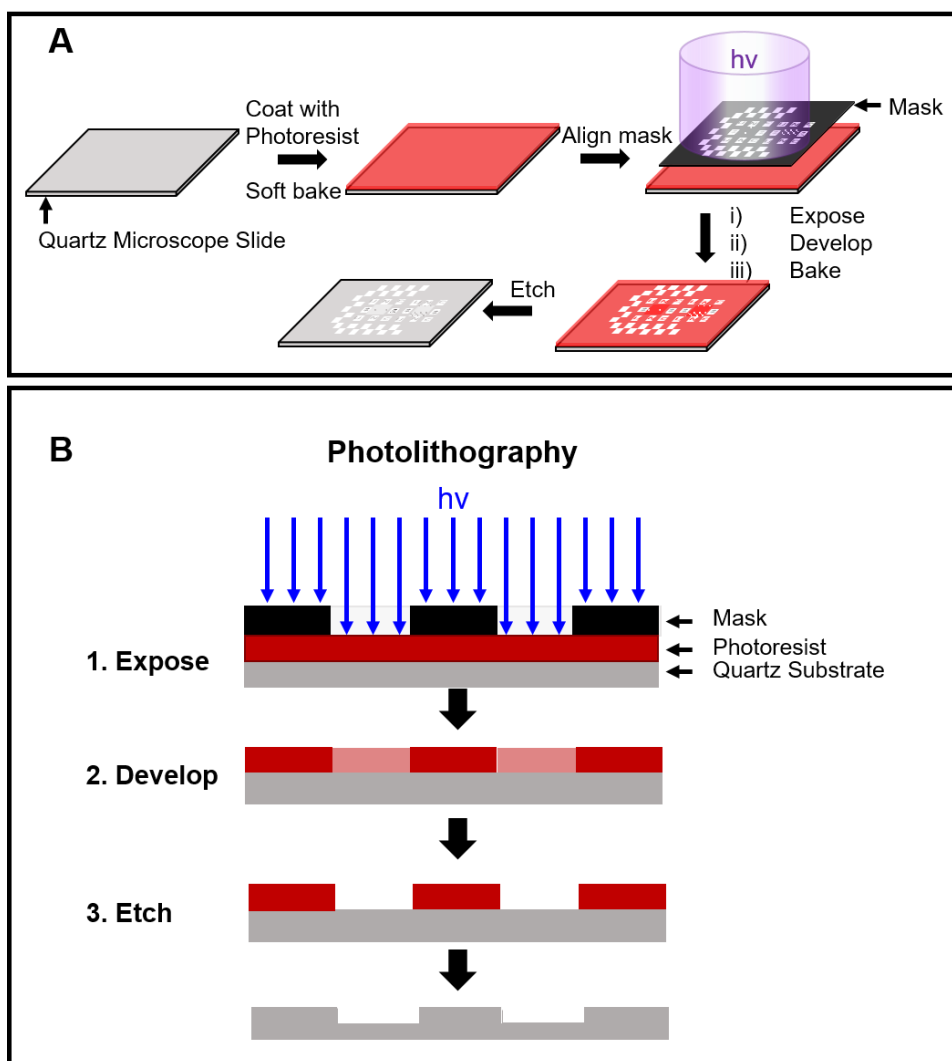
Figure 2.13: Photolithography of quartz substrates. **(A)** A quartz microscope slide is coated with a photoresist using a spin coater and baked. The slide is then loaded into the mask aligner with the custom mask and exposed to UV light. The exposed slide is developed to remove the dissolved polymer revealing the photolithography pattern in the polymer and baked again. The slide is then etched with DRIE to etch the pattern into the quartz surfaced. **(B)** Exposing a positive photoresist to UV through a mask causes a chemical change in the polymer that, once soaked in the developer solution, washes away the exposed photoresist. DRIE then etches the surface of the photoresist and exposed quartz, transferring the photolithography pattern into the substrate.

Figure 2.13 describes the photolithography process that generates the trench substrate registry patterns. Quartz slides were cleaned with acetone and isopropyl alcohol. A spin coater

was used to coat the quartz slide with a thin layer positive photoresist polymer (MicroChem S-1805 Photoresist) at 500 rpm for 15 s and then 3000 rpm for 30 s. The slides were then baked at 115 °C for 1 minute to adhere the polymer to the quartz. A mask aligner (Karl Suss MA6/BA6) exposes the photoresist through a photomask to generate the registry pattern into the polymer.

Using a positive photoresist with the mask leaves behind the polymer that was not exposed to the UV light. The slides were exposed to UV for 10 s and developed with MZ-319 (MicroChem) developer solution. The UV light changes the chemical composition within the exposed sections of the polymer, which breaks apart the polymer when developed. The slides are baked post development for 1 min at 115 °C to evaporate leftover developer solution. To etch the trench registry pattern into the quartz surface, the patterned polymer slides undergo nanofabrication using deep reactive ion etching (DRIE). The back of the quartz slide is coated with a thermal paste to conduct heat away from the slide into the aluminum sample holder during the etching process. The sample holder is loaded into the DRIE (Alcatel AMS 100) and etched using octafluorocyclobutane (C_4F_8) (17 sccm) and argon (150 sccm) gases for 5 mins. The DRIE generates a high-density plasma and ionized gas that bombards the surface and etches it away. The polymer-coated sections prevent the top of the quartz from being etched while the sections of exposed quartz create trenches ~0.8-1 µm deep with relatively straight vertical features. After DRIE, the slides are washed with acetone to remove any remaining polymer and thermal paste. SEM images of the resulting etched substrates are shown in Figure 2.14.
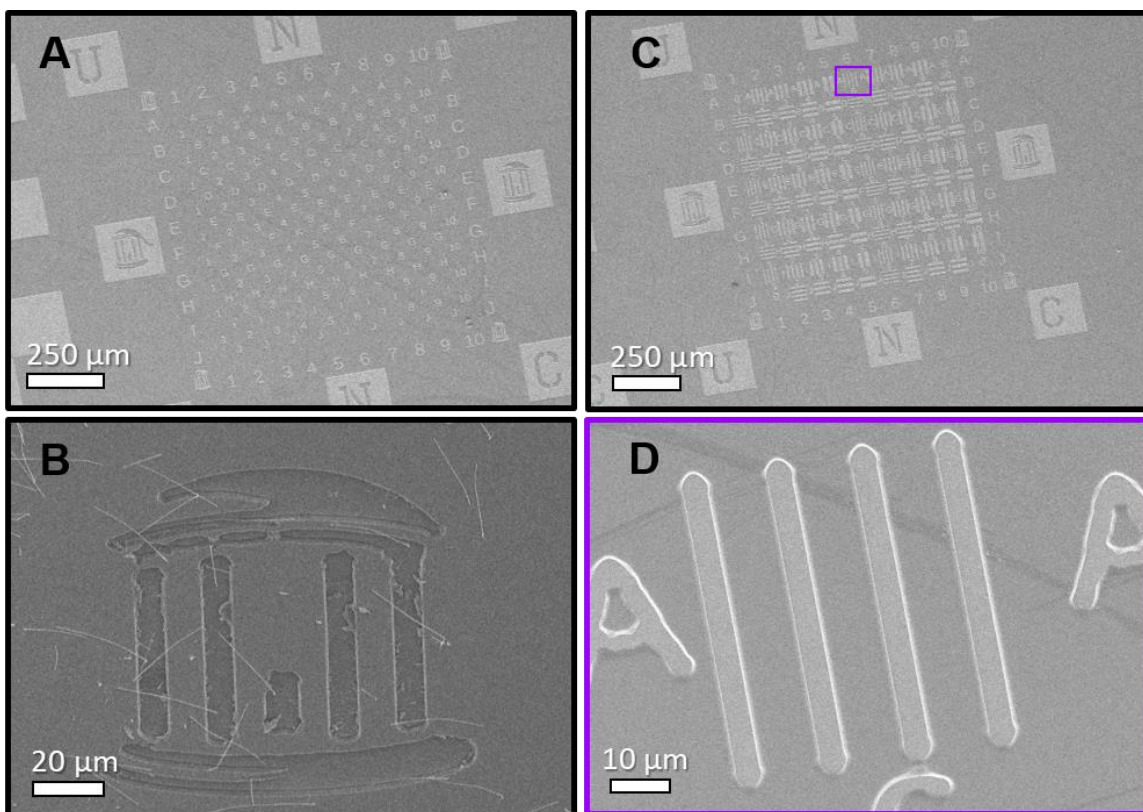
Figure 2.14: SEM images of quartz substrate (A) Registry Pattern with columns of numbers and rows of letters etched into the quartz microscope slide surface. **(B)** Old Well image etched into the quartz surface with Ge NWs suspended across. **(C)** Trench registry pattern with trenches alternating between vertical and horizontal orientation relative to the numbered and lettered grid pattern. The trenches range in width from 5 to 15 μm, which nanostructures can be suspended across. **(D)** Zoomed in on a section of trench registry pattern outlined in the purple box in 2.14C.

SEM images of the final trench substrates produced by photolithography and DRIE of quartz microscope slides are displayed in Figure 2.14. The entire etched substrate pattern is ~2 mm wide and includes two registry grids, one with a number/letter grid system and the other pattern having the number/letter grid with trenches. The registry pattern (Figure 2.14A) is surrounded by a large checkerboard pattern to make locating the registry/trench patterns and focusing the microscope in our bright field microscope configuration easier. Next to the registry pattern is the trench pattern (Figure 2.14C). Having both patterns on the same sample increases

the number of experiments that can be done on one sample. The etched surface allows

nanostructures, such as Ge NWs, to be suspended and reduce the mechanical and thermal

coupling between the NW and substrate. In Figure 2.14B, Ge NWs are suspended across the

UNC Old Well, allowing us to image vibrational motion across the NW axis. The trenches

formed from photolithography and DRIE (Figure 2.14D) are approximately 800 nm to 1 µm

deep with relatively vertical side walls.

REFERENCES

1. Grumstrup, E. M.; Cating, E. M.; Gabriel, M. M.; Pinion, C. W.; Christesen, J. D.; Kirschbrown, J. R.; Vallorz, E. L.; Cahoon, J. F.; Papanikolas, J. M., Ultrafast Carrier Dynamics of Silicon Nanowire Ensembles: The Impact of Geometrical Heterogeneity on Charge Carrier Lifetime. *The Journal of Physical Chemistry C* 2014, *118* (16), 8626-8633.

2. Grumstrup, E. M.; Gabriel, M. M.; Cating, E. M.; Pinion, C. W.; Christesen, J. D.; Kirschbrown, J. R.; Vallorz, E. L.; Cahoon, J. F.; Papanikolas, J. M., Ultrafast Carrier Dynamics in Individual Silicon Nanowires: Characterization of Diameter-Dependent Carrier Lifetime and Surface Recombination with Pump–Probe Microscopy. *J. Phys. Chem. C* 2014, *118* (16), 8634-8640.

3. Mehl, B. P.; Kirschbrown, J. R.; House, R. L.; Papanikolas, J. M., The End Is Different Than the Middle: Spatially Dependent Dynamics in ZnO Rods Observed by Femtosecond Pump–Probe Microscopy. *The Journal of Physical Chemistry Letters* 2011, *2* (14), 1777-1781.

4. Gabriel, M. M.; Grumstrup, E. M.; Kirschbrown, J. R.; Pinion, C. W.; Christesen, J. D.; Zigler, D. F.; Cating, E. E.; Cahoon, J. F.; Papanikolas, J. M., Imaging Charge Separation and Carrier Recombination in Nanowire p-i-n Junctions Using Ultrafast Microscopy. *Nano Lett.* 2014, *14* (6), 3079-87.

5. Mehl, B. P.; Kirschbrown, J. R.; Gabriel, M. M.; House, R. L.; Papanikolas, J. M., Pump-Probe Microscopy: Spatially Resolved Carrier Dynamics in ZnO Rods and the Influence of Optical Cavity Resonator Modes. *J. Phys. Chem. B* 2013, *117* (16), 4390-8.

6. Grumstrup, E. M.; Gabriel, M. M.; Pinion, C. W.; Parker, J. K.; Cahoon, J. F.; Papanikolas, J. M., Reversible Strain-Induced Electron-Hole Recombination in Silicon Nanowires Observed with Femtosecond Pump-Probe Microscopy. *Nano Lett.* 2014, *14* (11), 6287-92.

7. Gabriel, M. M.; Kirschbrown, J. R.; Christesen, J. D.; Pinion, C. W.; Zigler, D. F.; Grumstrup, E. M.; Mehl, B. P.; Cating, E. E.; Cahoon, J. F.; Papanikolas, J. M., Direct Imaging of Free Carrier and Trap Carrier Motion in Silicon Nanowires by Spatially-Separated Femtosecond Pump-Probe Microscopy. *Nano Lett.* 2013, *13* (3), 1336-40.

8. Cating, E. E.; Pinion, C. W.; Van Goethem, E. M.; Gabriel, M. M.; Cahoon, J. F.; Papanikolas, J. M., Imaging Spatial Variations in the Dissipation and Transport of Thermal

Energy within Individual Silicon Nanowires Using Ultrafast Microscopy. *Nano Lett.* 2016, *16* (1), 434-9.

9.   Cating, E. E. M.; Pinion, C. W.; Christesen, J. D.; Christie, C. A.; Grumstrup, E. M.; Cahoon, J. F.; Papanikolas, J. M., Probing Intrawire, Interwire, and Diameter-Dependent Variations in Silicon Nanowire Surface Trap Density with Pump-Probe Microscopy. *Nano Lett.* 2017, *17* (10), 5956-5961.

CHAPTER 3: OBSERVATION OF ULTRAFAST PHONON PROPAGATION IN GERMANIUM NANOWIRES USING FEMTOSECOND PUMP-PROBE MICROSCOPY

The excited state dynamics in individual Ge nanowires (NWs) are imaged using ultrafast pump-probe microscopy with high spatial (~400 nm) and temporal (~500 fs) resolution. Photoexcitation of the NW by a focused femtosecond laser pulse promotes electrons from the valence band to the conduction band within a 400 nm segment of the 20-30 μm long NW. The localized excitation is then probed by a delayed femtosecond pulse whose position with respect to the pump pulse is precisely controlled. The pump-probe signals contain contributions from free carriers, thermal excitation, and impulsively excited acoustic phonons, the latter of which are detected in the time-domain as a coherent oscillation in the pump-probe signal. Examination of an ensemble of NWs with diameters (d) ranging from 50-300 nm shows that the coherence frequency is inversely proportional to d, consistent with excitation of a radial breathing mode (RBM). In addition, experiments performed with spatially-separated pump and probe beams show that the vibrational motion is not confined to the excitation region, but rather spreads as much as 2.5 μm along the NW axis during the first 3 ns after excitation. Spatially-separated pump-probe microscopy also reveals the creation of a shockwave that travels along the NW at ~6500 m/s or about 20% faster than the speed of sound in bulk Ge.

42

3.1. Introduction

Pump-probe experiments performed on semiconductor nanowires (NWs) often reflect a variety of dynamical phenomena, including carrier trapping, recombination, and thermal relaxation, as well as coherent processes arising from impulsive excitation of lattice phonons. The structural heterogeneity present in semiconductor samples complicates pump-probe signals, making it difficult to interpret them in terms of fundamental physical phenomena.[1, 2] Even a first-order (or pseudo first-order) kinetic process such as electron-hole recombination is observed as a multiexponential decay with a distribution of lifetimes that correspond to the range of diameters found in the ensemble.[1-5] The coherent response arising from impulsive excitation of acoustic phonons is also affected by structural heterogeneity,[6] as the slight variation in phonon frequencies due to different NW diameters gives rise to heterogeneous dephasing that causes the loss of the coherent signal over just a few vibrational periods,[7] obscuring the true linewidth.

We have used ultrafast pump-probe microscopy to circumvent this heterogeneity by performing transient transmission measurements on a single structure with diffraction-limited spatial resolution. Measurements performed using a spatially-overlapped pump-probe (SOPP) configuration are analogous to conventional pump-probe spectroscopies, but implemented in a microscopy mode. This configuration allows one to follow the excited state dynamics from different structures, or different points within the same structure when an object is larger than the tightly focused pump and probe beams. Using this configuration, we discovered the presence of significant wire-to-wire variation in the surface recombination velocity (*i.e.* surface quality) in Si NWs, even when the NWs were selected from the same growth sample.[2] Work in our group also revealed strikingly different dynamics taking place at different points within individual nanostructures, including the partitioning between trap

43

and band-edge electron-hole recombination in needle-shaped ZnO rods[8, 9] and strain-induced

recombination in bent Si NWs[10]. Measurements performed using a spatially-separated

pump-probe (SSPP) microscopy mode, in which independent scanning mechanisms for the

two beams enable a structure to be excited in one location and probed in another, allow for

the characterization of transport phenomena. We have used this SSPP configuration to

directly visualize the diffusion of photogenerated carriers[11] and the spread of thermal

excitation in Si NWs,[12] as well as charge separation in Si NWs encoded with axial p-i-n

junctions.[13]

Here, we report on the application of pump-probe microscopy methods to the study of

Ge NWs. Like Si NWs, the transients obtained from Ge NWs include contributions from

electron-hole recombination, carrier diffusion, and thermal relaxation. However, unlike Si,

the Ge NWs also show clear evidence for impulsive excitation of acoustic modes. Low-

frequency acoustic phonons have been observed in pump-probe transient absorption and

microscopy experiments of many metal[14-27] and semiconductor nanostructures[7, 28, 29]. In the

vast majority of these examples,[30, 31] the nanostructures are smaller in size than the pump

beam, thus generating a uniform excitation over the entire structure. The pump and probe

spots in our experiment, on the other hand, are smaller than the NW length, resulting in

phonon excitation in a localized segment of the wire. We observe two characteristic acoustic

phonon modes. Coherent oscillations with a 10-20 ps period are observed at the location of

the pump pulse, which we attribute to the excitation of a radial breathing mode (RBM) of the

NW. The coherence persist for 3-5 ns when the NW is mechanically decoupled from the

substrate, and spatially-separated experiments show that this excitation slowly spreads along

the wire axis over many vibrational periods. Impulsive excitation also creates a shock wave

that is observed 3-5 µm away from the pump pulse as it propagates along the NW at close to the speed of sound.

3.2. Experimental

<u>NW Samples</u>: Germanium NWs were grown with Au catalysts using the vapor−liquid−solid (VLS) mechanism,[32] producing single-crystal wires with a native oxide (GeOx) shell after exposure to ambient conditions. For a typical growth, 20.0 standard cubic centimeters (sccm) of germane gas was flowed through the reactor using 100 sccm of hydrogen as carrier gas, while maintaining a total reactor pressure of 30 Torr. The reactor was held at 320 °C for 5 minutes to nucleate wire growth and then cooled (60 °C /min) to 260 °C for continued wire growth over 1.5 hours. The NWs were then dry-transferred from the growth chip to quartz substrates with trenches patterned by photolithography and etched by deep reactive ion etching. The wires studied here span trenches (5-15 µm wide) with several microns of the NW supported by the substrate on both ends. NWs were deposited on the registry patterned grid in order to relocate the exact NW in the scanning electron microscopy (SEM) to correlate dynamics to structural features, such as NW diameter.

<u>Ultrafast Microscope</u>: Pump-probe experiments were performed with a home-built microscope based on a mode-locked Ti: Sapphire laser.[11] In the setup, the 850 nm laser output is split by a 90:10 beam splitter and the two beams pass through synchronized acousto-optic modulators (AOMs), reducing their repetition rates to 1.6 MHz. The more intense fraction is directed through a β-barium borate (BBO) crystal to generate the 425 nm pump pulse while the lower-intensity component is used as the 850 nm probe. The probe is

quadruple-passed through a 253 mm mechanical stage, providing about 3.3 ns of optical delay. Access to pump-probe delays up to several hundred nanoseconds is achieved through the selection of different pulses from the 80 MHz pulse trains. The probe then passes through a set of computer-controlled scanning mirrors that change the angle of the beam as it enters the objective, allowing the probe to be focused to a spatially distinct point on the sample. The two beams are then attenuated using neutral density filters to 10 pJ/pulse and 4 pJ/pulse for the pump and probe, respectively. They are then recombined using a dichroic mirror and directed onto the back aperture of a microscope objective (100x, 0.8 NA), which focuses the pump and probe beams to 400 nm and 600 nm diffraction-limited spots at the sample. Individual nanostructures are placed within the laser focus using a 2-axis piezo scanning stage. The transmitted probe light is collected by a high NA condenser lens and detected by a balanced photodiode. The pump beam is modulated at 16 kHz and the pump-induced changes in the probe intensity (ΔI) are detected by lock-in amplification. With this microscope, we can measure the transient response of a single nanostructure with ~600 nm spatial resolution and ~500 fs time resolution, with a sensitivity of $\Delta I/I \sim 10^{-5}$.[11]

3.3. Results and Discussion

Spatially-overlapped pump-probe measurements on an individual Ge NW reveal a complex transient that has contributions from free carrier and thermal excitations, as well a low-frequency coherence arising from an acoustic phonon mode (Figure 3.1). This specific nanowire (denoted NW1) is ~153 nm in diameter and is typical of the structures studied here. The pump pulse excites an ~400 nm segment of the 20-30 µm long NW at the location indicated by the blue circle, promoting electrons from the valence band to the conduction

band with a carrier density of $\sim 10^{20}$ cm^{-3}.[33] The photogenerated carriers alter the absorption

and scattering properties of the Ge NW, causing the initial increase in the probe intensity

(positive-going signal), which decays over time as the carriers undergo electron-hole

recombination and migrate away from the point of excitation. The long-lived negative-going

signal arises from localized heating of the NW by the pump pulse, which we estimate based

on the amount of pump pulse energy deposited as thermal energy to be $\sim$150 K.[3, 11, 12, 34, 35]

This component decays over time as the thermal energy diffuses along the wire and

dissipates into the substrate.[12] Superimposed on top of the free carrier and thermal

contributions are time-dependent coherent oscillations that result from impulsive excitation

of a low-frequency radial breathing mode (RBM) due to rapid heating of the lattice.[4, 7, 30, 36, 37]

The periodic vibrational motion of the NW modulates the transient signal, perhaps through

strain-induced changes in the band structure or changes in the refractive index.[4, 7, 27, 38-44]
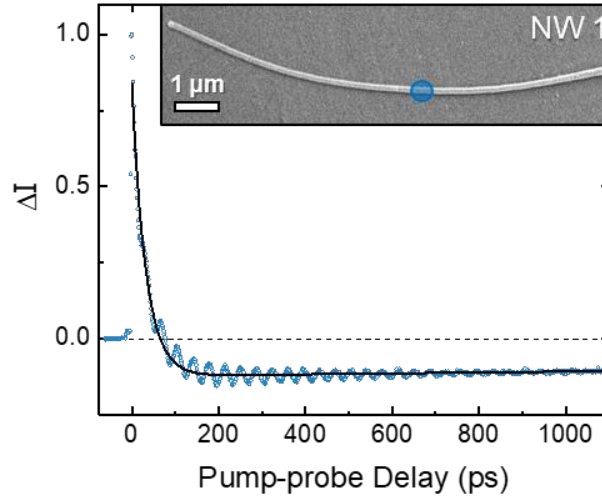
Figure 3.1: Transient obtained from a typical Ge nanowire (NW1) obtained with a spatially-overlapped configuration. The NW is excited at 425 nm (10 pJ/pulse) at the location of the blue circle in the corresponding SEM image (inset) and probed by a delayed 850 nm laser pulse directed at the same location. The nanowire is 153 nm in diameter and supported on a quartz substrate. The black curve is the biexponential fit.

3.3.1. Free Carrier Relaxation and Thermal Dissipation Dynamics

The overall form of the transient depicted in Figure 3.1 (neglecting the coherent oscillations) is reasonably well-described by a biexponential form, *i.e.*:

$$\Delta I(\Delta t) = A_P\, exp(-k_P\Delta t) + A_N\, exp(-k_N\Delta t) \qquad [3.1]$$

where the first and second terms correspond to the loss of the photogenerated carrier population (positive-going component) and thermal energy within the probe spot (negative-going component), respectively. We note that in this description, the decay rates ($k_P = (32$ ps$)^{-1}$ and $k_N = (7.2$ ns$)^{-1}$) have contributions from both population loss (*i.e.* recombination and

48

heat dissipation) and transport (*i.e.* carrier migration and thermal diffusion), and thus, they

are only effective rate constants.
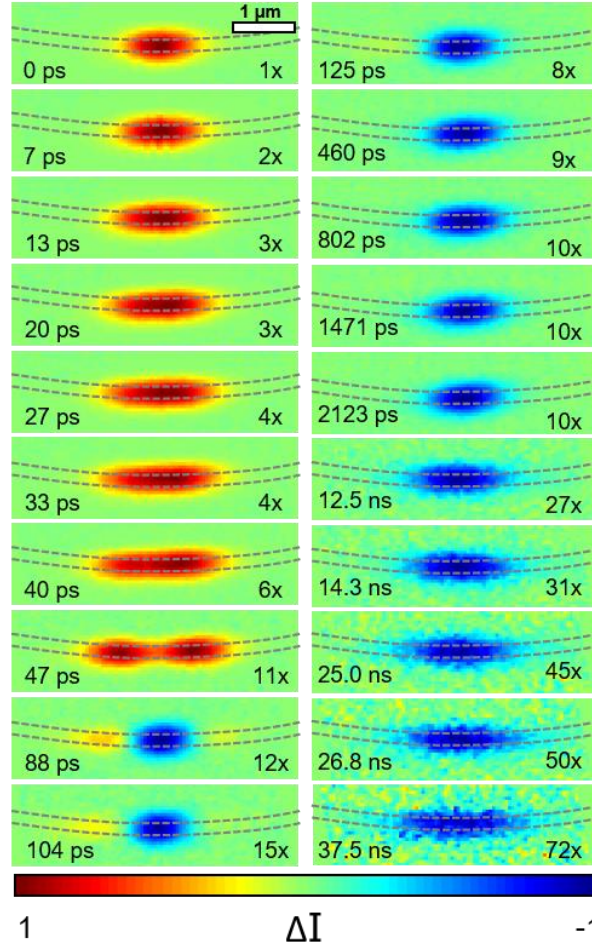
Figure 3.2: **SSPP images from NW1 obtained at different time delays** as indicated in the lower left corner of each image. Each image is plotted on a normalized color table with relative scaling factors in the lower right corner. The pump pulse energy was 10 pJ/pulse, and the excitation was located at the point marked by the blue circle in the SEM image (Figure 3.1). The NW location is denoted by the dashed line.

Transport phenomena are probed directly by SSPP experiments. Displayed in Figure

3.2 are SSPP images depicting the spread of the photoexcitation in NW1 for time delays

ranging from a few picoseconds to tens of nanoseconds.[11] The image at $\Delta t = 0$ ps shows the

spatial distribution of the photoinduced transparency. Over time this transparency spreads along the length of the NW as the quasi-neutral charge cloud diffuses. During this time, the electrons and holes recombine, resulting in a fading of the photoinduced transparency, and by 88 ps, the images are dominated by the absorptive component (*i.e.* blue feature) that corresponds to a localized thermal excitation. This thermal component also spreads along the NW, but at a slower rate, and even at ~2 ns it is only slightly larger than the initial excitation. By 30-40 ns the SSPP images show significant dispersal of the thermal excitation along the NW.

When the population decays through higher-order kinetic processes, the center of the excitation region will decay faster than the wings, resulting in an apparent spatial broadening of the pump-probe signal that is not due to transport. However, at sufficiently low excitation intensities, the pump-probe kinetics are independent of the photoinjected carrier density. In this regime, the signal decays uniformly across the excitation region, and as a result, the observed spreading of the pump-probe signal is due only to transport. This situation leads to a separation of the spatiotemporal signal into two factors, one that describes the time evolution of the size of the pump-probe signal, and the other its temporal decay. The separation applies to both the free carrier and thermal signals, resulting in the following expression: [3, 12, 13]

$$\Delta I(\Delta t, \Delta x) = \left[\alpha_C \, exp\left(\frac{-4 \ln 2 \, \Delta x^2}{\Gamma_C(\Delta t)^2} \right) \right] \left[\beta_C \frac{exp(-\Delta t/\tau_C)}{\Gamma_C(\Delta t)} \right]$$
$$+ \left[\alpha_T \, exp\left(\frac{-4 \ln 2 \, \Delta x^2}{\Gamma_T(\Delta t)^2} \right) \right] \left[\beta_T \frac{exp(-\Delta t/\tau_T)}{\Gamma_T(\Delta t)} \right]$$

[3.2]

where Δt and Δx are the temporal delay and spatial separation of the pump and probe spots on the sample, respectively. In this representation, the loss of the free carrier population and

the dissipation of heat are modeled as first-order decay processes with corresponding

lifetimes of τ_C and τ_T, respectively. The diffusional spreading of the free carrier and thermal

signals along the NW are described by the Gaussian expressions with time-dependent full-

width-at-half-maximum (FWHM) values given by

$$\Gamma_C(\Delta t) \;=\; \sqrt{\gamma_{pu}{}^2 + \gamma_{pr}{}^2 + 16\ln2\, D_C \Delta t} \qquad\qquad \text{[3.3a]}$$

$$\Gamma_T(\Delta t) \;=\; \sqrt{\gamma_{pu}{}^2 + \gamma_{pr}{}^2 + 16\ln2\, D_T \Delta t,} \qquad\qquad \text{[3.3b]}$$

where γ_{pu} and γ_{pr} are the FWHM sizes of the pump and probe spots (400 nm and 600 nm,

respectively), D_C is the ambipolar diffusion constant for the free carriers and D_T is the

thermal diffusivity.

(1.) <u>Overview of Kinetic Analysis</u>: In principle, all four kinetic constants (τ_C, D_C, τ_T, D_T)

could be obtained by fitting the set of SSPP images to these equations. However, global fits

of this nature are not robust due to the structure of the spatiotemporal data sets. The SSPP

images, for example, show the variation in the signal as a function of the pump-probe

separation, but only for a sparse selection of time delays, while the SOPP transient shows

how the signal varies with time delay, but only for a single overlap configuration. In

addition, because the SSPP images are collected sequentially, the relative intensity between two

images is known with less certainty when compared with two adjacent delay points in the SOPP

transient, which are collected closer together in time and are thus less susceptible to instrumental

drift.

Rather than pursuing a global analysis of these equations using the entire data set fit,

we take advantage of the separation of the transport and relaxation contributions and extract

the four parameters through a two-step process. In the first step, we analyze the spread in the

axial profile of SSPP images using the spatial portion of Eqn. 3.2, *i.e.*

$$\Delta I(\Delta x; \Delta t) = \eta_{C,\Delta t} \, exp\left(\frac{-4\ln 2\,\Delta x^2}{\Gamma_C(\Delta t)^2}\right) + \eta_{T,\Delta t} \, exp\left(\frac{-4\ln 2\,\Delta x^2}{\Gamma_T(\Delta t)^2}\right), \quad [3.4]$$

where $\eta_{C,\Delta t} = \alpha_C \cdot \beta_C \, exp(-\Delta t/\tau_C)/\Gamma_C(\Delta t)$, and likewise for $\eta_{T,\Delta t}$. While $\eta_{C,\Delta t}$ and $\eta_{T,\Delta t}$ both

depend upon Δt, for a given pump-probe delay they are constants and the axial profile only

depends upon the pump-probe separation, Δx. By fitting Eq. 4 to the series of axial profiles,

each collected at a different pump-probe delay, we can extract D_C and D_T without having to

rely on an accurate measure of the relative signal intensities from one SSPP image to the

next. Once D_C and D_T are determined, the lifetimes are then obtained by non-linear least-

squares fitting of $I(\Delta t) = I(\Delta t, 0)$, *i.e.*

$$\Delta I(\Delta t) = \kappa_C \frac{exp(-\Delta t/\tau_C)}{\Gamma_C(\Delta t)} + \kappa_T \frac{exp(-\Delta t/\tau_{Th})}{\Gamma_T(\Delta t)} \quad [3.5]$$

to the SOPP transient, where $\kappa_c = \alpha_C \cdot \beta_C$, and similarly for κ_T. This decay expression reduces

to a simple biexponential form in the limit that transport is slow compared to relaxation, a

case that is not applicable here.
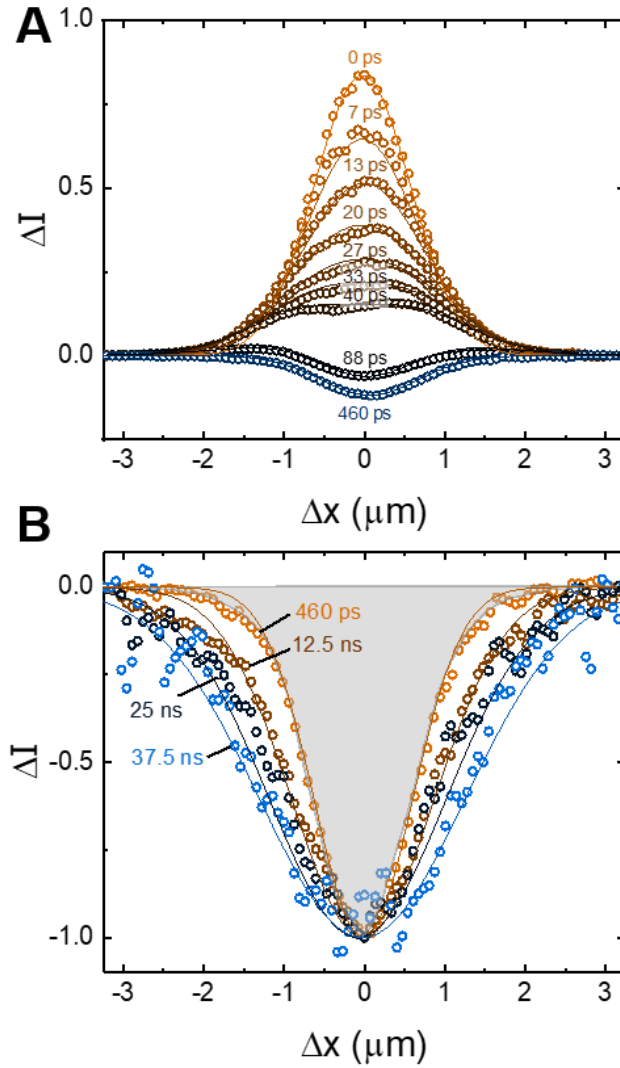
Figure 3.3: Quantifying thermal transport and carrier diffusion in NW1. The pump pulse energy was 10 pJ/pulse, and the excitation was located at the point marked by the blue circle in the SEM image (Figure 3.1). **(A)** Axial profiles depicting the spatial distribution of the pump-probe signal along NW1 during the first 460 ps after excitation. In this time window, the axial profile evolves from a photoinduced transparency at zero delay to a photoinduced absorption at 460 ps. **(B)** SSPP axial profiles for delays ranging from 460 ps to 37.5 ns. Each profile is normalized to -1, and the gray shaded area shows the size of the initial excitation as determined at 0 ps.

(2.) <u>Transport Coefficients</u>: Figure 3.3 depicts a series of axial profiles obtained from NW1.

Each profile was generated by integrating the SSPP image along the direction normal to the

NW axis. The positive-going profiles observed at early delays are dominated by the free-carrier signal and show clear lateral broadening as the signal decays in amplitude (Figure 3.3A). By 40-50 ps, the impact of the thermal excitation becomes increasingly apparent as the profile takes on a progressively more bimodal character. As the free carrier contribution disappears, all that remains is the negative-going thermal contribution, which at 460 ps has spread only slightly beyond the excitation region. While robust fits of Eqn. 3.4 to the axial profiles are possible at intermediate time delays, where the two contributions are clear, at earlier times the thermal contribution causes only a slight distortion in the shape of the axial profile. This situation leads to a strong dependency between the amplitudes and widths of the two Gaussian components, and less stable fits.

We circumvent the problem by first determining the thermal diffusivity using the axial profiles from 460 ps to 37.5 ns (Figure 3.3B). Over this time range, the thermal signal measurably spreads along the wire axis. However, because the free carrier contribution has completely decayed, the profiles can be fit by a single Gaussian function. The set of six normalized profiles were simultaneously fit to Eqn. 3.4 with $\eta_{C,\Delta t} = 0$ and $\eta_{T,\Delta t} = -1$. The fit treated D_T as a global fitting parameter and extracted a value of $D_T = 0.2$ cm^2/s. The thermal conductivity (k) is related to D_T by $k = \rho C_p D_T$, where ρ is the mass density (5.32 g/cm^3),[34] and Cp is the specific heat capacity (0.32 J/g·K)[45]. This expression yields $k = 29$ W/m·K, which is about a factor of two smaller than the ~60 W/m·K value for bulk Ge.[46-48] A similar reduction in thermal conductivity between the NW and bulk forms is also observed in Si.[12] As with Si, the smaller conductivity in the NW is likely the result of a reduced mean free path of the high-frequency optical phonons responsible for thermal transport.

The free carrier diffusion constant (D_C) is determined through a simultaneous fitting of Eq. 3.4 to the 10 SSPP axial profiles obtained during the first 125 ps after excitation. The fit is constrained by treating $D_T = 0.2$ cm^2/s as a fixed parameter. The fit is further constrained by determining the amplitudes for the free carrier and thermal components ($B_{C,\Delta t}$ and $B_{T,\Delta t}$, respectively) at each delay using the results of the biexponential fit to the SOPP transient (Figure 3.1) and then setting them to be fixed parameters, as well. Thus, the only adjustable parameter in the global fit of Eqn. 3.4 to the SSPP axial profiles is D_C. The best fit to the data is obtained when $D_C = 63.2$ cm^2/s, which is comparable to the value observed in bulk Ge.[49, 50]

(3.) <u>Lifetimes</u>: The SOPP transient depicted in Figure 3.1 is fit using Eqn. 3.5 with $D_C = 63.2$ cm^2/s and $D_T = 0.2$ cm^2/s, $\tau_C = 46$ ps and $\tau_T = 9.0$ ns. Both are longer than the observed lifetimes (k_P^{-1} and k_N^{-1}) extracted from the biexponential fit, which are influenced by transport processes, as discussed above. Electron-hole recombination in nanostructures can occur through a combination of mechanisms, including surface mediated mechanisms, as well as higher order processes such as Auger recombination that occur in the NW core.[5] Transients collected at a series of excitation intensities show that the lifetime is nearly constant for pump pulse energies up to ~5 pJ, after which it becomes shorter with increasing intensity. Thus, while recombination is likely dominated by surface-mediated processes, there appears to be a slight enhancement of the recombination rate at 8-10 pJ/pulse (and higher) due to higher-order kinetic processes. Effects of Auger recombination are also reported in ensemble pump-probe measurements performed on Ge NWs at similar excitation intensities,[4, 7] consistent with our observations. The carrier recombination time in Ge NWs is

markedly faster than that observed in Si NWs, which exhibit carrier lifetimes of 200-500 ps for NWs of comparable diameter.
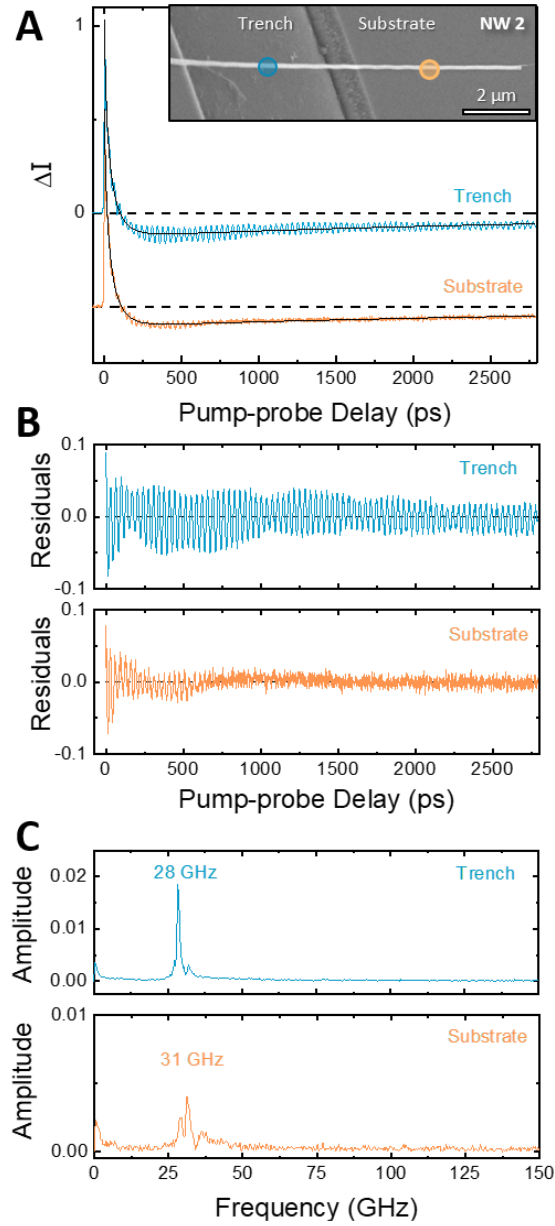
Figure 3.4. **Effect of substrate on phonon dynamics in NW2. (A)** SOPP kinetic traces obtained from substrate-supported (orange) and suspended (blue) sections of NW2. Solid black lines are best fits to Eqn. 3.5. Inset shows the SEM image with the trench (left) and substrate (right) visible. The positions at which transient scans were collected are highlighted by blue and orange circles. **(B)** Residuals from fitting yields coherent oscillations. **(C)** Frequency spectrum obtained by Fourier transform of residuals.

Shown in Figure 3.4 are SOPP transients obtained from a 125 nm diameter Ge NW suspended across a 5 µm trench etched into a quartz substrate. Two transient data sets are shown in Figure3.4A, one from the section suspended over the trench and the other from a segment in contact with the quartz substrate. Both traces were fit to Eqn. 3.5 and the resulting fit residuals, which isolate the coherent amplitude oscillations, are depicted in Figure 3.4B. While the free carrier and thermal contributions are largely unaffected by decoupling the NW from the substrate, suspending the NW increases the amplitude of the coherent signal and extends its lifetime by as much as a factor of six compared to the section in contact with the substrate (Figure 3.4B). Fast Fourier transform (FFT) of the residuals yields the phonon frequency spectra depicted in Figure 3.4C. Both sections of the NW show an intense frequency component near 30 GHz, indicating that interaction with the substrate does not significantly affect the mode frequency.
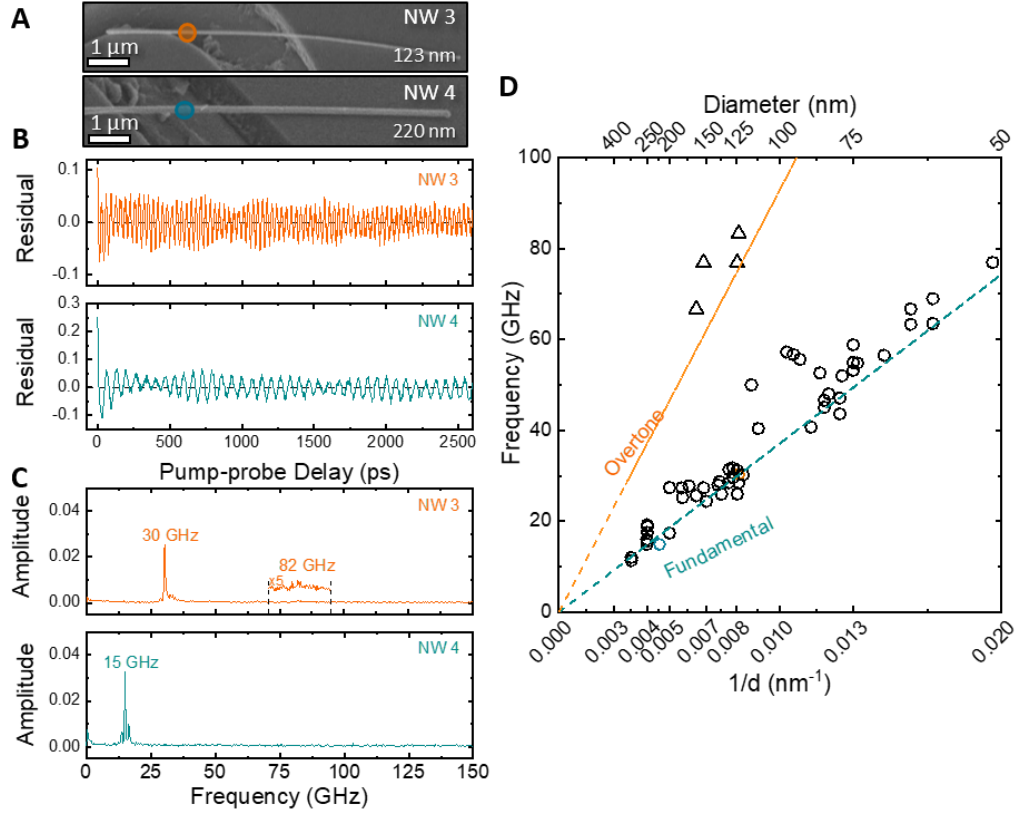
Figure 3.5. **Diameter dependence of acoustics phonon modes.** (**A**) SEM images of NW3 and NW4 suspended over trenches with the positions highlighted by teal and orange circles where transient scans were collected. (**B**) Coherence patterns (residuals from fitting the transient signals) corresponding to NW3 (orange) and NW4 (teal). (**C**) FFT of coherence patterns for NW3 and NW4. The fundamental RBMs at 30 GHz (for NW3, d = 123 nm) and 15 GHz (for NW4, d = 220 nm) and the first overtone mode at 82 GHz in NW3. (**D**) The frequency of the observed vibrational modes versus 1/d. The symbols represent experimental data, dashed lines represent calculations for fundamental (teal) and first overtone breathing modes (orange) ($\xi_0 = 2.162$ and $\xi_1 = 5.412$), performed using the bulk elastic constants of germanium.[51, 52]

Pump-probe measurements performed on multiple NWs show that the coherence frequency increases with decreasing diameter, much in the same way that the pitch of a bell changes with size. This variation with diameter is exemplified by the data from the two NWs depicted in Figure 3.5A. There is a clear increase in the coherence period for the larger of the two nanowires (Figure 3.5B), and Fourier analysis reveals that the RBM frequency decreases by a factor of two as the diameter increases from 123 nm to 220 nm (Figure 3.5C). Pump-probe measurements performed on an ensemble of NWs provide a quantitative relationship between vibrational frequency and NW size. RBM frequencies obtained from 40 different locations on 24 different NWs with diameters ranging from 50 to 300 nm (as measured by SEM) show that the coherence frequency scales linearly with 1/d (Figure 3.5D).[21, 53]

The inverse proportionality with diameter is consistent with elastomeric models of the NW. The RBM frequency (ω_{br}) predicted for an isotropic elastic cylinder is given by

$$\omega_{br}^{(n)} = \frac{\xi_n}{\pi d} C_L, \qquad [3.6]$$

where d is the NW diameter and C_L is the longitudinal speed of sound. The mode frequency also scales with ξ_n, which is the nth eigenvalue obtained from

$$\xi_n J_0(\xi_n) = \frac{1 - 2\nu}{1 - \nu} J_1(\xi_n), \qquad [3.7]$$

where ν is the Poisson ratio and $J_0(\xi)$ and $J_1(\xi)$ are Bessel functions. For Ge, $\nu = 0.28$,[52] which yields $\xi_0 = 2.16$ and $\xi_1 = 5.41$ for the fundamental and first overtone, respectively. The frequencies for the fundamental and first overtone obtained from Eqn. 3.6 with $C_L = 5400$ m/s (speed of sound in bulk Ge)[54] are depicted as a function of NW diameter by the dashed lines in Figure 3.5C. The fundamental frequency ($n = 0$) closely matches the most prominent

frequency component observed in the phonon spectrum. Some structures (*e.g.* NW5) also show a weak higher frequency peak that corresponds to the first overtone (n = 1) of the RBM.

While this model reproduces the general phonon structure, closer examination of the SOPP transients shows a clear beat pattern in the coherence component. Similar beating is observed in transient signals of metal nanowires,[26, 27, 55] where the non-circular cross-section gives rise to multiple RBMs with similar frequencies that interfere with each other.[26, 56] The modulated amplitude of the coherence in the Ge NWs transients could arise from a similar beating between two closely spaced modes and may reflect that the NW cross section is not perfectly circular.
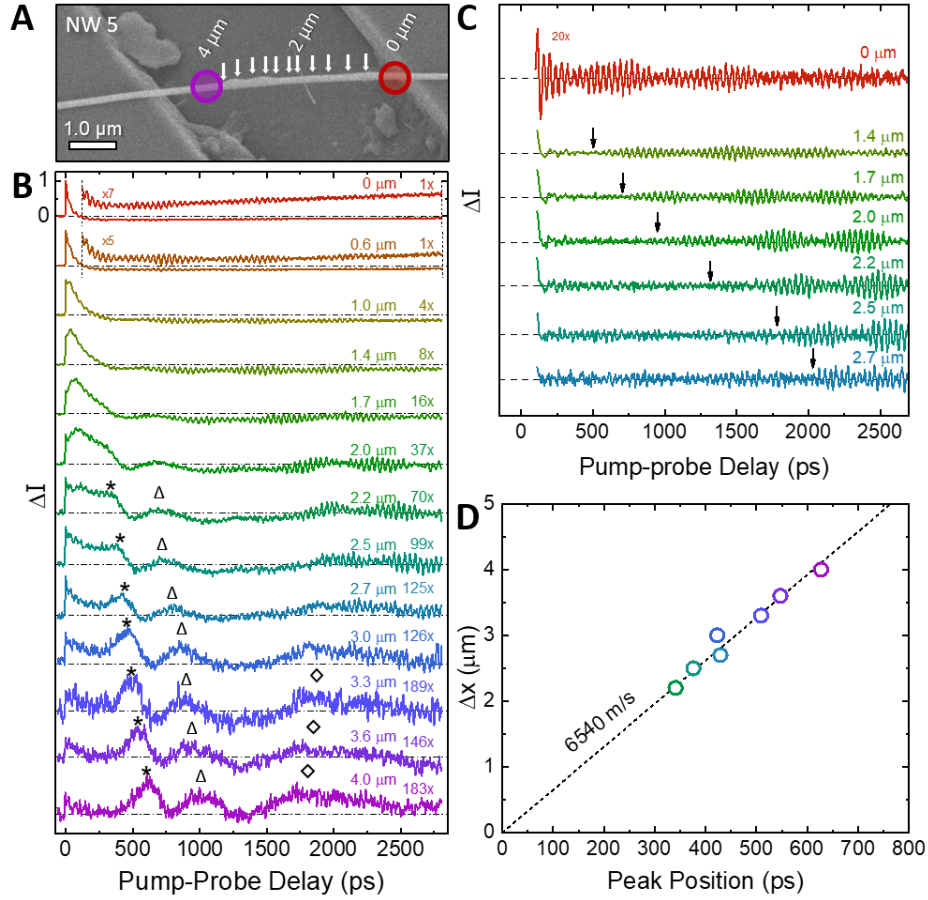
Figure 3.6. SSPP transients of charge-carrier recombination and coherent phonon propagation. (A) SEM image showing suspended section of NW5. The location of the pump excitation is indicated by red circle. The probe position is displaced from the pump along the NW axis up to 4μm separation (purple circle) in steps of ~200-400 nm as denoted by the arrows. **(B)** SSPP transients obtained with the pump-probe separations Δx between 0 μm and 4 μm. Each transient is normalized to its maximum signal with scaling factors relative to Δx = 0 μm shown to the right. The asterisk, triangle, and diamond symbols mark three recurrences in the transient signal that result from excitation of a low-frequency mode propagating out from the point of excitation. **(C)** Pump-probe transients after application of a high-pass Fourier filter show delayed onset of high-frequency coherence at larger separations, as indicated by arrows above each trace. **(D)** The spatial position of the fundamental phonon peak (marked by asterisks in panel B) versus pump-probe delay. The slope of the linear fit line (black) is the propagation speed of the low-frequency mode.

Spreading of the phonon excitation along the NW is observed by collecting transients

with spatially separated pump and probe beams (Figure 3.6). The experimental geometry is

depicted in Figure 3.6A, which shows NW5 suspended across a 5 µm wide trench. The pump beam is directed onto the NW near one edge of the trench (red circle), impulsively exciting a localized region of the NW. The probe beam (purple circle) is then positioned at a distance (Δx) away, towards the opposite side of the trench. Figure 3.6B shows a series of 13 transients obtained at increasing separations (Δx) ranging from 0 µm to 4 µm, with the different probe locations marked by the arrows in Figure 3.6A. The transient obtained when the pump and probe are spatially coincident ($\Delta x = 0$) exhibits the same dynamical features as the transient observed for NW1 (Figure 3.1) and NW2 (Figure 3.3). The shape of the transients changes dramatically as the probe pulse is moved progressively further away from the pump. There is an overall decrease in the pump-probe signal, the magnitude of which is indicated by the scaling factors shown at the right for each transient. The transients obtained with Δx between 1.0 µm and 1.7 µm show a delayed rise in the signal, reflecting the time needed for charge carriers to reach the location of the probe beam. Given the spot sizes of the pump and probe beams (400 nm and 600 nm, respectively), there is some residual overlap of the two laser pulses for separations up to about 1.0 µm, which is likely the reason for the observation of signal at $\Delta t = 0$ ps. For larger separations, their spatial overlap is expected to be negligible, yet we still observe pump-probe signal at $\Delta t = 0$ ps, even at separations as large as 4 µm. We do not observe this type of prompt signal in experiments where the NW is in direct contact with the substrate, suggesting that its origin involves the trench geometry of the experiment. One possibility is that it results from scattering of the pump beam by the trench as it passes through the sample, causing a weak excitation of the NW even at the remote locations.

Like the free carrier and thermal signals, the coherence associated with the RBM also appear to exhibit a delayed onset, as marked by arrows in Figure 3.6C, when the pump and probe spots are well-separated. The RBM coherence in the SSPP transients is isolated through application of high-pass Fourier filter, which removes frequency components below 10 GHz (Figure 3.6C). This delayed onset (marked by the arrows in the figure) is apparent when the separation exceeds 1.0 µm, although it is most prevalent in the $\Delta x = 2.0$-2.5µm transients where the coherent oscillations do not appear until ~1000 ps (or later), and then increase in amplitude over time. As the separation is further increased, it takes more time for the signature of the RBM to appear, and by 2.7 µm the onset of the coherent oscillation has shifted beyond the 2.8 ns time window of the experiment. The systematic delay in the coherence onset at larger separations indicates that the RBM motion is not confined to the point of excitation, but rather slowly spreads along NW axis as the expansion and contraction of the NW in one location induces vibrational motion in adjacent sections that are initially vibrationally quiet.

The series of transients also show a broad temporal feature (marked by an asterisk) that is first noticeable as a shoulder in the 2.2 µm transient at ~350 ps. This feature is followed by a second recurrence of weaker intensity (marked by the triangle) appearing at ~750 ps. The arrival time of these two features increases linearly with pump-probe separation (Figure 3.6D), indicating the transient distortion is moving with a constant velocity away from the point of excitation. We attribute these two features to the formation of a shock wave that propagates along the NW at ~6540 m/s, or about 20% faster than the speed of sound in bulk germanium (5400 m/s).[57] The period of this recurrence is determined by the size of the diffraction-limited excitation pulse on the sample, creating a standing wave

across the NW from the superposition of the different wavelengths that form the laser pulses.[41]

These two features are followed by a third recurrence in the signal (marked by diamond) that is significantly broader than the other features. This third recurrence is most well-defined at the largest separation (4 µm), arriving at 2-3 ns after excitation. However, whereas the arrival of the first two features is increasingly delayed as the probe is moved away from the pump, the third appears to arrive earlier, and become more intense at the furthest separation. These observations suggest that the third recurrence results when the shock-wave reaches the far side of the trench and reflects off the point where the NW makes contact with the substrate. The reflection then travels back along the NW towards the location probe pulse, taking longer to reach the probe spot when it is located closer to the pump (*i.e.* smaller Δx).

3.4. Conclusions

In summary, the pump pulse photoexcites electrons-hole pairs within a localized section of the Ge NW. Rapid electron-hole recombination results in an impulsive excitation of a radial breathing mode and shockwave observed as coherence in the transient dynamics. When the NW is in contact with the substrate, the coherences dampen out quickly. Suspending the NWs over trenches reduces the mechanical coupling between the NW and substrate, allowing the coherence to live much longer and observing the spreading of the vibrational motion outside of the initial excitation spot. The RBM slowly spreads outside of the initial excitation spot at ~1 nm/ps, while the shockwave propagates along the NW axis at ~6500 m/s. The shockwave travels across the NW until it reaches the opposite side of the

trench, at which point it reflects off the point of contact where NW meets the substrate and moves back toward the pump spot. Time-resolved images show clear evidence of rapid diffusion and recombination of the free carriers followed by thermal transport on slower time scales. Charge-carrier diffusion is similar to that observed in bulk Ge, the thermal diffusion is ~2x slower than the bulk, consistent with trends previously observed in our studies of Si NWs.

Acknowledgments

Supporting Information

Trenches were fabricated on quartz substrates using a combination of photolithography and deep reactive ion etching (DRIE). A custom photomask (by PhotomaskPortal) was created that included a registry pattern and grid of trenches. Quartz slide was coated with MICROPOSIT S1805 photoresist (MicroChem) with a spin coater at 3000 rpm and heated to 115°C for 60 sec on a hotplate. The trench registry pattern was

transferred into the polymer coated slides using the photomask and mask aligner (Karl Suss MA6/BA6) and developed with MICROPOSIT MF-319 developer (MicroChem) and heated on a hotplate at 115°C for 60 seconds. The pattern was then etched into the quartz itself using DRIE (Alcatel AMS 100). Trenches were ~1 μm deep, measured with a Stylus Profiler (KLA Tencor P-6).

Pump-probe experiments were performed on a home-built microscope[9] An output beam (850 nm) from a mode-locked Ti: Sapphire laser (Spectra-Physics, 80 MHz, 100 fs) is split by a 90:10 beam splitter. Two synchronized AOMs (Gooch and Housego) reduce the repetition rates of both beams to 4 MHz. A 1 mm β-barium borate (BBO) crystal is used to frequency double the beam and generates the high-power pump pulse (425 nm). The low powered beam is used as the probe. The probe is directed through a mechanical delay stage twice, which can adjust the delay from −500 ps to 2.8 ns. The probe passes through a computer-controlled scanning mirror assembly that controls the angle of incidence of the beam on the back of the objective. Neutral density filters attenuate the pump and probe pulse energies and the two beams are recombined at a dichroic beam splitter and focused by a microscope objective (100x, NA 0.8) to spot sizes that are 400 nm and 600 nm for the pump and the probe, respectively. The transmitted light is collected by a condenser lens and detected by a balanced photodiode. A lock-in amplifier detects pump-induced changes in probe intensity. A mechanical delay stage was used to collect SSPP images within the 0−2123 ps range, while longer time delays (12.5-37.5 ns) were achieved by selecting subsequent pulses from the 80 MHz pulse train with synchronized acousto-optic modulators. By utilizing two AOMs, one for each the pump and probe beams, we can pick individual pulses and reduce the repetition rate of the laser. By selecting non-coincident pump-probe

pulse pairs, we can increase the pump-probe delay in steps of 12.5 ns (corresponding to an 80 MHz laser repetition rate).

REFERENCES

1. Grumstrup, E. M.; Cating, E. M.; Gabriel, M. M.; Pinion, C. W.; Christesen, J. D.; Kirschbrown, J. R.; Vallorz, E. L.; Cahoon, J. F.; Papanikolas, J. M., Ultrafast Carrier Dynamics of Silicon Nanowire Ensembles: The Impact of Geometrical Heterogeneity on Charge Carrier Lifetime. *J. Phys. Chem. C* **2014,** *118* (16), 8626-8633.

2. Cating, E. E. M.; Pinion, C. W.; Christesen, J. D.; Christie, C. A.; Grumstrup, E. M.; Cahoon, J. F.; Papanikolas, J. M., Probing Intrawire, Interwire, and Diameter-Dependent Variations in Silicon Nanowire Surface Trap Density with Pump-Probe Microscopy. *Nano Lett.* **2017,** *17* (10), 5956-5961.

3. Grumstrup, E. M.; Gabriel, M. M.; Cating, E. M.; Pinion, C. W.; Christesen, J. D.; Kirschbrown, J. R.; Vallorz, E. L.; Cahoon, J. F.; Papanikolas, J. M., Ultrafast Carrier Dynamics in Individual Silicon Nanowires: Characterization of Diameter-Dependent Carrier Lifetime and Surface Recombination with Pump–Probe Microscopy. *J. Phys. Chem. C* **2014,** *118* (16), 8634-8640.

4. Li, Y.; Clady, R.; Park, J.; Thombare, S. V.; Schmidt, T. W.; Brongersma, M. L.; McIntyre, P. C., Ultrafast Electron and Phonon Response of Oriented and Diameter-Controlled Germanium Nanowire Arrays. *Nano Lett.* **2014,** *14* (6), 3427-31.

5. Prasankumar, R. P.; Choi, S.; Trugman, S. A.; Picraux, S. T.; Taylor, A. J., Ultrafast Electron and Hole Dynamics in Germanium Nanowires. *Nano Lett.* **2008,** *8* (6), 1619-1624.

6. Cavalleri, A.; Schoenlein, R. W., Femtosecond X-Rays and Structural Dynamics in Condensed Matter. In *Ultrafast Dynamical Processes in Semiconductors*, Tsen, K.-T., Ed. Springer Berlin Heidelberg: Berlin, Heidelberg, 2004; pp 309-338.

7. Li, Y.; Clady, R.; Marshall, A. F.; Park, J.; Thombare, S. V.; Chan, G.; Schmidt, T. W.; Brongersma, M. L.; McIntyre, P. C., Ultrafast Carrier Dynamics of a Photo-Excited Germanium Nanowire–Air Metamaterial. *ACS Photonics* **2015,** *2* (8), 1091-1098.

8. House, R. L.; Mehl, B. P.; Kirschbrown, J. R.; Barnes, S. C.; Papanikolas, J. M., Characterizing the Ultrafast Charge Carrier Trapping Dynamics in Single ZnO Rods Using Two-Photon Emission Microscopy. *J. Phys. Chem. C* **2011,** *115* (21), 10806-10816.

9.   Mehl, B. P.; Kirschbrown, J. R.; Gabriel, M. M.; House, R. L.; Papanikolas, J. M., Pump-Probe Microscopy: Spatially Resolved Carrier Dynamics in ZnO Rods and the Influence of Optical Cavity Resonator Modes. *J. Phys. Chem. B* **2013,** *117* (16), 4390-8.

10.   Grumstrup, E. M.; Gabriel, M. M.; Pinion, C. W.; Parker, J. K.; Cahoon, J. F.; Papanikolas, J. M., Reversible Strain-Induced Electron-Hole Recombination in Silicon Nanowires Observed with Femtosecond Pump-Probe Microscopy. *Nano Lett.* **2014,** *14* (11), 6287-92.

11.   Gabriel, M. M.; Kirschbrown, J. R.; Christesen, J. D.; Pinion, C. W.; Zigler, D. F.; Grumstrup, E. M.; Mehl, B. P.; Cating, E. E.; Cahoon, J. F.; Papanikolas, J. M., Direct Imaging of Free Carrier and Trap Carrier Motion in Silicon Nanowires by Spatially-Separated Femtosecond Pump-Probe Microscopy. *Nano Lett.* **2013,** *13* (3), 1336-40.

12.   Cating, E. E.; Pinion, C. W.; Van Goethem, E. M.; Gabriel, M. M.; Cahoon, J. F.; Papanikolas, J. M., Imaging Spatial Variations in the Dissipation and Transport of Thermal Energy within Individual Silicon Nanowires Using Ultrafast Microscopy. *Nano Lett.* **2016,** *16* (1), 434-9.

13.   Gabriel, M. M.; Grumstrup, E. M.; Kirschbrown, J. R.; Pinion, C. W.; Christesen, J. D.; Zigler, D. F.; Cating, E. E.; Cahoon, J. F.; Papanikolas, J. M., Imaging Charge Separation and Carrier Recombination in Nanowire p-i-n Junctions Using Ultrafast Microscopy. *Nano Lett.* **2014,** *14* (6), 3079-87.

14.   Zijlstra, P.; Tchebotareva, A. L.; Chon, J. W. M.; Gu, M.; Orrit, M., Acoustic Oscillations and Elastic Moduli of Single Gold Nanorods. *Nano Lett.* **2008,** *8* (10), 3493-3497.

15.   Staleva, H.; Skrabalak, S. E.; Carey, C. R.; Kosel, T.; Xia, Y.; Hartland, G. V., Coupling to Light, and Transport and Dissipation of Energy in Silver Nanowires. *PCCP* **2009,** *11* (28), 5889-5896.

16.   Polli, D.; Lisiecki, I.; Portalès, H.; Cerullo, G.; Pileni, M.-P., Low Sensitivity of Acoustic Breathing Mode Frequency in Co Nanocrystals Upon Change in Nanocrystallinity. *ACS Nano* **2011,** *5* (7), 5785-5791.

17.   Juve, V.; Crut, A.; Maioli, P.; Pellarin, M.; Broyer, M.; Del Fatti, N.; Vallee, F., Probing Elasticity at the Nanoscale: Terahertz Acoustic Vibration of Small Metal Nanoparticles. *Nano Lett.* **2010,** *10* (5), 1853-8.

18.   Owrutsky, J. C.; Pomfret, M. B.; Brown, D. J., Coherent Acoustic Oscillations of Nanorods Composed of Various Metals. *J. Phys. Chem. C* **2009,** *113* (25), 10947-10955.

19.   Yu, K.; Zijlstra, P.; Sader, J. E.; Xu, Q. H.; Orrit, M., Damping of Acoustic Vibrations of Immobilized Single Gold Nanorods in Different Environments. *Nano Lett.* **2013,** *13* (6), 2710-6.

20.   Jean, C.; Belliard, L.; Cornelius, T. W.; Thomas, O.; Pennec, Y.; Cassinelli, M.; Toimil-Molares, M. E.; Perrin, B., Spatiotemporal Imaging of the Acoustic Field Emitted by a Single Copper Nanowire. *Nano Lett.* **2016,** *16* (10), 6592-6598.

21.   Jean, C.; Belliard, L.; Cornelius, T. W.; Thomas, O.; Toimil-Molares, M. E.; Cassinelli, M.; Becerra, L.; Perrin, B., Direct Observation of Gigahertz Coherent Guided Acoustic Phonons in Free-Standing Single Copper Nanowires. *J. Phys. Chem. Lett.* **2014,** *5* (23), 4100-4.

22.   Petrova, H.; Perez Juste, J.; Pastoriza-Santos, I.; Hartland, G. V.; Liz-Marzan, L. M.; Mulvaney, P., On the Temperature Stability of Gold Nanorods: Comparison between Thermal and Ultrafast Laser-Induced Heating. *PCCP* **2006,** *8* (7), 814-21.

23.   Hu, M.; Hillyard, P.; Hartland, G. V.; Kosel, T.; Perez-Juste, J.; Mulvaney, P., Determination of the Elastic Constants of Gold Nanorods Produced by Seed Mediated Growth. *Nano Lett.* **2004,** *4* (12), 2493-2497.

24.   Hartland, G. V., Optical Studies of Dynamics in Noble Metal Nanostructures. *Chem. Rev.* **2011,** *111* (6), 3858-87.

25.   Hodak, J. H.; Henglein, A.; Hartland, G. V., Photophysics of Nanometer Sized Metal Particles: Electron−Phonon Coupling and Coherent Excitation of Breathing Vibrational Modes. *J. Phys. Chem. B* **2000,** *104* (43), 9954-9965.

71

26. Yu, K.; Major, T. A.; Chakraborty, D.; Devadas, M. S.; Sader, J. E.; Hartland, G. V., Compressible Viscoelastic Liquid Effects Generated by the Breathing Modes of Isolated Metal Nanowires. *Nano Lett.* **2015,** *15* (6), 3964-70.

27. Major, T. A.; Lo, S. S.; Yu, K.; Hartland, G. V., Time-Resolved Studies of the Acoustic Vibrational Modes of Metal and Semiconductor Nano-Objects. *J. Phys. Chem. Lett.* **2014,** *5* (5), 866-74.

28. Lo, S. S.; Major, T. A.; Petchsang, N.; Huang, L.; Kuno, M. K.; Hartland, G. V., Charge Carrier Trapping and Acoustic Phonon Modes in Single CdTe Nanowires. *ACS Nano* **2012,** *6* (6), 5274-5282.

29. Sakuma, H.; Tomoda, M.; Otsuka, P. H.; Matsuda, O.; Wright, O. B.; Fukui, T.; Tomioka, K.; Veres, I. A., Vibrational Modes of GaAs Hexagonal Nanopillar Arrays Studied with Ultrashort Optical Pulses. *Appl. Phys. Lett.* **2012,** *100* (13), 131902.

30. Hu, M.; Wang, X.; Hartland, G. V.; Mulvaney, P.; Juste, J. P.; Sader, J. E., Vibrational Response of Nanorods to Ultrafast Laser Induced Heating: Theoretical and Experimental Analysis. *J. Am. Chem. Soc.* **2003,** *125* (48), 14925-33.

31. Dong, S.; Lian, J.; Jhon, M. H.; Chan, Y.; Loh, Z. H., Pump-Power Dependence of Coherent Acoustic Phonon Frequencies in Colloidal CdSe/CdS Core/Shell Nanoplatelets. *Nano Lett.* **2017,** *17* (5), 3312-3319.

32. Prasankumar, R. P.; Upadhya, P. C.; Taylor, A. J., Ultrafast Carrier Dynamics in Semiconductor Nanowires. *Phys. Status Solidi B* **2009,** *246* (9), 1973-1995.

33. Jellison, G. E., Optical Functions of GaAs, GaP, and Ge Determined by Two-Channel Polarization Modulation Ellipsometry. *Opt. Mater.* **1992,** *1* (3), 151-160.

34. Elci, A.; Scully, M. O.; Smirl, A. L.; Matter, J. C., Ultrafast Transient Response of Solid-State Plasmas. I. Germanium, Theory, and Experiment. *Phys. Rev. B* **1977,** *16* (1), 191-221.

35. Latham, W. P.; Smirl, A. L.; Elci, A.; Bessey, J. S., The Role of Phonons and Plasmons in Describing the Pulsewidth Dependence of the Transmission of Ultrashort Optical Pulses through Germanium. *Solid-State Electronics* **1978,** *21* (1), 159-165.

36.   Crut, A.; Maioli, P.; Del Fatti, N.; Vallee, F., Acoustic Vibrations of Metal Nano-Objects: Time-Domain Investigations. *Phys. Rep.* **2015,** *549*, 1-43.

37.   Yan, Y. X.; Gamble, E. B.; Nelson, K. A., Impulsive Stimulated Scattering: General Importance in Femtosecond Laser Pulse Interactions with Matter, and Spectroscopic Applications. *J. Chem. Phys.* **1985,** *83* (11), 5391-5399.

38.   Wright, O. B.; Perrin, B.; Matsuda, O.; Gusev, V. E., Ultrafast Carrier Diffusion in Gallium Arsenide Probed with Picosecond Acoustic Pulses. *Phys. Rev. B* **2001,** *64* (8).

39.   Sokolowski-Tinten, K.; Shymanovich, U.; Nicoul, M.; Blums, J.; Tarasevitch, A.; Horn-von-Hoegen, M.; von der Linde, D.; Morak, A.; Wietler, T. In *Energy Relaxation and Anomalies in the Thermo-Acoustic Response of Femtosecond Laser-Excited Germanium*, Berlin, Heidelberg, Springer Berlin Heidelberg: Berlin, Heidelberg, 2007; pp 597-599.

40.   Thomsen, C.; Grahn, H. T.; Maris, H. J.; Tauc, J., Surface Generation and Detection of Phonons by Picosecond Light Pulses. *Phys. Rev. B* **1986,** *34* (6), 4129-4138.

41.   Nelson, K. A.; Fayer, M. D., Laser Induced Phonons: A Probe of Intermolecular Interactions in Molecular Solids. *J. Chem. Phys.* **1980,** *72* (9), 5202-5218.

42.   Ouyang, G.; Zhu, W. G.; Sun, C. Q.; Zhu, Z. M.; Liao, S. Z., Atomistic Origin of Lattice Strain on Stiffness of Nanoparticles. *PCCP* **2010,** *12* (7), 1543-9.

43.   Ruello, P.; Gusev, V. E., Physical Mechanisms of Coherent Acoustic Phonons Generation by Ultrafast Laser Action. *Ultrasonics* **2015,** *56*, 21-35.

44.   Zollner, S.; Myers, K. D.; Jensen, K. G.; Dolan, J. M.; Bailey, D. W.; Stanton, C. J., Femtosecond Interband Hole Scattering in Ge Studied by Pump-Probe Reflectivity. *Solid State Commun.* **1997,** *104* (1), 51-55.

45.   Smith, R. C., High-Temperature Specific Heat of Germanium. *J. Appl. Phys.* **1966,** *37* (13), 4860-4865.

46. Hsiao, T. K.; Huang, B. W.; Chang, H. K.; Liou, S. C.; Chu, M. W.; Lee, S. C.; Chang, C. W., Micron-Scale Ballistic Thermal Conduction and Suppressed Thermal Conductivity in Heterogeneously Interfaced Nanowires. *Phys. Rev. B* **2015,** *91* (3).

47. Maycock, P. D., Thermal Conductivity of Silicon, Germanium, III-V Compounds and III–V Alloys. *Solid-State Electronics* **1967,** *10* (3), 161-168.

48. McCarthy, K. A.; Ballard, S. S., Thermal Conductivity of Germanium at Ambient Temperatures. *Phys. Rev.* **1955,** *99* (4), 1104-1104.

49. Young, J. F.; van Driel, H. M., Ambipolar Diffusion of High-Density Electrons and Holes in Ge, Si, and GaAs: Many-Body Effects. *Phys. Rev. B* **1982,** *26* (4), 2147-2158.

50. Auston, D. H.; Shank, C. V., Picosecond Ellipsometry of Transient Electron-Hole Plasmas in Germanium. *Phys. Rev. Lett.* **1974,** *32* (20), 1120-1123.

51. Othonos, A.; van Driel, H. M.; Young, J. F.; Kelly, P. J., Correlation of Hot-Phonon and Hot-Carrier Kinetics in Ge on a Picosecond Time Scale. *Phys. Rev. B* **1991,** *43* (8), 6682-6690.

52. Greaves, G. N.; Greer, A. L.; Lakes, R. S.; Rouxel, T., Poisson's Ratio and Modern Materials. *Nat. Mater.* **2011,** *10* (11), 823-37.

53. Jerebtsov, S. N.; Kolomenskii, A. A.; Liu, H.; Zhang, H.; Ye, Z.; Luo, Z.; Wu, W.; Paulus, G. G.; Schuessler, H. A., Laser-Excited Acoustic Oscillations in Silver and Bismuth Nanowires. *Phys. Rev. B* **2007,** *76* (18).

54. Wolff, C.; Soref, R.; Poulton, C. G.; Eggleton, B. J., Germanium as a Material for Stimulated Brillouin Scattering in the Mid-Infrared. *Opt. Express* **2014,** *22* (25), 30735-47.

55. Belliard, L.; Cornelius, T. W.; Perrin, B.; Kacemi, N.; Becerra, L.; Thomas, O.; Eugenia Toimil-Molares, M.; Cassinelli, M., Vibrational Response of Free Standing Single Copper Nanowire through Transient Reflectivity Microscopy. *J. Appl. Phys.* **2013,** *114* (19), 193509.

56.   Major, T. A.; Crut, A.; Gao, B.; Lo, S. S.; Del Fatti, N.; Vallee, F.; Hartland, G. V., Damping of the Acoustic Vibrations of a Suspended Gold Nanowire in Air and Water Environments. *PCCP* **2013,** *15* (12), 4169-76.

57.   Hao, H.; Maris, H. J., Study of Phonon Dispersion in Silicon and Germanium at Long Wavelengths Using Picosecond Ultrasonics. *Phys. Rev. Lett.* **2000,** *84* (24), 5556-9.

CHAPTER 4: IMAGING EXCITED STATE DYNAMICS IN 2D TRANSITION METAL
DICHALCOGENIDE NANOFLAKES

4.1. Introduction

Pump-probe experiments performed on two-dimensional transition metal
dichalcogenide nanomaterials (TMDCs) often reflect a variety of dynamical phenomena,
including exciton-exciton annihilation, exciton dissociation, exciton recombination, electron-
hole recombination, and carrier trapping as well as coherent processes arising from impulsive
excitation of lattice phonons.[1-3] Heterogeneity within samples of nanostructures (such as
variation in morphology, defect concentration, and strain) strongly affect the electronic
structure and drastically alter the measured experimental response in ensemble
measurements.[4-8] Surface defects dramatically degrade the electronic and optical properties
of semiconductors when the size of the materials are reduced to the nanoscale.[9-11] However,
TMDCs have a significantly lower density of defects at the basal surface (top and bottom
surfaces of a layer that are perpendicular to the principal axis) because the layers are held
together by Van der Waals forces.[10, 12] The edges of the nanoflakes (NFs) have dangling
bonds that are spots for defects[11], which provide sites for catalytic activity[13-17] or limit device
performance.[18, 19] In this regard, ultrafast spatially-resolved techniques capable of probing
individual structures, and even localized regions along a single structure, are preferred.

Similarly, ultrafast optical spectroscopies have been used to probe photoinduced
changes in the optical properties of few-layer and bulk molybdenum disulfide (MoS_2),
molybdenum diselenide ($MoSe_2$), tungsten disulfide (WS_2), and tungsten diselenide

(WSe$_2$).[20] The alteration in optical properties can then be correlated with electronic and structural changes in the TMDC materials. TMDC nanomaterial ensembles contain a variety of structural features (*i.e.* edges, steps, buckles, etc.) that lead to varying transient signals. The large excitation spot size used in these spectroscopy techniques average the signals from many structures, resulting in multiexponential decay components. This convolutes the assignment of different kinetic pathways to the observed excited state decay.[21] High spatial resolution pump-probe microscopy circumvents this problem by interrogating dynamics in localized regions on single WS$_2$ and WSe$_2$ nanostructures to disentangle the intrinsic kinetic pathways arising from an assortment of structural features.

Here we report on the application of pump-probe microscopy methods to the study of WS$_2$ and WSe$_2$ NFs. The transients obtained from WS$_2$ NFs includes kinetic contributions from exciton-exciton annihilation (second-order, $\tau < 200$ ps), electron-hole recombination (first-order, $\tau > 3000$ ps), and coherence from impulsive excitation of acoustic phonon modes.   However, transients collected on WSe$_2$ NFs include kinetic contributions from indirectly excited excitons that either dissociate into unbound electron-hole pairs or directly recombine. Excitons in WS$_2$ relax quicker at the edges of NFs, compared to the interior where there are fewer defect sites from dangling bonds. However, WSe$_2$ shows similar exciton lifetimes spatially across the NF but the interior shows faster free carrier recombination instead of the edges. We observe a periodic modulation in the pump-probe signal across both WS$_2$ and WSe$_2$ NFs in the SOPP images due to the propagation of exciton-polaritons.

4.2. Experimental

4.2.1. Sample Preparation

Tungsten disulfide and tungsten diselenide nanoflake samples were each prepared via mechanical exfoliation of bulk crystals (2D Semiconductor, Inc.) via the scotch tape method shown in Figure 4.1.
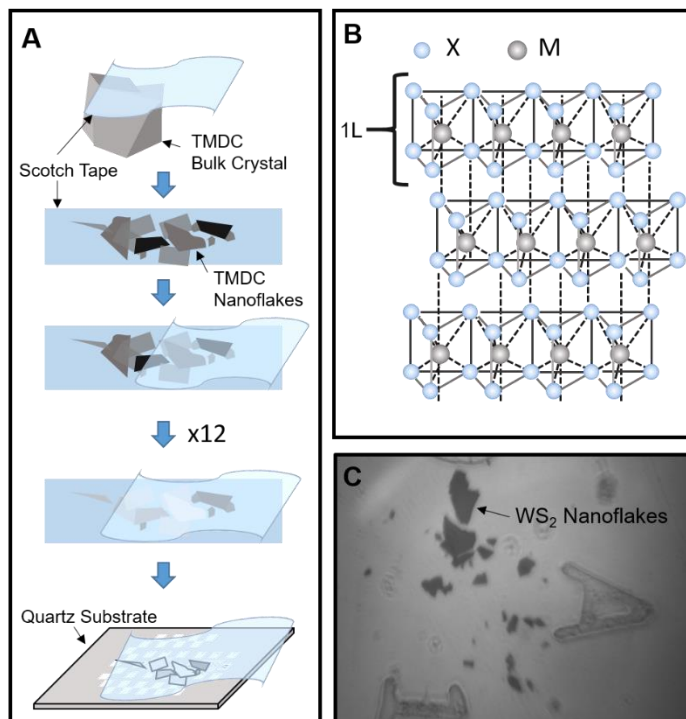
Figure 4.1: Mechanical exfoliation of bulk TMDC crystals (A) Illustration of scotch tape method for mechanically exfoliating bulk WS_2 (or WSe_2) crystals to generate nanoflakes. Scotch tape is applied to a small piece of bulk crystal and removed. Top layers of the bulk crystal adhere to the tape from which more tape is applied, further thinning the TMDC flake layers. After multiple applications of scotch tape, the tape is applied to the surface of an etched quartz slide to transfer thin nanoflakes onto the substrate. **(B)** Crystal structure of TMDCs. Metal atoms (M) are sandwiched between two layers of chalcogen atoms (X) called a monolayer (1L), where monolayers are held together by Van Der Waal forces. **(C)** Bright field image of WS_2 NFs on an etched quartz substrate.

Figure 4.1 illustrates how Scotch tape is used to mechanically exfoliate TMDC bulk crystals to atomically thin nanoflakes. The bulk crystal is composed of monolayers (Figure

4.1B) that are held together by Van der Waals forces, which can be easily separated via mechanical exfoliation. A piece of scotch tape is applied to a bulk crystal of WS_2 and then removed (Figure 4.1A), leaving behind WS_2 layers stuck to the tape. Placing a new piece of scotch tape onto the newly exfoliated sample and removing the top tape layer further exfoliates the sample down to nanoscale thickness. After 12 exfoliations, a small piece of tape with NFs is pressed to an etched quartz substrate slide, transferring the NFs to the substrate surface. The slide is then placed in an acetone bath for 20 minutes to remove the scotch tape residue from the substrate. A bright field microscope is used to locate individual NFs on the quartz substrate. An example of the resulting TMDC NFs is shown in Figure 4.2C, where WS_2 NFs are located at position A10 the registry side of the quartz substrate.

4.2.2. Ultrafast Microscope

  Pump-probe experiments are performed with a home-built microscope based on a mode-locked Ti: Sapphire laser.[22] The 850 nm laser output is split by a 90:10 beam splitter. The two beams pass through synchronized acousto-optic modulators (AOMs), reducing their repetition rates to 1.6 MHz. The more intense fraction is directed through a β-barium borate (BBO) crystal to generate the 425 nm pump pulse while the lower-intensity component is used as the 850 nm probe. The probe is quadruple-passed through a 253 mm mechanical stage, providing about 3.3 ns of optical delay. The probe then passes through a set of computer-controlled scanning mirrors that change the angle of the beam as it enters the objective, allowing the probe to be focused to a spatially distinct point on the sample. The two beams are then attenuated using neutral density filters. They are then recombined using a dichroic mirror and directed onto the back aperture of a microscope objective (100x, 0.8

NA), which focuses the pump and probe beams to 400 nm and 600 nm diffraction-limited spots at the sample. Individual nanostructures are placed within the laser focus using a 2-axis piezo scanning stage. The transmitted probe light (T) is collected by a high NA condenser lens and detected by a balanced photodiode. The reflected probe light (R) is collected with the microscope objective and detected by a second balance photodiode. The pump beam is modulated at 16 kHz and the pump-induced changes in the probe intensity (ΔT or ΔR) are detected by lock-in amplification. With this microscope, we can measure the transient responses of a single nanostructure with ~600 nm spatial resolution and ~500 fs time resolution, with a sensitivity of $\Delta T/T \sim 10^{-5}$.[22]

4.3. Results and Discussion

4.3.1. Band Structure Characterization

The TMDC NFs in this study were prepared via mechanical exfoliation of natural crystals and transferred onto a patterned quartz substrate (shown previously in Figure 4.1). The thickness of a typical WS_2 and WSe_2 NFs were measured with atomic force microscopy (AFM) (Figure 4.2A), where the average height of the flakes are ~40 nm (~64 layers).[23] Bulk WS_2 and WSe_2 are indirect bandgap materials (~1.4 eV and 1.2 eV, respectively),[24] composed of a valence band (VB) maximum at the Γ point and a conduction band (CB) minimum between the K-Γ points of the Brillouin zone. The bulk-like electronic structures (Figure 4.2b and 4.2d) of these flakes was confirmed by collecting a transmission profile (Figure 4.2e) using a microspectrophotometer (MSP) (Craic 20/30 PV).

Excitation by the pump pulse (425 nm) excites electron-hole pairs above the bandgap which then rapidly relax to the band edge.[2] A fraction of these electron-hole pairs are stabilized through Coulombic attractions which act as a single quasiparticle called an exciton.[25] The A and B exciton peaks, involving the direct band-to-band transitions at K (indicated by the orange and green arrows in Figure 4.2B and 4.2D), are observed at 630 nm and 515 nm, with the C exciton appearing at 455 nm in WS_2. Whereas the A and B exciton peaks are located at 764 nm and 600 nm, respectively in WSe_2. The VB splits into two bands at the K point, with the A and B excitons located at the transition from the higher and lower VB to the CB, respectively.[26] The C exciton in WS_2 is speculated be a direct transition located at the Γ in the Brillouin zone, but has not yet been verified experimentally.[27] The indirect transition at $\Gamma \rightarrow$ K-Γ is shown by an absorption/reflectance observed to the red of the A exciton peak and extending out to 950 nm. These general features of these peaks are in

good agreement with previously reported results and confirming that the NFs presented here

show properties that are characteristic of their bulk form.[27]
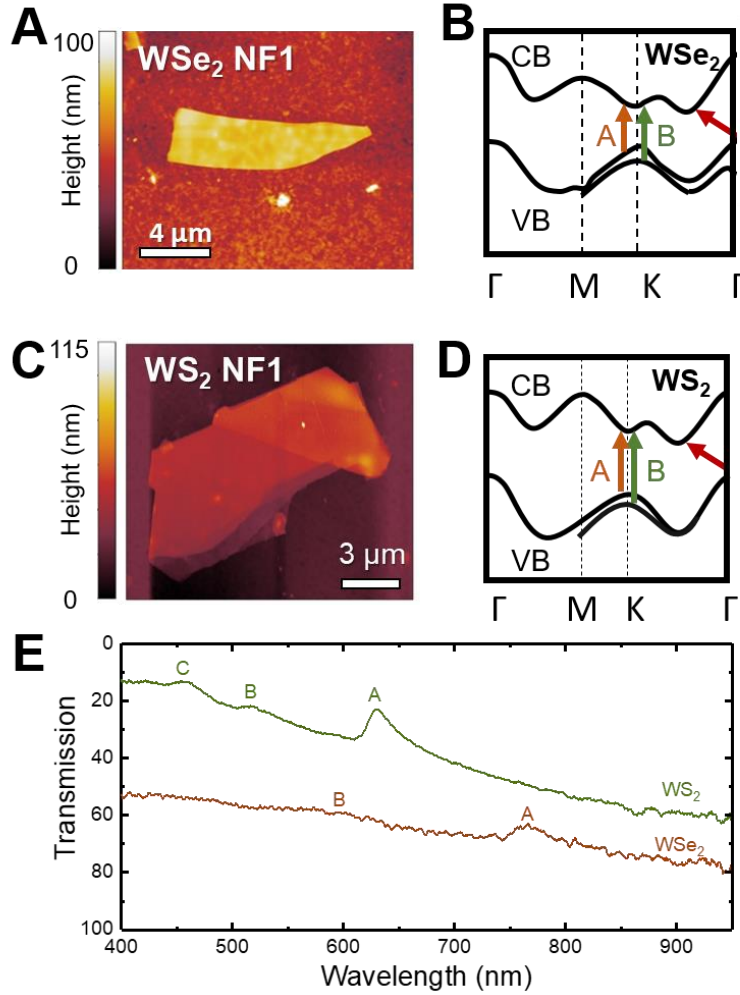
Figure 4.2: Band structure of TMDCs (A) AFM image of WSe_2 NF1 obtained in tapping mode. **(B)** Band diagram of bulk WSe_2. The red arrow shows the indirect bandgap transition and the orange and green arrows the A and B exciton transitions, respectively. Adapted from ref #28 **(C)** AFM image of WSe_2 NF1 obtained in tapping mode. **(D)** Band diagram of bulk WS_2. The red arrow shows the indirect bandgap transition and the orange and green arrows the A and B exciton transitions, respectively. Adapted from ref #28 **(E)** Transmission profile of both NFs obtained using MSP. The data was collected over a 2x2 micron area centered on the flake.

As the number of layers in a WX_2 (X= S or Se) crystal are reduced below ~five, the bands at the Γ point get pushed to higher energies, while the bands at K remain unchanged, shifting the bandgap transition. In the extreme case of the crystal being thinned to a monolayer, the WS_2 becomes a direct bandgap semiconductor.[24] Quantum confinement and the resulting change in hybridization between the p orbitals on chalcogenide atoms and the d orbitals on the metal atom alter the band structure with layer number.[29] The conduction-band states at the K-point are mainly due to localized d orbitals on the metal atoms (Mo and W), while the states near the Γ-point are due to combinations of the antibonding p_z-orbitals on the S atoms and the d orbitals on metal atoms.[29, 30] The states near Γ-point have a strong interlayer coupling effect, resulting in the change in electronic structure.[24] As a result in these modifications to the electronic structure by the decreased number of layers, the carriers become confined to a smaller space and yield a TMDC monolayer with distinctly different properties than the bulk crystal.[29] In the work presented here, the TMDC nanoflakes retain the bulk like electronic characteristics.

Spatially-overlapped pump-probe measurements on individual TMDC NFs reveal complex transients that have contributions from excitons and free carrier excitation, as well a low-frequency coherence arising from acoustic phonon modes (Figure 4.3A). These specific NFs (denoted WS_2 NF1 and WSe_2 NF1) are ~40 nm thick and are typical of the structures studied here. The pump pulse excites an ~400 nm segment of the 10-20 μm wide NF at the location indicated by the black circles (Figure 4.3B and 4.3C), promoting electrons from the VB to the CB with a carrier density of ~10^{20} cm^{-3}. In these experiments, the 425 nm pump is resonant with the C exciton band in WS_2. While in WSe_2, the nonresonant optical excitation by the pump pulse results in the indirect formation of excitons from unbound electrons and

holes that are excited significantly above the band gap. The 850 nm probe interrogates the

indirect bandgap in WS_2, but is resonant with the A exciton in WSe_2.[1-3] The photogenerated

carriers alter the absorption and/or scattering properties of the TMDC NFs causing the initial

change in the probe intensity (positive-going and negative-going signals for WS_2 and WSe_2,

respectively), which decays as the excitons undergo relaxation through higher-order

pathways (*i.e.* exciton-exciton annihilation). The long-lived negative-going signal in both

materials arises from recombination of the photogenerated carriers that decay via a first-order

pathway.
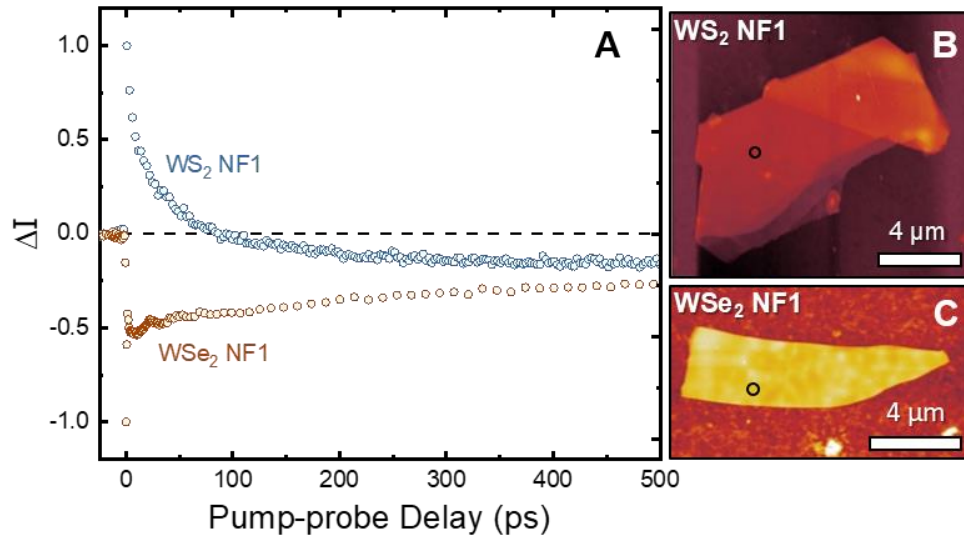
Figure 4.3: Charge Carrier Dynamics in WS₂ and WSe₂ NFs. (A) Transients collected
following localized excitation on WS_2 NF1 (blue) and WSe_2 NF1 (orange) **(B)** AFM images
of the WS_2 showing the location of pump excitation as a black circle; scale bar, 4 μm. **(C)**
WSe_2 NFs showing the location of pump excitation as a black circle; scale bar, 4 μm.

The transient dynamics of WSe_2 show time-dependent coherent oscillations

superimposed on the exciton and free carrier contributions. The relaxation of photoexcited

carriers that are excited significantly above the band gap rapidly deposit their excess energy as heat as they relax to the band edge, which in turn, applies elastic stress to the lattice through thermal expansion. This is likely the physical origin of the impulsively excited low-frequency vibration.[31-33] The periodic vibrational motion modulates the transient signal through strain-induced changes in the band structure or changes in refractive index. Further analysis of the acoustic phonon modes in WS_2 and WSe_2 is discussed in Chapter 5.

4.3.2. Power Dependence

Pump-probe transients were collected in the interior of a WS_2 NF1 in both transmission mode (Figure 4.4A) and reflection mode (Figure 4.4B) with pump pulse energies ranging from 3-23 pJ/pulse. The location the transients were collected in both modes is marked by a blue circle in the inset. In transmission mode, excitation with a 5 pJ pump pulse (orange trace) initially results in a photoinduced transparency (positive-going signal) that rapidly decreases, revealing a long-lived absorptive (negative-going signal) component. These features indicate that there are at least two distinct excited state phenomena/species contributing to the signal. Transients collected at higher pump pulse energies (9 pJ/pulse, dark brown; 17 pJ/pulse, dark blue; 23 pJ/pulse, light blue) show the photoinduced transparency decays faster with increasing pump pulse energy compared to the 5 pJ/pulse (orange) transient. This suggests that the short-lived species decays with higher-order kinetics. Increasing the pump pulse energy doesn't alter the kinetics of the long-lived signal, as indicated by the negative-going signals overlaying at delays longer than 600 ps. This is telling of the long-lived species decaying with first-order (or pseudo-first-order) kinetics. Considering that the pump is exciting directly into the C exciton band, the excited

state species interacting with the probe are excitons that decay with second-order kinetics and free carriers (formed either by direct excitation or dissociation of excitons) that decay through a first-order pathway.

Figure 4.4: Power studies on WS₂ NF. Dynamics measured in transmission and reflective
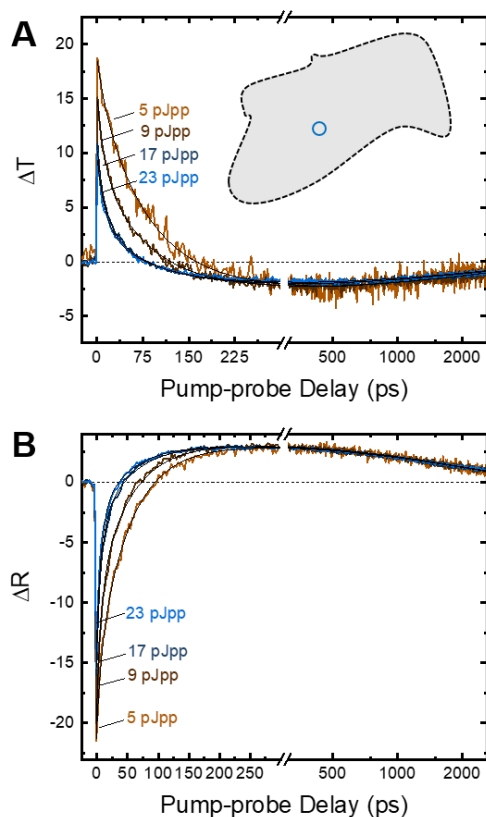
modes with pump energies of 5 pJ/pulse (light orange), 9 pJ/pulse (brown), and 17 pJ/pulse (navy), and 23 pJ/pulse (light blue). The transients are normalized to the signal at 2600 ps. **(A)**Transients collected in transmission mode showing data out to 300 ps, whereas **(B)** shows the same transients collected in transmission mode plotted out to 1500 ps. **(C)** Transients collected in reflection mode showing data out to 300 ps, whereas **(D)** shows the same transients collected in reflection mode plotted out to 1500 ps.

　　　　In reflection mode, excitation with a pump pulse energy of 5 pJ/pulse (orange trace) initially results in a photoinduced transparency (negative-going signal) that rapidly decays, revealing a long-lived reflective (positive-going signal) component. The signal rapidly

increases and switches sign by 125 ps, signifying the sample is now reflecting more probe light in the presence of the pump. The positive signal continues to increase until 300 ps after which it slowly decays back towards zero. Like in the transients collected in transmission mode, these features indicate that there are at least two distinct excited state phenomena/species contributing to the signal. Transients collected at higher pump pulse energies (9 pJ/pulse, dark brown; 17 pJ/pulse, dark blue; 23 pJ/pulse, light blue) show similar features to those collected at 5 pJ/pulse (orange). However, increasing the pump energy shortens the exciton lifetime, while the free carrier relaxation remains independent of pump power. The ultrafast signal coming from both the reflected and transmitted probe is dominated by changes in the refractive index of the WS_2 due to the presence of photoexcited free carriers and excitons.

All 11 transient signals (of which, 4 are shown) in the transmission (reflection) mode power study can be fit to a superposition of a positive (negative) going signal that decays with biexponential kinetics (τ_1, τ_2), and a smaller negative (positive) going signal with a much slower decay time (τ_3) described by the following expression:

$$\Delta T(R)(\Delta t) = A_1 \, exp\left(-\Delta t/\tau_1\right) + A_2 \, exp\left(-\Delta t/\tau_2\right) + A_3 \, exp\left(-\Delta t/\tau_3\right) \qquad [4.1]$$

where the first two terms correspond to the loss of the exciton population and the third to free carrier recombination within the probe spot, respectively. The exciton and free carrier lifetimes (τ_{avg} and τ_3, respectively) were determined through simultaneous fitting of 11 transients to Eqn 4.1. The fit was constrained by sharing τ_1, τ_2, τ_3 between all the transients in each power study, leaving the only adjustable parameter in the global fit to be the relative amplitudes of each exponential decay term. The results of the fits are shown in Table 4.1.

Table 4.1. Parameters Used To Fit WS$_2$ Kinetics Derived from Pump-Probe Microscopy to a Sum of Three Exponentials, $\Delta I(t) = A_1e^{-\Delta t/\tau_1} + A_2e^{-\Delta t/\tau_2} + A_3e^{-\Delta t/\tau}$

	Pump Energy (pJ/pulse)	τ_1 (A$_1$)	τ_2 (A$_2$)	τ_3 (A$_3$)	$\tau_{avg}{}^\alpha$
Transmission Mode	5	12 ps (2.3)	81 ps (19.1)	2650 ps (-2.8)	**51 ps**
	9	12 ps (6.3)	81 ps (11.7)	2650 ps (-2.8)	**28 ps**
	17	12 ps (6.6)	81 ps (6.4)	2650 ps (-2.4)	**21 ps**
	23	12 ps (6.1)	81 ps (5.8)	2650 ps (-2.3)	**21 ps**
Reflection Mode	5	7.4 ps (-4.9)	54 ps (-18.4)	1990 ps (3.4)	**23 ps**
	9	7.4 ps (-8.7)	54 ps (-12.7)	1990 ps (3.5)	**15 ps**
	17	6.2 ps (-6.8)	54 ps (-7.4)	1990 ps (3.4)	**12 ps**
	23	6.5 ps (-7.8)	54 ps (-6.2)	1990 ps (3.4)	**11 ps**

$^\alpha$*Average decay time for the two fast components, i.e., $(1/\tau_{Avg}) = [(A_1/\tau_1)+(A_2/\tau_2)]/(A_1 + A_2)$*

The average exciton relaxation lifetime is determined by averaging together the two fast components in the sum of three exponential fit function and weighting the lifetimes (τ_1 and τ_2) by their respective amplitudes (A_1 and A_2). A 51 ps τ_{avg} was determined for 5 pJ/pulse compared to 21 ps when the pump pulse energy was increased to 23 pJ/pulse in transmission mode, while reflection mode showed a τ_{avg} of 23 ps and 11 ps at 5 pJ/pulse and 23 pJ/pulse, respectively. In both transmission and reflective power studies, the free carrier recombination lifetime is independent of pump power. The transient absorption and transient reflectivity dynamics observed at a 5 pJ/pulse and 23 pJ/pulse pump energies exhibit different exciton decay lifetimes. Increasing the pump pulse energy from 5 pJ to 23 pJ (in both transmission and reflection modes) reduces the exciton relaxation lifetime (τ_{avg}) by ~2x, while the free carrier lifetime remains independent of pump power. The free carrier lifetime is slightly different in transmission and reflection modes; $\tau_3 = 2000$ ps (transmission mode) versus 2700 ps (reflective mode). Monitoring the excited state dynamics in transmission mode averages the exciton and free carrier population kinetics over many NF layers, while the traces collected in reflection mode only report on the dynamics in the surface layers. This could account for the difference between the exciton and free carrier lifetimes measured between the two power studies.

Plotting the relative pump-probe signals at Δt_{0ps} as a function of the relative pump pulse energy reveals a linear increase in the transmitted (black) and reflected (blue) probe (Figure 4.5). Each transient was scaled by dividing the raw signal amplitude by the raw amplitude of the transient collected at the lowest pump pulse energy. The relative pump energies were determined by dividing the experimental pump pulse energy (3-23 pJ/pulse) by the magnitude of the lowest pump pulse energy (3 pJ/pulse) used in the power study. This

linear trend shows that the probe is monitoring single photon excitation and that we are not in a saturation regime.

Figure 4.5: Details of the pump-probe power dependence study for WS$_2$ NF1. The relative pump-probe signal amplitude at t_0 as a function of relative pump pulse energy. The data was collected in both transmission (shown in black) and reflection (shown in blue) mode.

Pump-probe transients were collected in the interior of WSe$_2$ NF2 at pump pulse energies ranging from 0.75-10 pJ/pulse (Figure 4.6). Figure 4.6A shows the transients normalized to the signal at 0 ps. Excitation at the lowest pump pulse energy (0.75 pJ/pulse) initially results in a negative-going signal that corresponds to increased probe absorption (or scattering) through the sample (Figure 4.6, orange). During the first 2 ps of pump-probe

delay, there appears a sharp negative going peak, which quickly decays and is followed by a

long-lived negative going signal that slowly relaxes back toward zero.
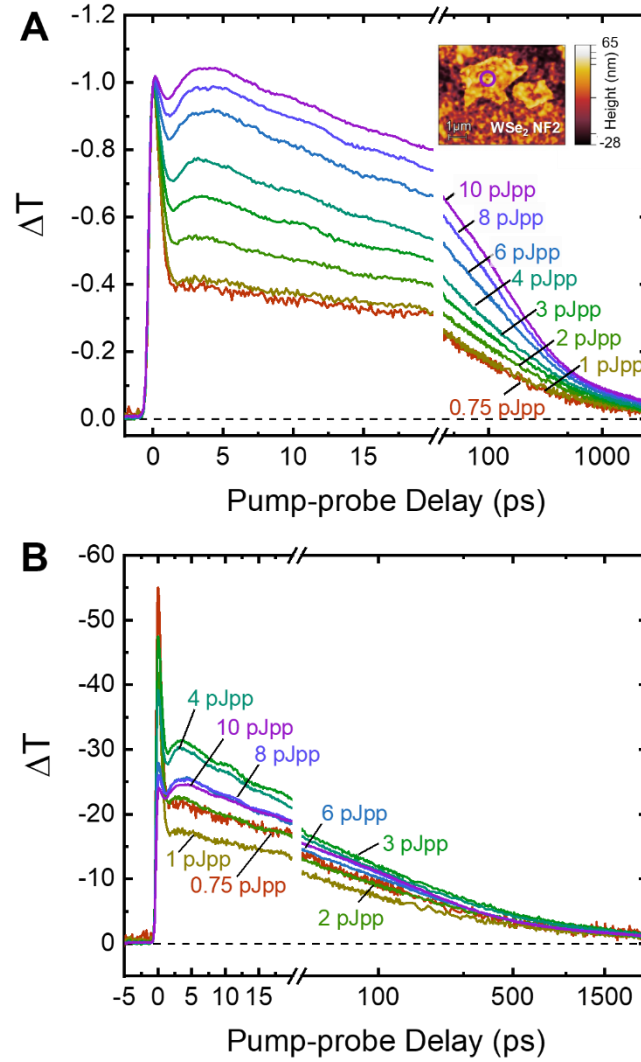
Figure 4.6: Power dependence of WSe$_2$ NF2. Dynamics measured in transmission mode with pump energies of 0.75 pJ/pulse (orange), 1 pJ/pulse (yellow), 2 pJ/pulse (lime green) and 3 pJ/pulse (green), 4 pJ/pulse (teal), 6 pJ/pulse (blue), 8 pJ/pulse (violet) and 10 pJ/pulse (purple). **(A)**The transients are normalized to the signal at 0 ps. Inset is AFM image of ~ 15 nm thick WSe$_2$ NF2 with the circle indicating where the data was collected. **(B)**The transients are normalized to the signal at 2600 ps.

Transients collected at higher pump pulse energies (1 pJ/pulse (yellow), 2 pJ/pulse (lime green) and 3 pJ/pulse (green), 4 pJ/pulse (teal), 6 pJ/pulse (blue), 8 pJ/pulse (violet) and 10 pJ/pulse (purple)) show a similar ultrafast peak as the 0.75 pJ/pulse transient. However, at pump energies above 1 pJ/pulse, there is another feature that grows in over ~5 ps and decays away over hundreds of picoseconds. When the transients are normalized to the signal at 2600 ps (Figure 4.6B), the transients all overlay at delays longer than 1500 ps, indicative of the long-lived species decaying with first order dynamics. The amplitude sharp feature from 0-2 ps could be due to 1) trapping of photocarriers by defect sites, 2) shifting of the A-exciton peak with pump pulse intensity, 3) exciton formation, or 4) nonlinear interactions between the pump and the probe pulses.[2, 3] Increasing the pump pulse energy lowers the relative contribution of the ultrafast peak to the transient signal.

Plotting the relative pump-probe signals at Δt_{0ps} and Δt_{2ps} as a function of the relative pump pulse energy (Figure 4.7) reveals a nonlinear increase of the transmitted probe of the Δt_{0ps} signal (blue), while the Δt_{2ps} signal shows a linear trend (black). Each transient was scaled by dividing the raw signal amplitude by the raw amplitude of the transient collected at the lowest pump pulse energy. The relative pump energies were determined by dividing the experimental pump pulse energy (0.75-13 pJ/pulse) by the magnitude of the lowest pump pulse energy (0.75 pJ/pulse) used in the power study.
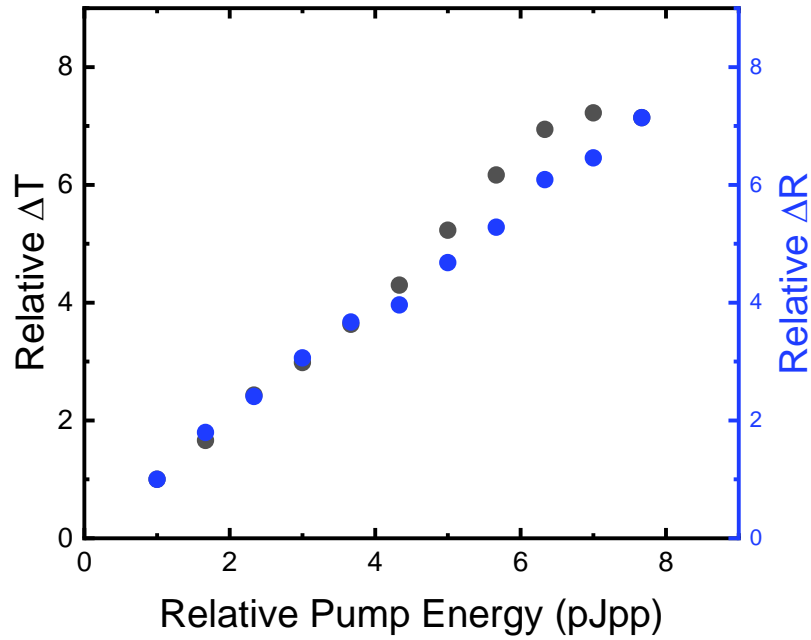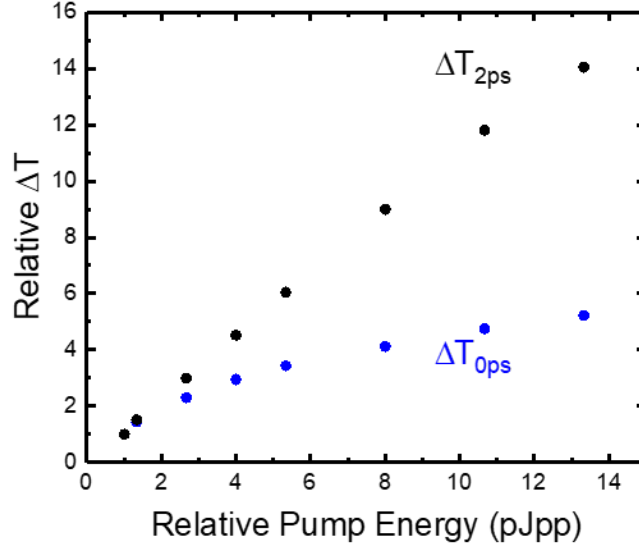
Figure 4.7: Details of the pump-probe power dependence study on WSe₂ NF. The relative pump-probe signal amplitude at 0 ps (ΔT_{0ps}, blue) and 2 ps (ΔT_{2ps}, black) as a function of relative pump pulse energy. The data were collected in transmission mode.

The relative signal intensity at Δt_{2ps} shows the relative pump-probe signal after the ultrafast peak has decayed. Because the relative signal intensity at Δt_{2ps} (ΔT_{2ps}) shows a linear increase with the increasing relative pump pulse energy. This suggests that the loss of the ultrafast signal at Δt_{0ps} (ΔT_{0ps}) is not due to exciton formation.[2] Ceballos and coworkers[2] observed an ultrafast peak in experiments on monolayer WSe₂ that was power independent at carrier concentrations $\sim 10^{11}$ and results from the formation of excitons from injected electron-hole pairs. The fact that our bulk-like WSe₂ NFs ΔT_{0ps} signals display a nonlinear trend indicates that the probe is either monitoring loss of photocarrier population via trap states, the redshift of the A exciton peak or that we are in a saturation regime. The fact that the pump-probe signal at 2 ps (after the loss of the ultrafast peak) shows a linear trend eliminates the possibility of being in a saturation regime. If the rapid loss of the photoexcited

carrier population via trap states is the cause, then the existence of the signal after this fast

process can only be explained if the traps are full and no longer able to capture more carriers.

In regimes where the injected density is much higher than the defect density, only a

negligible fraction of the injected carriers would be trapped and the fast decay component

would be swamped out. The relative intensity of the ΔT_{0ps} signal becomes a small

component of the overall transient dynamics, as is evident in Figure 4.6 and 4.7. This

supports the possibility of defect states trapping photocarriers at low power densities, but as

the carrier population increases at higher pump energies, carriers saturate the trap states.

Further studies are needed to determine if carrier trapping or shifting of the A exciton peak is

the cause for the ultrafast peak. The ultrafast signal that decays within 2 ps after excitation by

the pump pulse and because both the amplitude and kinetics of the pump-probe signal are

power dependent, this makes an analysis of the WSe$_2$ dynamics complex.

4.3.3. Exciton and Free Carrier Dynamics

The charge carrier dynamics were measured within the localized pump spot at the

edge and interior of a WS$_2$ NF and a WSe$_2$ NF using spatially-overlapped pump-probe

imaging. Pump-probe transients were collected at the edge (blue curves) and the interior

(orange curves) of both WS$_2$ NF1 and WSe$_2$ NF1, shown in Figure 4.8A and 4.8B,

respectively. The time-delayed probe pulse monitors the change the photoinduced probe

transparency (ΔT) with pump-probe delay.
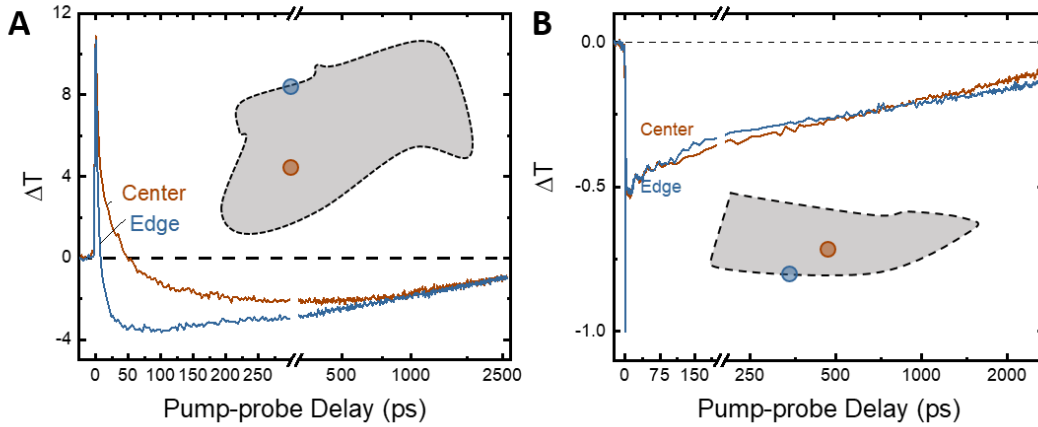
Figure 4.8: Center versus edge dynamics on TMDC NFs. Transmission pump-probe transients collected at the center (orange) and edge (blue) of TMDC NFs. The colored circles in the NF illustration (inset, bottom panel) marks the positions where the data were collected. **(A)** Dynamics on a WS_2 NF1. Transients normalized signal at to 2700 ps. Both transients were taken with a pump energy of 10 pJ/pulse. **(B)** Dynamics on a WSe_2 NF1. Transients normalized to signal at 0 ps. Both transients were taken with a pump energy of 5 pJ/pulse.

There are two differences between the edge and center transients in the WS_2 NF and the WSe_2 NF. In WS_2, the excitons decay more rapidly at the edge than in the center of the NF while the free carrier recombination rate remains unchanged. Whereas in WSe_2, the exciton lifetime is consistent across the NF, but the long-lived negative component relaxes faster in the center than the edges of the NF. Due to the Van der Waals interaction between TMDC layers, the interior has a significantly lower defect density of defects than the edges were dangling bonds are present. These defect sites locally alter the band structure by introducing trap states, providing a lower energy pathway through which these carrier species can relax back to the ground state. This explanation is consistent with the faster exciton decay at the edges of the WS_2 NF.

To better understand how the excited state dynamics vary spatially, SOPP images were collected by scanning the structure across the focal point of the pump and probe pulses and monitoring the transient signal at a fixed time delay. The SOPP image at Δt_{0ps} (Figure 4.9A) shows a photoinduced transparency across the WS_2 NF. The magnitude is largest near the edges, while the interior shows a lower but mostly uniform signal across the interior of the NF as the excitation is moved further from the edges. However, the same image (Figure 4.9B) on the WSe_2 NF reveals a mostly uniform photoinduced absorption (or scattering) across the NF surface. Comparison of SOPP images collected at a series of delays demonstrates that the relaxation rate is nearly uniform across the WS_2 and WSe_2 NF interiors. The edges of the WS_2 NF shows a significant increase in the exciton relaxation rate, whereas WSe_2 shows faster free carrier recombination in the late pump-probe delay images.
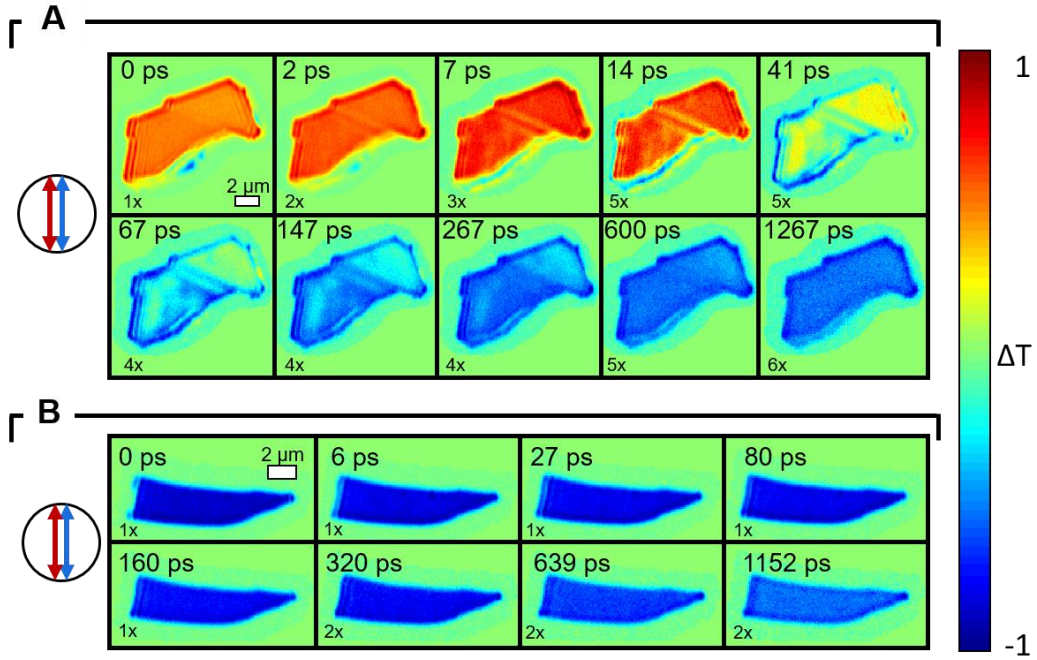
Figure 4.9: Time-resolved measurements with spatially overlapped pump-probe microscopy of WS$_2$ NF1 and WSe$_2$ NF1. Spatially-resolved transient absorption images collected at various pump-probe delays for WS$_2$ and WSe$_2$ NFs. The pump and probe polarization are oriented parallel to the short NF axis (vertical with respect to images). Each image (scale bar 2 μm) is depicted using a normalized color scale with the relative amplitudes indicated by the scaling factors at the bottom left of each image. **(A)** WS$_2$ NF1 **(B)** WSe$_2$ NF1

Transient scans collected in both the edge and interior regions of NF1 (Figure 4.8A and 4.8B) support this conclusion, as there is a significant difference in carrier lifetime in these areas. SOPP imaging on both NFs also reveals a periodic modulation in the transient signal near the flake edges; referred to as a fringe pattern and is present out to ~600 ps. Similar fringe patterns have been observed in MoS$_2$, MoSe$_2$, WSe$_2$, WS$_2$ and are due to polaritons. [34-36]
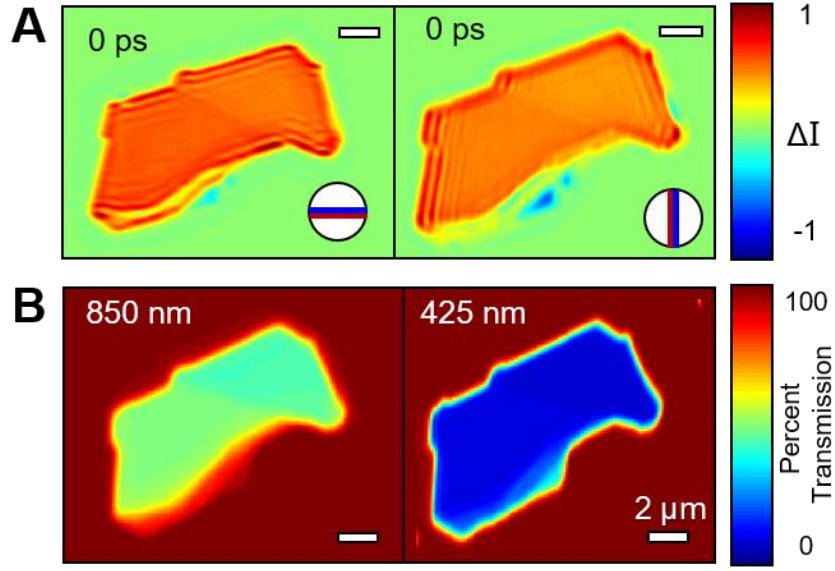
Figure 4.10: Polarization dependence of WS$_2$ NF1 (A) SOPP images of WS$_2$ at parallel and perpendicular probe polarization while the pump is oriented parallel to the long NF axis (horizontal with respect to images, left) or the short NF axis (vertical with respect to images, right). Each image (scale bar 2 μm) is depicted using a normalized color scale. **(B)** Transmission images of WS$_2$ NF1 with the probe (left) and pump (right). Both images (scale bar 2 μm) are depicted using a percent transmission color scale.

Figure 4.10A shows SOPP images collected at various pump and probe polarizations in transmission mode. When the pump and probe beams are oriented parallel to each other and the long axis of the NF, the initially formed excited state (0 ps) shows periodic spatial modulation in the pump-induced change in probe transmission (Figure 4.10A, left image). Rotating the pump and probe polarizations to being parallel to each other and to the short edge of the NF (Figure 4.10A, right image), the fringe pattern appears parallel with the long edge. However, diffraction-limited transmission images taken at the pump (425 nm) and probe (850 nm) wavelength (Figure 4.10B) reveal uniform transmission across the structure.

The fringe phenomena observed in the pump-probe imaging experiment is due to excited state processes.

The fringe pattern could either arise from spatial heterogeneity in the NF surface (*i.e.* changes in NF thickness, grain boundaries, and defect sites) or the result of exciton-polariton formation.[35-37] An AFM image (Figure 4.11C) and height profiles (Figure 4.11D) were collected of the NF and compared to high-resolution spatial profiles (Figure 4.11B) of the fringe pattern over two sections of the SOPP image of WS_2 NF1 (Figure 4.11A).
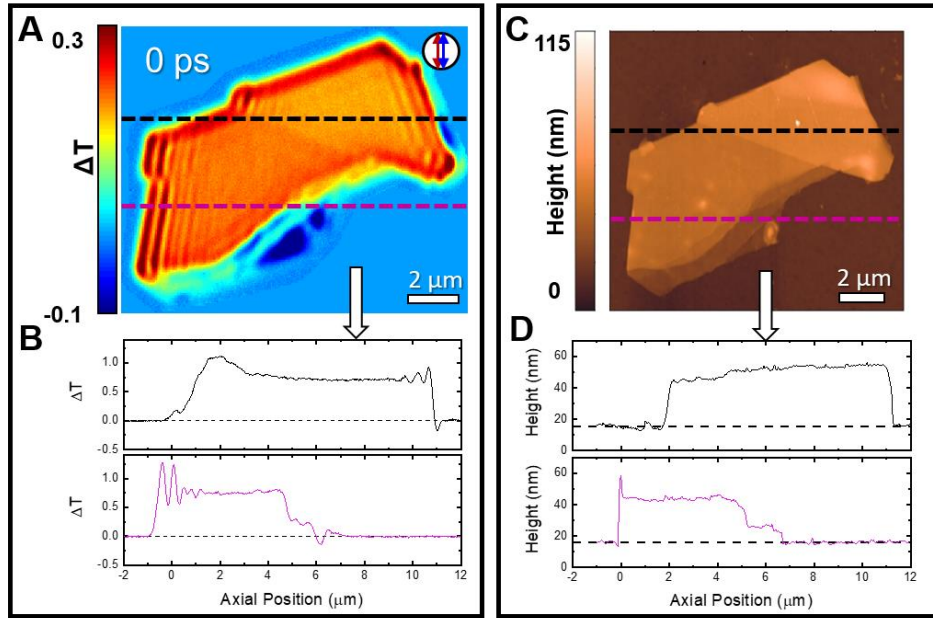
Figure 4.11: Exciton-polariton spatial dependence (A) Pump-probe image of WS_2 NF1 taken at 0 ps delay. The pump and probe are both polarized vertically with respect to the image. **(B)** A horizontal slice of the data from the top (black) and bottom (pink) of the image. The black **(top)** and pink **(bottom)** lines show the location of the slices**. (C)** AFM image with **(D)** horizontal height profiles at the top and bottom of the NF.

Spatial profiles were collected over two regions in WS_2 NF1, as shown in Figure 4.11, by scanning the NF under the pump-probe beams and collecting a SOPP image that is one pixel wide with a high dwell time at pump-probe delays out to 600 ps. The image is then converted with MATLAB code to a plot of the pump-probe (ΔT) intensity versus the axial position; referred to as a spatial profile. The spatial profiles collected over top half of the NF (Figure 4.11B, black) shows periodic modulation in the pump-probe signal a the right side of the NF and a spatial profile from the bottom half of the NF (Figure 4.11B, purple) shows that pattern on the opposite side of the NF. The black and pink dashed lines on the SOPP image (Figure 4.11A) shows the location at which the corresponding black and pink spatial profiles were collected (Figure 4.11B). Comparing these profiles to the height profiles from the same location as the spatial profiles show no periodic change in the NF height in these areas. Thus, the fringe pattern is not the result of structural heterogeneity in the NF surface, but the formation of exciton-polaritons.

The fringes present in the SOPP images are the result of excitons coupling with the probe photons, forming a quasiparticle called an exciton-polariton.[35] The pump pulse excites excitons within a localized area of the NF and the probe interrogates the exciton population within the pump spot. These excitons are strongly confined to the plane within the 2D material, unlike in bulk semiconductors, and experience a reduced screening from their surrounding dielectric environment.[36] The exciton-polariton propagate at the speed of light across the NF surface and reflects off the boundary (NF edges) back toward the probe spot.[38] Because the probe pulse has a temporal width of ~ 100 fs, the polariton can travel ~ 15 μm away from the probe spot, reflect off the NF edge and return to interfere with the remaining probe photons, before the probe pulse has completely passed through the NF. The polariton

forms a standing wave that, depending on the location of the laser pulse relative to the NF, can either constructively or destructively interfere with itself, forming the periodic modulation in the pump-probe signal across the NF surface.[26, 35-39] The farther the pump and probe are from the edge, the longer it takes the exciton-polariton to travel back from the NF boundary, leading to diminishing in the fringe pattern with distance.

4.3.4. Exciton-Polariton Dynamics

SOPP images collected at Δt_{0ps} delays with the pump and probe polarizations oriented parallel to each other in transmission mode, but oriented parallel to either the short (Figure 4.12A) or long axis (Figure 4.12B) of the NF. Each image is depicted using a normalized color scale with the relative amplitudes indicated by the scaling factors in the bottom-left corner of each image. The SOPP images at Δt_{0ps} show a photoinduced transparency across the NF where the magnitude is largest near the edges, while the interior shows a lower but mostly uniform signal across the interior of the NF as the excitation is moved further from the edges. The fringe pattern appears on the edges that are parallel to the pump and probe polarizations. In both NF orientations, the fringe pattern extends ~5 µm from the NF edge.
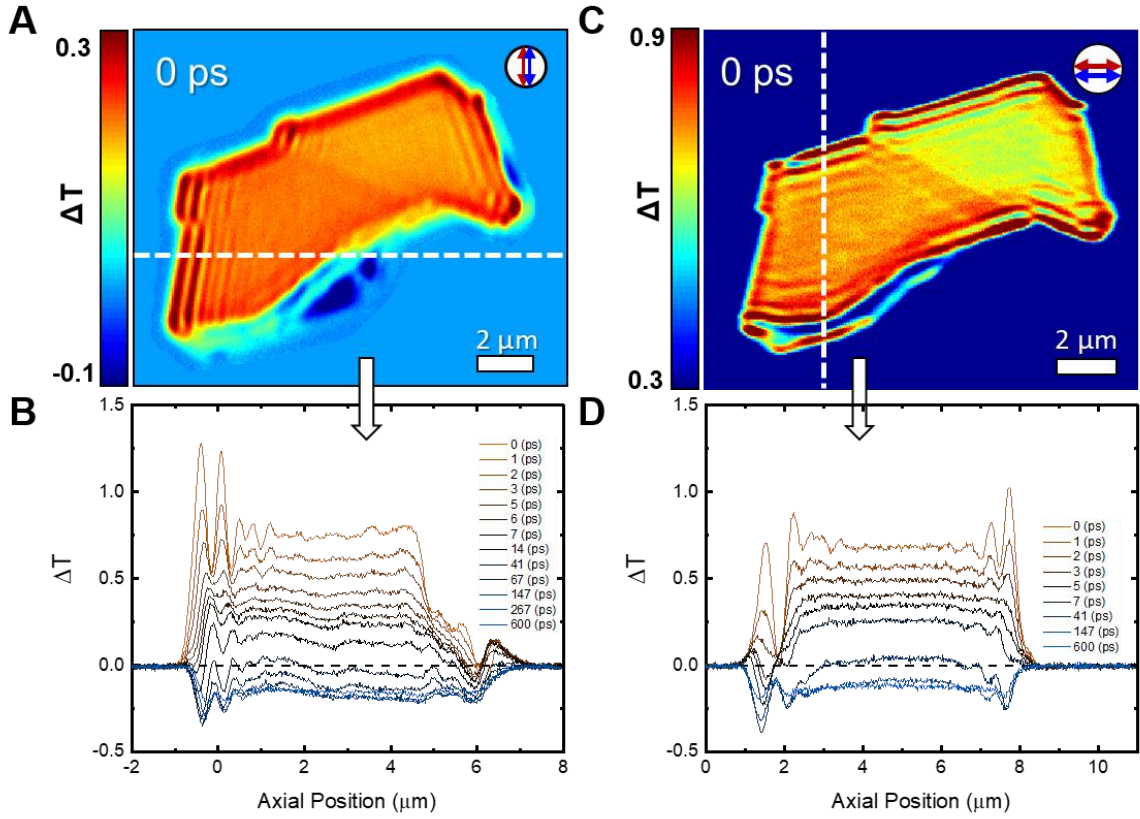
Figure 4.12: Temporal decay of exciton-polariton (A) Pump-probe image of WS$_2$ NF1 taken at a 0 ps delay. The pump and probe are both polarized vertically with respect to the image. The white dashed line indicates where **(B)** Horizontal spatial profiles collected from the top image at various pump-probe delays. **(C)** Pump-probe image of WS$_2$ NF1 taken at a 0 ps delay. The pump and probe are both polarized horizontally with respect to the image. The white dashed line indicates where **(D)** the vertical spatial profiles were collected from the top image at various pump-probe delays.

To determine how the fringes evolve with time, spatial profiles (Figure 4.12C and 4.12D) were collected on WS$_2$ NF1 at various pump-probe delays with the pump and probe beam polarizations oriented parallel to either the short or long axis of the NF. The locations where the spatial profiles were collected are indicated by white dashed lines in the SOPP images (Figure 4.12A and 4.12C). Spatial profiles were collected at pump-probe delays

102

ranging from 0-600 ps and reveal that the amplitude of periodic modulation in the profiles reduces greatly within the first few ps. The periodic modulation in the pump-probe signal lasts out to 600 ps in both NF orientations, similar to what was observed in the time-resolved SOPP images (Figure 4.9). The fringes decay with the short-lived species as the excitons decay[34] and annihilate leaving fewer excitons for the probe photons to couple with, reducing the amplitude of the of the oscillations in the pump-probe signal over the NF.

4.4. Conclusion

The pump pulse photoexcites both short-lived excitons and long-lived free carriers in both tungsten disulfide and tungsten diselenide nanoflakes. The excitons decay through exciton-exciton annihilation (a second order process) within ~200 ps, while the free carriers undergo recombination over ~2-3 ns (a first-order process). Excitons relax faster when they are photoexcited near the edge of the WS_2 NF, compared to excitons generated in the interior of the NF. The edges of TMDC layers have significantly more defects and thus more traps states in the electronic band structure providing lower energy pathways for exciton relaxation. SOPP images of the WS_2 NF also reveal spatial variation in the transmitted probe intensity from changes in NF thickness and the formation of exciton-polaritons. Ultrafast pump-probe microscopy experiments reveal complex transient signals in tungsten diselenide that are the result of photoexcitation of excitons and free carriers. Our power study revealed a nonlinear dependence on pump pulse power suggesting a shifting of the A exciton energy. Further studies on WSe_2 at different probe wavelengths are needed to determine the source of the nonlinear power dependence and a model for exciton relaxation.

REFERENCES

1. Steinleitner, P.; Merkl, P.; Nagler, P.; Mornhinweg, J.; Schüller, C.; Korn, T.; Chernikov, A.; Huber, R., Direct Observation of Ultrafast Exciton Formation in a Monolayer of WSe$_2$. *Nano Lett.* **2017,** *17* (3), 1455-1460.

2. Ceballos, F.; Cui, Q.; Bellus, M. Z.; Zhao, H., Exciton Formation in Monolayer Transition Metal Dichalcogenides. *Nanoscale* **2016,** *8* (22), 11681-11688.

3. Cui, Q.; Ceballos, F.; Kumar, N.; Zhao, H., Transient Absorption Microscopy of Monolayer and Bulk WSe$_2$. *ACS Nano* **2014,** *8* (3), 2970-2976.

4. Ouyang, B.; Mi, Z.; Song, J., Bandgap Transition of 2H Transition Metal Dichalcogenides: Predictive Tuning Via Inherent Interface Coupling and Strain. *The Journal of Physical Chemistry C* **2016,** *120* (16), 8927-8935.

5. Grumstrup, E. M.; Gabriel, M. M.; Pinion, C. W.; Parker, J. K.; Cahoon, J. F.; Papanikolas, J. M., Reversible Strain-Induced Electron-Hole Recombination in Silicon Nanowires Observed with Femtosecond Pump-Probe Microscopy. *Nano Lett.* **2014,** *14* (11), 6287-92.

6. Grumstrup, E. M.; Cating, E. M.; Gabriel, M. M.; Pinion, C. W.; Christesen, J. D.; Kirschbrown, J. R.; Vallorz, E. L.; Cahoon, J. F.; Papanikolas, J. M., Ultrafast Carrier Dynamics of Silicon Nanowire Ensembles: The Impact of Geometrical Heterogeneity on Charge Carrier Lifetime. *J. Phys. Chem. C* **2014,** *118* (16), 8626-8633.

7. Grumstrup, E. M.; Gabriel, M. M.; Cating, E. M.; Pinion, C. W.; Christesen, J. D.; Kirschbrown, J. R.; Vallorz, E. L.; Cahoon, J. F.; Papanikolas, J. M., Ultrafast Carrier Dynamics in Individual Silicon Nanowires: Characterization of Diameter-Dependent Carrier Lifetime and Surface Recombination with Pump–Probe Microscopy. *J. Phys. Chem. C* **2014,** *118* (16), 8634-8640.

8. Mahajan, S., Defects in Semiconductors and Their Effects on Devices. *Acta Mater.* **2000,** *48* (1), 137-149.

9. Cating, E. E. M.; Pinion, C. W.; Christesen, J. D.; Christie, C. A.; Grumstrup, E. M.; Cahoon, J. F.; Papanikolas, J. M., Probing Intrawire, Interwire, and Diameter-

Dependent Variations in Silicon Nanowire Surface Trap Density with Pump-Probe Microscopy. *Nano Lett.* **2017,** *17* (10), 5956-5961.

10.   Cao, L., Two-Dimensional Transition-Metal Dichalcogenide Materials: Toward an Age of Atomic-Scale Photonics. *MRS Bull.* **2015,** *40* (07), 592-599.

11.   Yore, A. E.; Smithe, K. K. H.; Crumrine, W.; Miller, A.; Tuck, J. A.; Redd, B.; Pop, E.; Wang, B.; Newaz, A. K. M., Visualization of Defect-Induced Excitonic Properties of the Edges and Grain Boundaries in Synthesized Monolayer Molybdenum Disulfide. *The Journal of Physical Chemistry C* **2016,** *120* (42), 24080-24087.

12.   Cao, Z.; Harb, M.; Lardhi, S.; Cavallo, L., Impact of Interfacial Defects on the Properties of Monolayer Transition Metal Dichalcogenide Lateral Heterojunctions. *J Phys Chem Lett* **2017,** *8* (7), 1664-1669.

13.   Voiry, D.; Yamaguchi, H.; Li, J.; Silva, R.; Alves, D. C. B.; Fujita, T.; Chen, M.; Asefa, T.; Shenoy, V. B.; Eda, G.; Chhowalla, M., Enhanced Catalytic Activity in Strained Chemically Exfoliated WS_2 Nanosheets for Hydrogen Evolution. *Nat. Mater.* **2013,** *12*, 850.

14.   Cheng, L.; Huang, W.; Gong, Q.; Liu, C.; Liu, Z.; Li, Y.; Dai, H., Ultrathin WS_2 Nanoflakes as a High-Performance Electrocatalyst for the Hydrogen Evolution Reaction. *Angew. Chem. Int. Ed.* **2014,** *53* (30), 7860-7863.

15.   Zhang, Y.; Yan, J.; Ren, X.; Pang, L.; Chen, H.; Liu, S., 2D WS_2 Nanosheet Supported Pt Nanoparticles for Enhanced Hydrogen Evolution Reaction. *Int. J. Hydrogen Energy* **2017,** *42* (8), 5472-5477.

16.   Lukowski, M. A.; Daniel, A. S.; English, C. R.; Meng, F.; Forticaux, A.; Hamers, R. J.; Jin, S., Highly Active Hydrogen Evolution Catalysis from Metallic WS_2 Nanosheets. *Energy & Environmental Science* **2014,** *7* (8), 2608-2613.

17.   Sang, Y.; Zhao, Z.; Zhao, M.; Hao, P.; Leng, Y.; Liu, H., From Uv to near-Infrared, Ws2 Nanosheet: A Novel Photocatalyst for Full Solar Light Spectrum Photodegradation. *Adv. Mater.* **2015,** *27* (2), 363-369.

18.   Vancsó, P.; Magda, G. Z.; Pető, J.; Noh, J.-Y.; Kim, Y.-S.; Hwang, C.; Biró, L. P.; Tapasztó, L., The Intrinsic Defect Structure of Exfoliated MoS_2 Single Layers Revealed by Scanning Tunneling Microscopy. *Scientific Reports* **2016,** *6*, 29726.

19.   Vogel, E. M.; Robinson, J. A., Two-Dimensional Layered Transition-Metal Dichalcogenides for Versatile Properties and Applications. *MRS Bull.* **2015,** *40* (07), 558-563.

20.   Boulesbaa, A.; Huang, B.; Wang, K.; Lin, M.-W.; Mahjouri-Samani, M.; Rouleau, C.; Xiao, K.; Yoon, M.; Sumpter, B.; Puretzky, A.; Geohegan, D., Observation of Two Distinct Negative Trions in Tungsten Disulfide Monolayers. *Phys. Rev. B* **2015,** *92* (11).

21.   Grumstrup, E. M.; Gabriel, M. M.; Cating, E. E. M.; Van Goethem, E. M.; Papanikolas, J. M., Pump–Probe Microscopy: Visualization and Spectroscopy of Ultrafast Dynamics at the Nanoscale. *Chem. Phys.* **2015,** *458*, 30-40.

22.   Gabriel, M. M.; Kirschbrown, J. R.; Christesen, J. D.; Pinion, C. W.; Zigler, D. F.; Grumstrup, E. M.; Mehl, B. P.; Cating, E. E.; Cahoon, J. F.; Papanikolas, J. M., Direct Imaging of Free Carrier and Trap Carrier Motion in Silicon Nanowires by Spatially-Separated Femtosecond Pump-Probe Microscopy. *Nano Lett.* **2013,** *13* (3), 1336-40.

23.   Ramakrishna Matte, H. S. S.; Gomathi, A.; Manna, A. K.; Late, D. J.; Datta, R.; Pati, S. K.; Rao, C. N. R., MoS_2 and WS_2 Analogues of Graphene. *Angew. Chem. Int. Ed.* **2010,** *49* (24), 4059-4062.

24.   Wang, Q. H.; Kalantar-Zadeh, K.; Kis, A.; Coleman, J. N.; Strano, M. S., Electronics and Optoelectronics of Two-Dimensional Transition Metal Dichalcogenides. *Nat. Nanotechnol.* **2012,** *7*, 699.

25.   Xiao, J.; Zhao, M.; Wang, Y.; Zhang, X., Excitons in Atomically Thin 2D Semiconductors and Their Applications. *Nanophotonics* **2017,** *6* (6).

26.   Vasilevskiy, M. I.; Santiago-Pérez, D. G.; Trallero-Giner, C.; Peres, N. M. R.; Kavokin, A., Exciton Polaritons in Two-Dimensional Dichalcogenide Layers Placed in a Planar Microcavity: Tunable Interaction between Two Bose-Einstein Condensates. *Phys. Rev. B* **2015,** *92* (24).

27.   Zhao, W.; Ghorannevis, Z.; Amara, K. K.; Pang, J. R.; Toh, M.; Zhang, X.; Kloc, C.; Tan, P. H.; Eda, G., Lattice Dynamics in Mono- and Few-Layer Sheets of WS_2 and WSe_2. *Nanoscale* **2013,** *5* (20), 9677-83.

28.   Terrones, H.; Lopez-Urias, F.; Terrones, M., Novel Hetero-Layered Materials with Tunable Direct Band Gaps by Sandwiching Different Metal Disulfides and Diselenides. *Sci Rep* **2013,** *3*, 1549.

29.   Zhao, W.; Ghorannevis, Z.; Chu, L.; Toh, M.; Kloc, C.; Tan, P.-H.; Eda, G., Evolution of Electronic Structure in Atomically Thin Sheets of WS_2 and WSe_2. *ACS Nano* **2013,** *7* (1), 791-797.

30.   Klein, A.; Tiefenbacher, S.; Eyert, V.; Pettenkofer, C.; Jaegermann, W., Electronic Band Structure of Single-Crystal and Single-Layer WS_2:Influence of Interlayer Van Der Waals Interactions. *Phys. Rev. B* **2001,** *64* (20).

31.   Cremons, D. R.; Plemmons, D. A.; Flannigan, D. J., Femtosecond Electron Imaging of Defect-Modulated Phonon Dynamics. *Nat Commun* **2016,** *7*, 11230.

32.   Cremons, D. R.; Plemmons, D. A.; Flannigan, D. J., Defect-Mediated Phonon Dynamics in TaS_2 and WSe_2. *Structural Dynamics* **2017,** *4* (4), 044019.

33.   Crut, A.; Maioli, P.; Del Fatti, N.; Vallee, F., Time-Domain Investigation of the Acoustic Vibrations of Metal Nanoparticles: Size and Encapsulation Effects. *Ultrasonics* **2015,** *56*, 98-108.

34.   Fei, Z.; Scott, M. E.; Gosztola, D. J.; Foley, J. J.; Yan, J.; Mandrus, D. G.; Wen, H.; Zhou, P.; Zhang, D. W.; Sun, Y.; Guest, J. R.; Gray, S. K.; Bao, W.; Wiederrecht, G. P.; Xu, X., Nano-Optical Imaging of WSe_2 Waveguide Modes Revealing Light-Exciton Interactions. *Phys. Rev. B* **2016,** *94* (8), 081402.

35.   Hu, F.; Luan, Y.; Scott, M. E.; Yan, J.; Mandrus, D. G.; Xu, X.; Fei, Z., Imaging Exciton–Polariton Transport in $MoSe_2$ Waveguides. *Nature Photonics* **2017,** *11*, 356.

36.   Low, T.; Chaves, A.; Caldwell, J. D.; Kumar, A.; Fang, N. X.; Avouris, P.; Heinz, T. F.; Guinea, F.; Martin-Moreno, L.; Koppens, F., Polaritons in Layered Two-Dimensional Materials. *Nat. Mater.* **2016,** *16*, 182.

37.   Basov, D. N.; Fogler, M. M.; García de Abajo, F. J., Polaritons in Van Der Waals Materials. *Science* **2016,** *354* (6309).

38.   Kang, J.-H.; Wang, S.; Shi, Z.; Zhao, W.; Yablonovitch, E.; Wang, F., Goos-Hänchen Shift and Even–Odd Peak Oscillations in Edge-Reflections of Surface Polaritons in Atomically Thin Crystals. *Nano Lett.* **2017,** *17* (3), 1768-1774.

39.   Liu, X.; Bao, W.; Li, Q.; Ropp, C.; Wang, Y.; Zhang, X., Control of Coherently Coupled Exciton Polaritons in Monolayer Tungsten Disulphide. *Phys. Rev. Lett.* **2017,** *119* (2), 027403.

CHAPTER 5: PROBING COHERENT ACOUSTIC PHONON DYNAMICS IN WS$_2$ AND WSE$_2$ NANOFLAKES

5.1. Introduction

Acoustic phonon dynamics have been extensively characterized in various metal and semiconducting nanostructures with cylindrical and spherical based geometries (*i.e.* nanowires, nanoparticles, etc.), where the frequency of these modes are strongly coupled to the geometry of the system.[1-14] However, less research has been conducted on how phonons behave in layered TMDC materials. Pump-probe experiments performed on transition metal dichalcogenide materials (TMDCs) often reflect a variety of dynamical phenomena, including exciton-exciton annihilation, exciton dissociation, and free carrier recombination, as well as coherent processes arising from impulsive excitation of lattice phonons.[15-17] The structural heterogeneity present in TMDC samples complicates pump-probe signals, making it difficult to interpret them in terms of fundamental physical phenomena.[18, 19] The coherent response arising from impulsive excitation of acoustic phonons is also affected by structural heterogeneity.[20] The slight variation in phonon frequencies due to different NF structural features (thickness, steps, defects, edges, buckles, etc.) gives rise to heterogeneous dephasing that causes the loss of the coherent signal over a few vibrational periods,[21] obscuring the true linewidth.

We have used ultrafast pump-probe microscopy to get around this heterogeneity by performing transient reflection measurements on a single structure with diffraction-limited

spatial resolution. A key feature of our microscope is that both the pump and probe laser pulses are tightly focused, enabling the characterization of transport phenomena in addition to relaxation processes. Measurements performed using a spatially-overlapped pump-probe (SOPP) configuration are analogous to conventional pump-probe spectroscopies, but implemented in a microscopy mode. This configuration allows one to follow the excited state dynamics from different structures, or discrete points within the same structure when an object is larger than the tightly focused pump and probe beams. In addition, through the use of independent scanning mechanisms on the two beams, our microscopy can excite a structure in one location and probe in another, enabling the characterization of transport phenomena. We have used this spatially-separated pump-probe (SSPP) configuration to directly visualize the diffusion of photogenerated carriers,[22] the spread of thermal excitation in Si NWs,[23] charge separation in Si NWs encoded with an axial p-i-n junctions,[24] and propagation of acoustic phonon modes in Ge NWs (as described in Ch. 3) and VO_2 NWs.

Here we report on the application of pump-probe microscopy methods to the study of acoustic phonon dynamics in tungsten disulfide (WS_2) and tungsten diselenide (WSe_2) NFs. Like Ge NWs, the transients obtained from WS_2 and WSe_2 NFs include contributions from charge carrier relaxation and impulsive excitation of acoustic modes. Low-frequency acoustical phonons have been observed in pump-probe experiments of Van Der Waals materials.[15-17, 25] In the vast majority of these examples, the coherent oscillations are only monitored within the initial excitation spot. The pump and probe spots in our experiment, on the other hand, are smaller than the NF size, resulting in phonon excitation in a localized spot of the flake. We observe three characteristic acoustic phonon modes, two of which propagate along the NF. Coherent oscillations with a ~40 ps period are detected at the location of the

pump pulse. We attribute this coherent signal to the excitation of an interlayer breathing mode in the NF.[26] The coherence persists for ~1 ns when the NF is mechanically decoupled from the substrate. We also observe a slow-moving low-frequency acoustic phonon mode. Spatially-separated experiments show that this excitation slowly spreads across the NF surface. Impulsive excitation also creates a shock wave that is observed 1-2 µm away from the pump pulse as it propagates along the NFs.

5.2. Experimental

5.2.1. Sample Preparation

Tungsten disulfide (WS_2) and tungsten diselenide (WSe_2) bulk crystals (commercially acquired from 2D Semiconductor, Inc.) were mechanically exfoliated via the scotch tape method to produced WS_2 and WSe_2 nanoflake samples. A small section of the bulk crystal was exfoliated 11 times and transferred to the etched quartz registry substrates using a small piece of tape, for a total of 12 exfoliations to generate ~40 nm thick NFs. The quartz slide is then placed in an acetone bath for 20 minutes to remove the scotch tape residue from the substrate. A bright field microscope is used to locate individual NFs on the quartz substrate. Atomic force microscopy (AFM) was used to characterize average flake thickness.

5.2.2. Ultrafast Microscope

Pump-probe experiments are performed with a home-built microscope based on a mode-locked Ti: Sapphire laser.[22] The 850 nm laser output is split by a 90:10 beam splitter. The two beams pass through synchronized acousto-optic modulators (AOMs), reducing their repetition rates to 1.6 MHz. The more intense fraction is directed through a β-barium borate (BBO) crystal to generate the 425 nm pump pulse while the lower-intensity component is

used as the 850 nm probe. The probe is quadruple-passed through a 253 mm mechanical stage, providing about 3.3 ns of optical delay. The probe then passes through a set of computer-controlled scanning mirrors that change the angle of the beam as it enters the objective, allowing the probe to be focused to a spatially distinct point on the sample. The two beams are then attenuated using neutral density filters for the pump and probe. They are then recombined using a dichroic mirror and directed onto the back aperture of a microscope objective (100x, 0.8 NA), which focuses the pump and probe beams to 400 nm and 600 nm diffraction-limited spots at the sample. Individual nanostructures are placed within the laser focus using a 2-axis piezo scanning stage. The transmitted probe light is collected by a high NA condenser lens and detected by a balanced photodiode. The pump beam is modulated at 16 kHz and the pump-induced changes in the reflected probe intensity (ΔR) are detected by lock-in amplification. With this microscope, we can measure transient responses of a single nanostructure with ~600 nm spatial resolution and ~500 fs time resolution.[22]

5.3. Results and Discussion

Spatially-overlapped pump-probe measurements on an individual WS_2 NF and WSe_2 NF reveal a complex transient that has contributions from exciton and free carrier excitation, as well as a low-frequency coherence arising from an acoustical phonon mode (Figure 5.1). The pump pulse excites an ~400 nm segment of the 20-30 µm wide NF at the location indicated by the blue circle, promoting electrons from the valence band to the conduction band with a carrier density of ~10^{20} cm^{-3}.[27] The photogenerated carriers alter the absorption and/or scattering properties of the TMDC NFs, causing the initial increase in the transmitted probe intensity (positive-going signal) in WS_2 NF, which decays over time as the excitons

and electron-hole pairs relax and migrate away from the point of excitation. Whereas in WSe$_2$, the photogenerated carriers alter the absorption and/or scattering properties of the NFs, causing the initial decrease in the transmitted probe intensity (negative going signal) in the NF. Given that the pump pulse excites carriers ~1.5-1.7 eV above the band gap, they then rapidly relax to the band edge and heat the lattice in a localized section. The rapid heating applies elastic stress to the lattice generating thermal expansion, which is the likely physical origin of the impulsively excited low-frequency vibrations. The periodic vibrational motion modulates the transient signal through strain-induced changes in the band structure or changes in refractive index,[15] which in turn leads to the time-dependent coherent oscillations superimposed on top of the exciton and free carrier contributions. We determine these low-frequency modes to be a mixture of interlayer breathing, coherent longitudinal, and shear acoustic phonon modes.[15, 16]
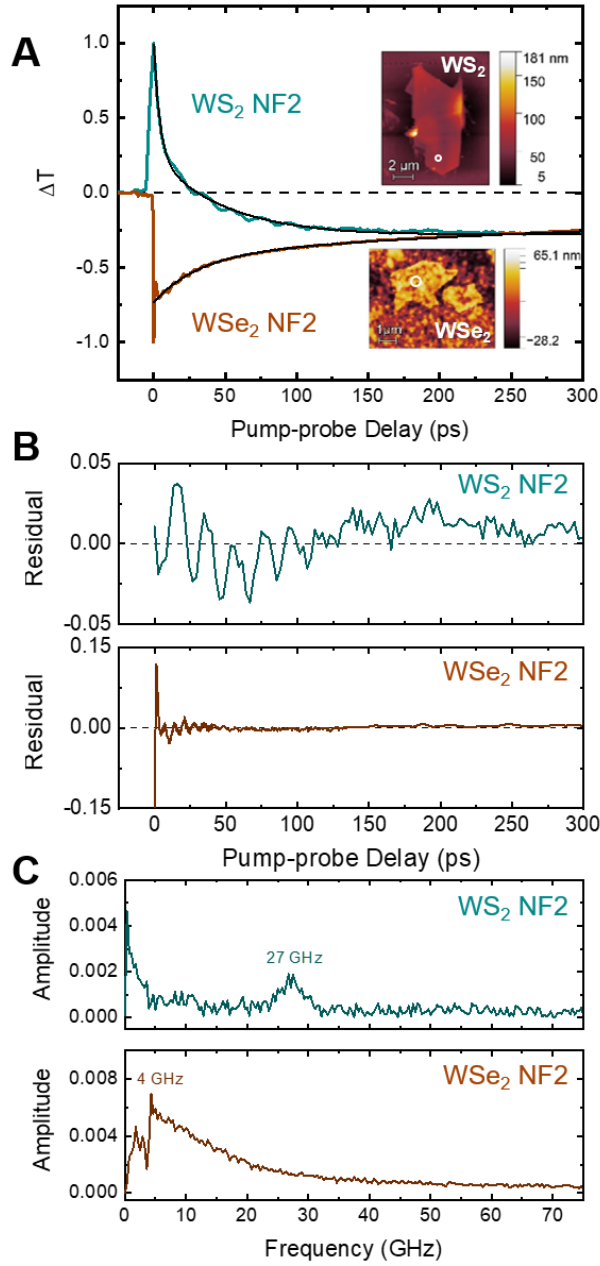
Figure 5.1: Phonon dynamics in WS₂ and WSe₂ NFs. Transients obtained from a typical WS₂ nanoflake (teal) and WSe₂ nanoflake (orange) obtained with a spatially-overlapped configuration. **(A)** The NFs are excited at 425 nm (4 pJ/pulse for WSe₂ NF2, 10 pJ/pulse for WS₂ NF2) at the location of the white circles in the corresponding AFM images (inset) and probed by a delayed 850 nm laser pulse directed at the same location. The black curves are the fit with a sum of three decaying exponential terms. **(B)** Residuals from fitting yields coherent oscillations. The coherences dampen out quickly; before 50 ps (WSe₂ NF2) and 150 ps (WS₂ NF2). **(C)** FFT of residuals yields a frequency of phonons.

5.3.1. Phonon Dynamics

The overall form of the transients depicted in Figure 5.1 (apart from the coherent oscillations) is reasonably well-described by a sum of three decaying exponential terms, i.e.:

$$\Delta I(\Delta t) = A_1 \, exp(-k_1 \Delta t) + A_2 \, exp(-k_2 \Delta t) + A_3 \, exp(-k_3 \Delta t) \qquad [5.1]$$

where the first and second exponential decay terms correspond to the loss of the exciton population (positive-going component in WS_2 and negative-going component in WSe_2), while the third term relates to electron-hole recombination within the probe spot (negative-going component), respectively. We note that in this description, the decay rates (k_1 and k_2) have contributions from exciton loss (*i.e.* exciton-exciton-annihilation, a high-order process) and the free carrier recombination (k_3), and thus, they are only 'observed' rate constants. The observed rate constants for the fits of both WS_2 and WSe_2 NF transient signals are shown in Table 5.1.

Table 5.1. Parameters Used To Isolate Phonon Dynamics in WS$_2$ and WSe$_2$ from Kinetics Derived from Pump-Probe Microscopy to a Sum of Three Exponentials, $\Delta I(t) = A_1 e^{-k1\Delta t} + A_2 e^{-k2\Delta t} + A_3 e^{-k3\Delta t}$

	k$_1$ (A$_1$)	k$_2$ (A$_2$)	k3 (A$_3$)
WS$_2$ NF	(4 ps)$^{-1}$ (0.74)	(51 ps)$^{-1}$ (0.56)	(2613 ps)$^{-1}$ (-0.31)
WSe$_2$ NF	(32 ps)-1 (-0.31)	(347 ps)$^{-1}$ (-0.24)	(1934 ps)$^{-1}$ (-0.18)

Fitting the transients to Eqn 5.1 results in residuals (Figure 5.1B) that isolate the coherent contribution to the pump-probe signals. The oscillations in the WS$_2$ NF dampens out to 150 ps while in WSe$_2$ NF the oscillations only last 50 ps. Fourier transform (FFT) of the residuals yields the phonon frequency spectra depicted in Figure 5.1C. WS$_2$ NF shows an intense frequency component near 27 GHz. However, WSe$_2$ shows a broad feature with a maximum centered at 4 GHz. The resolution of the FFT is limited by the time steps of the pump-probe delay, higher resolution pump-probe transients would be needed to determine if more modes are produced in this NF.
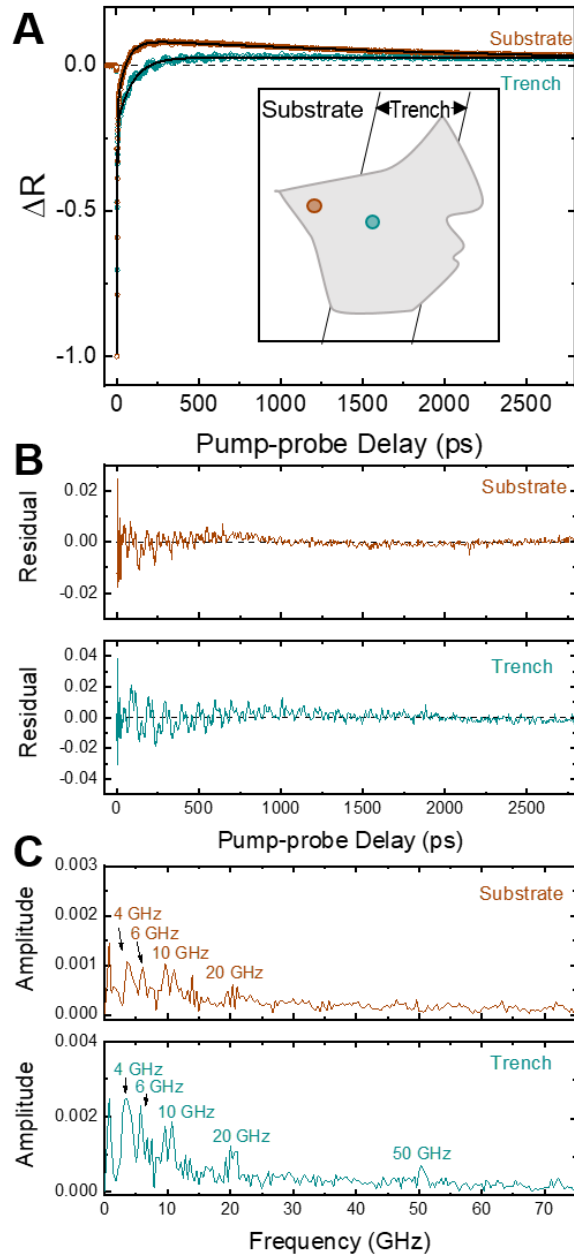
Figure 5.2: SOPP transients of exciton recombination and coherent phonon generation in WSe₂ NF3. **(A)** Inset is a depiction of NF3 with the trench (middle) and substrate (left) visible. The positions at which transient scans were collected are highlighted by teal and orange circles. The top panel shows transient signals corresponding to the suspended (teal) and supported (orange) segments of WSe₂ NF2 with the corresponding fit lines in black. **(B)** Residuals from fitting yields coherent oscillations. Suspended NW section has a lower phonon dampening rate than the section in contact with the substrate. **(C)** FFT of residuals yields a frequency of phonons.

Like previously observed in Ge NWs, the coherence lifetime of the interlayer breathing mode is dramatically increased by mechanically decoupling the NF from the quartz substrate. Shown in Figure 5.2 are SOPP transients obtained by monitoring the pump-induced change in the probe reflection off the NF surface of a ~150 nm thick WSe_2 NF suspended across a 15 µm trench etched into the quartz. Two transients are shown in the Figure, one from the section suspended over the trench and the other from a segment in contact with the quartz substrate (Figure 5.2A, inset). Both transients were fit to Eqn 5.1 and the resulting residuals isolate the coherent contribution (Figure 5.2B). Suspending the NF increases the amplitude of the coherent signal and extends its lifetime by as much as a factor of two compared to the section in contact with the substrate.

Fourier transform (FFT) of the residuals yields the phonon frequency spectra exhibited in Figure 5.2C. Though the FFT spectra are very complex, some clear observations can be made. It is worth mentioning that a complicated spectrum of peaks exists below 10 GHz, some of which can be attributed to the limited temporal window of the transient decay scan. Both sections of the NF show two doublet peaks centered at 5 and 10 GHz and a third frequency component near 20 GHz, indicating that interaction with the substrate does not significantly affect the mode frequency. However, while only three frequency components are observed in the substrate-supported section, the transient collected from the suspended segment also shows a mode at a higher frequency (50 GHz). Ge et. al.,[15] observed a linear dependence on the longitudinal acoustic (LA) phonon mode period and MoS_2 thickness when the material was less than 122 layers thick (~75 nm). Above 122 layers, the material behaves like a bulk material and the oscillation period stays around 30 ps (or 33 GHz). The modes observed at 20 GHz and 50 GHz can be attributed to the interlayer breathing modes,

118

while the modes observed below 10 GHz are due to LA modes of the nanoflake. These results are similar to those observed for bulk semiconducting MoS_2.[15, 26]

The longitudinal acoustic mode frequency is given by:

$$\omega_{LA} = \frac{C_L}{4d} \qquad [5.2]$$

where d is the NF thickness and C_L is the longitudinal speed of sound.[15, 28] Using the frequency from the FFT and NF thickness measurement from AFM images, the speed of sound can be determined for WS_2 and WSe_2.

The photoinduced stress mostly depends on the optical, mechanical, and thermal properties of the material, while the observed frequency of the stress wave created in the lattice is largely governed by geometry (such as film thickness).[28-34] Homogeneous laser excitation where the spot size incident on the film is significantly larger than the film thickness, generates a photoinduced stress and leads to the propagation of LA modes.[28, 30, 35] The pump pulse transfers mechanical energy into the lattice, introducing a plane stress wave that bounces back and forth (in the depth direction) at the interfaces of the thin film sample. The strain in the lattice alters the refractive index of the material, resulting in a periodic modulation in the transmitted (or reflected) probe intensity. Confinement of the vibration is thus dictated by the thickness of the film.

5.3.2. Acoustic Phonon Propagation

Spatially separated pump-probe transients were collected on WS_2 and WSe_2 NFs. The probe was spatially offset from the pump spot at various spatial distances (Δx) across the NF surfaces. With the distances between the pump and probe pulses fixed, the pump-probe delay is scanned to observe the propagation of these acoustic waves. At large enough spatial

separations, such that there is a minimal Gaussian overlap of the pump and probe spots, a wave in the signal emerges corresponding to the arrival of a transverse acoustic pulse.

Tungsten Disulfide

Spreading of the phonon excitation along the tungsten disulfide nanoflake is observed by collecting transients with spatially separated pump and probe beams (Figure 5.3). The experimental geometry is depicted in Figure 5.3A, which shows WS_2 NF2 in contact with the substrate. The pump beam is directed onto the interior of the NF (black circle), impulsively exciting a localized region of the NF. The probe beam (purple circle) is then positioned at a distance (Δx) away, towards the NF edge and the pump-induced change in the reflected probe beam is monitored over time.
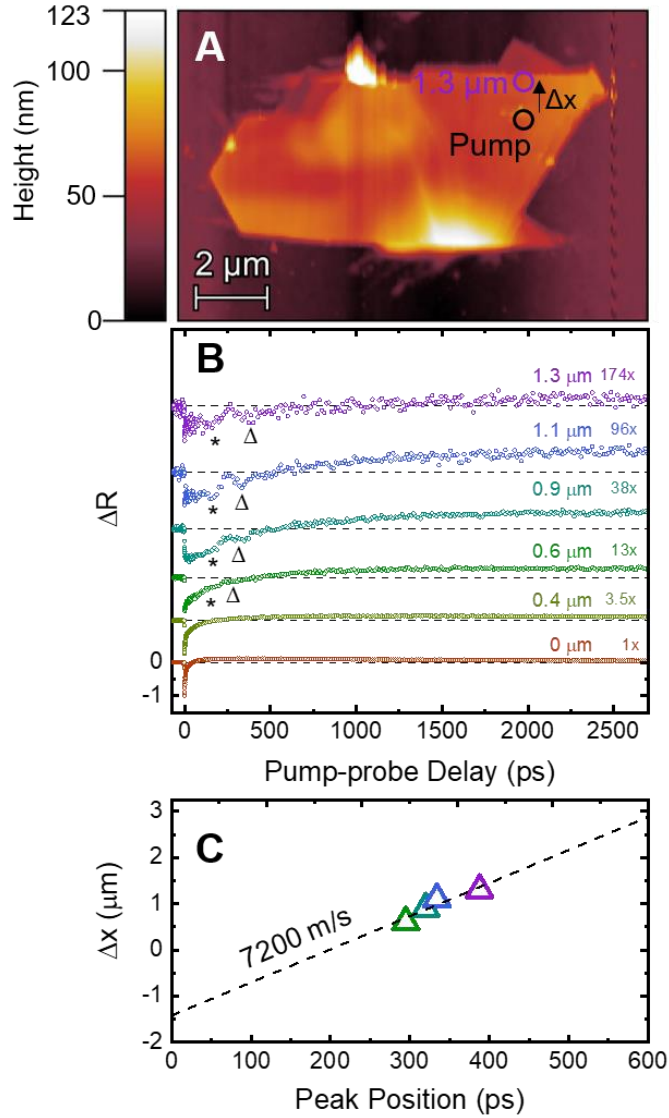
Figure 5.3: SSPP transients of charge-carrier recombination and coherent phonon propagation in WS₂ NF2. (**A**) AFM image of WS$_2$ NF2. The pump spot (black circle) is fixed at the interior of the NF. The probe position is moved across the NF toward the edge from 0-1.3 µm separation (max separation indicated by the purple circle). (**B**) Transients with the pump-probe separation Δx labeled above each curve. Each transient is normalized to its minimum signal with scaling factors with respect to Δx = 0 µm shown to the right. At separations 0.6-.1.3 µm, a low-frequency mode (first peak marked by an asterisk, second peak indicated by a triangle) is observed and grows in over the pump-probe delay. (**C**) The spatial position of the second phonon peak (marked by triangle in 5.3B) is plotted versus pump-probe delay. The slope of the linear fit line (black dashed line) is the propagation speed of the low-frequency mode.

Figure 5.3B shows a series of six transients obtained at increasing separations (Δx) ranging from 0 µm to 1.3 µm, with the farthest probe location marked by the purple circle in the AFM image (Figure 5.3A). The transient obtained when the pump and probe are spatially coincident (Δx = 0) exhibits the same dynamical features (but opposite sign) as the transient observed in Figure 5.1. The shape of the transients changes dramatically as the probe pulse is moved progressively further away from the pump. There is an overall decrease in the pump-probe signal, the magnitude of which is indicated by the scaling factors shown at the right for each transient. Given the spot sizes of the pump and probe beams (400 nm and 600 nm, respectively), there is some residual overlap of the two laser pulses for separations up to about 1.3 µm, which is likely the reason for the observation of signal at Δt = 0 ps.

The series of transients show a broad temporal feature (marked by an asterisk) that is noticeable as a shoulder in the 0.6 µm transient at ~60 ps. This feature is followed by a second recurrence of weaker intensity (marked by the triangle) appearing ~200 ps after the initial peak. The arrival time of these two features increases linearly with pump-probe separation (Figure 5.3C), indicating the transient distortion is moving with a constant velocity. We attribute these two features to the formation of a longitudinal shock wave that propagates along the NW at ~7200 m/s, or about 20% faster than the speed of sound in bulk tungsten disulfide.[36] This is consistent with previous observations of shock wave propagation in Ge NWs.

<u>Tungsten Diselenide</u>

Next, we investigated acoustic phonon propagation in a suspended WSe_2 NF (Figure 5.4), using a spatially separated pump and probe beams as we did with the WS_2 NF above. The pump reflection image of WSe_2 NF3 is shown in Figure 5.4A with a depiction of the experimental geometry. The NF is suspended across a 15 µm wide trench, with the dashed black lines marking the trench boundaries under the flake. The pump beam is directed onto the NF in the center of the trench (black circle), impulsively exciting a localized region of the NF. The probe beam (purple circle) is then positioned at a distance (Δx) away, towards the trench edge and the pump-induced change in the reflected probe beam is monitored over time.
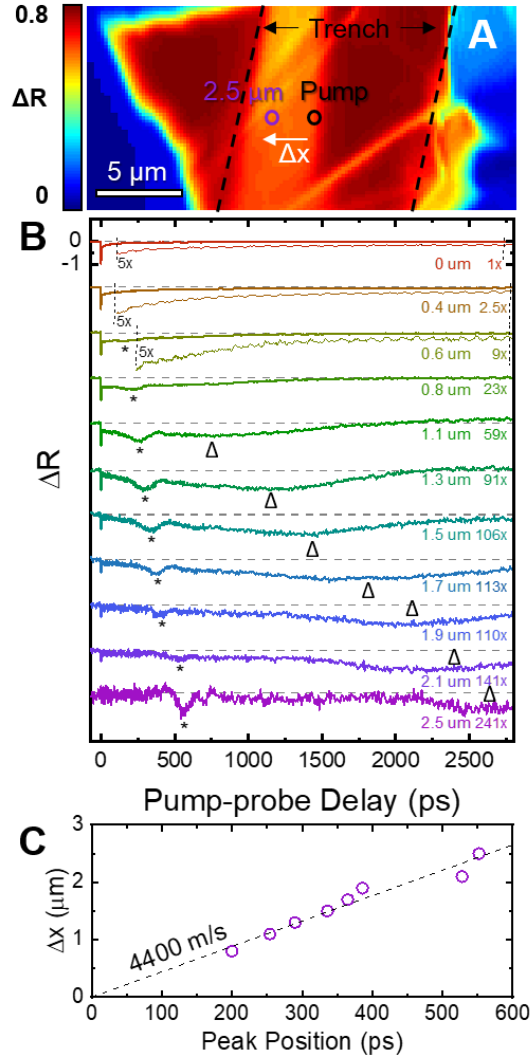
Figure 5.4: SSPP transients of charge-carrier recombination and coherent phonon propagation in WSe2 NF2. (A) Reflection image with the pump pulse (425 nm) of WSe2 NF2. The pump spot (black circle) is fixed at the interior of the NF. The probe position is moved across (left) the NF toward the edge from 0-2.5 μm separation (max separation indicated by the purple circle). **(B)** Transients with the pump-probe separation Δx labeled below each curve. Each transient is normalized to its minimum signal with scaling factors with respect to Δx = 0 μm shown to the right. Two low-frequency modes (first peak indicated by an asterisk, second marked by a triangle) is observed and grows in over the pump-probe delay. **(C)** The spatial position of the fundamental phonon peak (marked by an asterisk in 5.4B) is plotted versus pump-probe delay. The slope of the linear fit line (black) is the propagation speed of the low-frequency mode.

A series of 11 transients are shown in Figure 5.4B, which were obtained at increasing pump and probe separations (Δx) ranging from 0 µm to 2.5 µm. The largest separation is marked by the purple circle in the NF pump reflection image (Figure 5.4A). The transient obtained when the pump and probe are spatially coincident ($\Delta x = 0$) exhibits the same dynamical features as the transient observed in Figure 5.1. Moving the probe pulse further away from the pump spot dramatically alters the shape of the transients. The pump-probe signal at 0 ps decreases dramatically when the probe is separated from the pump so the transients are shown as normalized to -1, with the scaling factors shown at the right for each transient. Given the spot sizes of the pump and probe beams (400 nm and 600 nm, respectively), there is some residual overlap of the two laser pulses for separations up to about 1.3 µm, which is likely the reason for the observation of signal at $\Delta t = 0$ ps.

Unlike the radial breathing mode in Ge NWs, the coherence associated with the interlayer breathing mode does not appear to exhibit a delayed onset when the pump and probe spots are slightly-separated. As the separation of the pump and probe is increased, the amplitude of the high-frequency coherence due to the breathing mode reduces in amplitude. This is most apparent in the 0.6 µm, transient where the coherence shows significant loss of amplitude compared to the SOPP transient. This is indicative of the dilation mode remaining confined mostly within the pump spot.

The series of transients show a shockwave temporal feature (marked by an asterisk) similar to the WS$_2$ NF and Ge NW, which is first noticeable as a small peak in the 0.6 µm transient at ~200 ps. This feature is followed by a second dramatically broader peak of similar intensity (marked by the triangle) appearing ~800 ps after the initial peak. The arrival time of these two features increases linearly with pump-probe separation (Figure 5.4C),

125

indicating the transient distortion is moving with a constant velocity. However, the second peak travels substantially slower than the first, indicating that this is a separate phonon mode being launched from the pump spot. We attribute the first feature to the formation of a longitudinal shock wave that propagates along the NW at ~4400 m/s. The second feature is likely a transverse or shear mode[16, 21, 37, 38] propagating ~10x slower than the shockwave across the NF.
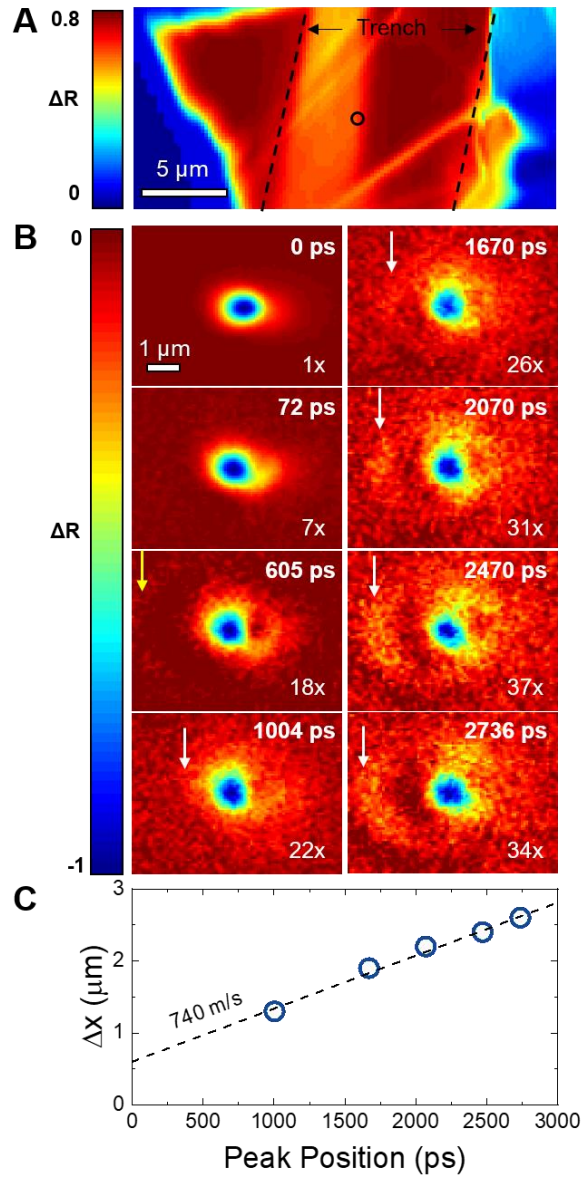
Figure 5.5: Spatially-separated pump-probe images of propagating shear modes. (A) Reflection image collected with the 425 nm pump pulse of a region of WSe$_2$ NF. **(B)** SSPP images were collected with the pump (10 pJ/pulse) held fixed on the position indicated by the black circle on the reflection image. The probe beam (16 pJ/pulse) was scanned across the flake at pump-probe decays indicated in the upper right corner of each frame. Each image is normalized such that minimum negative-going signal corresponds to a value of -1. All images are represented on the same spatial scale (2 μm). **(C)** The plot of wave position from the center of the pump spot (Δx) as a function pump-probe delay (ps) as estimated from (B) and indicated by white arrows. The dashed black line is the linear fit of the peak position vs Δx. The slope (740 m/s) represents an estimation of how mode propagation across the NF.

The assumption that the low-frequency modes are caused by a transverse or shear strain in the lattice is supported by images collected in the SSPP configuration. Figure 5.5 shows a series of SSPP images collected at the same location as in Figure 5.4A using a pump pulse energy of 10 pJ/pulse. These images show the spatial evolution of the charge carrier population and vibration motion across the NF. Each image is normalized such that minimum negative-going signal corresponds to a value of -1. A small amplitude wave is apparent in the 605 ps image, indicated by the yellow arrow that has traveled ~2 μm from the pump spot, corresponding to an approximate velocity of ~4000 m/s. This is consistent with the shockwave observed in the spatially separated transients in Figure 5.4B. Ultrafast electron microscopy experiments show similar results for nanoacoustic wave generation in freestanding WSe_2 nanolayers[1] and flakes.[26] However, this is the first report for direct imaging of acoustic phonon propagation in suspended WSe_2 nanoflakes using ultrafast pump-probe microscopy. By 1670 ps another wave has grown in and continues to propagate outward across the NF. The spatial position of the wave (marked by white arrows in 5.4B) is plotted versus pump-probe delay. The plot shown in Figure 5.5C follows a linear trend where the velocity of wave propagation is estimated by the slope of the linear fit (black dashed line). Here, the slope corresponds to an acoustic wave velocity of 740 m/s, which is comparable to the speed of the low-frequency mode observed in the SSPP transients (marked by triangles in Figure 5.4B).

5.4. Conclusions

Here we measured the acoustic phonon dynamics of tungsten disulfide (WS_2 NFs) and tungsten diselenide nanoflakes (WSe_2 NFs) with diffraction-limited spatial resolution

(~400 nm) and high temporal resolution (~500 fs) using ultrafast pump-probe microscopy. The WS$_2$ and WSe$_2$ NFs are typically 2-25 microns in width and ~40 nm thick. The pump pulse photoexcites both short-lived excitons and long-lived free carriers. Rapid exciton decay impulsively excites the lattice of these TMDC materials generating acoustic phonons. Spatially separated transients monitor the propagation of vibrational motion outside of the initial excitation spot in both WS$_2$ and WSe$_2$ NFs. Time-resolved imaging reveals the propagation of acoustic phonon modes across the NF surface in WSe$_2$ NFs. These results are consistent with previous studies on Ge NWs and the speed of the shock waves in these materials are measured to be ~20% faster than there bulk sound velocities.

REFERENCES

1. Hartland, G. V., Coherent Excitation of Vibrational Modes in Metallic Nanoparticles. *Annu. Rev. Phys. Chem.* **2006,** *57*, 403-30.

2. Jean, C.; Belliard, L.; Cornelius, T. W.; Thomas, O.; Toimil-Molares, M. E.; Cassinelli, M.; Becerra, L.; Perrin, B., Direct Observation of Gigahertz Coherent Guided Acoustic Phonons in Free-Standing Single Copper Nanowires. *J. Phys. Chem. Lett.* **2014,** *5* (23), 4100-4.

3. Kloeffel, C.; Trif, M.; Loss, D., Acoustic Phonons and Strain in Core/Shell Nanowires. *Phys. Rev. B* **2014,** *90* (11).

4. Kolomenskii, A. A.; Jerebtsov, S. N.; Liu, H.; Zhang, H.; Ye, Z.; Luo, Z.; Wu, W.; Schuessler, H. A., Observation of Coherent Acoustic and Optical Phonons in Bismuth Nanowires by a Femtosecond Pump-Probe Technique. *J. Appl. Phys.* **2008,** *104* (10), 103110.

5. Li, Y.; Lim, H. S.; Ng, S. C.; Kuok, M. H.; Ge, M. Y.; Jiang, J. Z., Brillouin Study of Acoustic Phonon Confinement in GeO_2 Nanocubes. *Appl. Phys. Lett.* **2007,** *91* (9), 093116.

6. Lo, S. S.; Major, T. A.; Petchsang, N.; Huang, L.; Kuno, M. K.; Hartland, G. V., Charge Carrier Trapping and Acoustic Phonon Modes in Single CdTe Nanowires. *ACS Nano* **2012,** *6* (6), 5274-5282.

7. Mahmoud, M. A.; O'Neil, D.; El-Sayed, M. A., Shape- and Symmetry-Dependent Mechanical Properties of Metallic Gold and Silver on the Nanoscale. *Nano Lett.* **2014,** *14* (2), 743-8.

8. Mante, P. A.; Lehmann, S.; Anttu, N.; Dick, K. A.; Yartsev, A., Nondestructive Complete Mechanical Characterization of Zinc Blende and Wurtzite GaAs Nanowires Using Time-Resolved Pump-Probe Spectroscopy. *Nano Lett.* **2016,** *16* (8), 4792-8.

9. O'Callahan, B. T.; Jones, A. C.; Hyung Park, J.; Cobden, D. H.; Atkin, J. M.; Raschke, M. B., Inhomogeneity of the Ultrafast Insulator-to-Metal Transition Dynamics of VO_2. *Nat Commun* **2015,** *6*, 6849.

10.   Soavi, G.; Tempra, I.; Pantano, M. F.; Cattoni, A.; Collin, S.; Biagioni, P.; Pugno, N. M.; Cerullo, G., Ultrasensitive Characterization of Mechanical Oscillations and Plasmon Energy Shift in Gold Nanorods. *ACS Nano* **2016,** *10* (2), 2251-8.

11.   Su, M. N.; Dongare, P. D.; Chakraborty, D.; Zhang, Y.; Yi, C.; Wen, F.; Chang, W. S.; Nordlander, P.; Sader, J. E.; Halas, N. J.; Link, S., Optomechanics of Single Aluminum Nanodisks. *Nano Lett.* **2017,** *17* (4), 2575-2583.

12.   Thoen, E. R.; Steinmeyer, G.; Langlois, P.; Ippen, E. P.; Tudury, G. E.; Brito Cruz, C. H.; Barbosa, L. C.; Cesar, C. L., Coherent Acoustic Phonons in Pbte Quantum Dots. *Appl. Phys. Lett.* **1998,** *73* (15), 2149-2151.

13.   Wall, S.; Wegkamp, D.; Foglia, L.; Appavoo, K.; Nag, J.; Haglund, R. F., Jr.; Stahler, J.; Wolf, M., Ultrafast Changes in Lattice Symmetry Probed by Coherent Phonons. *Nat. Commun.* **2012,** *3*, 721.

14.   Wang, L.; Kiya, A.; Okuno, Y.; Niidome, Y.; Tamai, N., Ultrafast Spectroscopy and Coherent Acoustic Phonons of Au-Ag Core-Shell Nanorods. *J. Chem. Phys.* **2011,** *134* (5), 054501.

15.   Ge, S.; Liu, X.; Qiao, X.; Wang, Q.; Xu, Z.; Qiu, J.; Tan, P.-H.; Zhao, J.; Sun, D., Coherent Longitudinal Acoustic Phonon Approaching Thz Frequency in Multilayer Molybdenum Disulphide. *Scientific Reports* **2014,** *4*, 5722.

16.   Cremons, D. R.; Plemmons, D. A.; Flannigan, D. J., Defect-Mediated Phonon Dynamics in TaS_2 and WSe_2. *Structural Dynamics* **2017,** *4* (4), 044019.

17.   Jeong, T. Y.; Jin, B. M.; Rhim, S. H.; Debbichi, L.; Park, J.; Jang, Y. D.; Lee, H. R.; Chae, D. H.; Lee, D.; Kim, Y. H.; Jung, S.; Yee, K. J., Coherent Lattice Vibrations in Mono- and Few-Layer WSe_2. *ACS Nano* **2016,** *10* (5), 5560-6.

18.   Grumstrup, E. M.; Cating, E. M.; Gabriel, M. M.; Pinion, C. W.; Christesen, J. D.; Kirschbrown, J. R.; Vallorz, E. L.; Cahoon, J. F.; Papanikolas, J. M., Ultrafast Carrier Dynamics of Silicon Nanowire Ensembles: The Impact of Geometrical Heterogeneity on Charge Carrier Lifetime. *J. Phys. Chem. C* **2014,** *118* (16), 8626-8633.

19. Cating, E. E. M.; Pinion, C. W.; Christesen, J. D.; Christie, C. A.; Grumstrup, E. M.; Cahoon, J. F.; Papanikolas, J. M., Probing Intrawire, Interwire, and Diameter-Dependent Variations in Silicon Nanowire Surface Trap Density with Pump-Probe Microscopy. *Nano Lett.* **2017,** *17* (10), 5956-5961.

20. Cavalleri, A.; Schoenlein, R. W., Femtosecond X-Rays and Structural Dynamics in Condensed Matter. In *Ultrafast Dynamical Processes in Semiconductors*, Tsen, K.-T., Ed. Springer Berlin Heidelberg: Berlin, Heidelberg, 2004; pp 309-338.

21. Liang, L.; Zhang, J.; Sumpter, B. G.; Tan, Q. H.; Tan, P. H.; Meunier, V., Low-Frequency Shear and Layer-Breathing Modes in Raman Scattering of Two-Dimensional Materials. *ACS Nano* **2017,** *11* (12), 11777-11802.

22. Gabriel, M. M.; Kirschbrown, J. R.; Christesen, J. D.; Pinion, C. W.; Zigler, D. F.; Grumstrup, E. M.; Mehl, B. P.; Cating, E. E.; Cahoon, J. F.; Papanikolas, J. M., Direct Imaging of Free Carrier and Trap Carrier Motion in Silicon Nanowires by Spatially-Separated Femtosecond Pump-Probe Microscopy. *Nano Lett.* **2013,** *13* (3), 1336-40.

23. Cating, E. E.; Pinion, C. W.; Van Goethem, E. M.; Gabriel, M. M.; Cahoon, J. F.; Papanikolas, J. M., Imaging Spatial Variations in the Dissipation and Transport of Thermal Energy within Individual Silicon Nanowires Using Ultrafast Microscopy. *Nano Lett.* **2016,** *16* (1), 434-9.

24. Gabriel, M. M.; Grumstrup, E. M.; Kirschbrown, J. R.; Pinion, C. W.; Christesen, J. D.; Zigler, D. F.; Cating, E. E.; Cahoon, J. F.; Papanikolas, J. M., Imaging Charge Separation and Carrier Recombination in Nanowire p-i-n Junctions Using Ultrafast Microscopy. *Nano Lett.* **2014,** *14* (6), 3079-87.

25. Greener, J. D. G.; Akimov, A. V.; Gusev, V. E.; Kudrynskyi, Z. R.; Beton, P. H.; Kovalyuk, Z. D.; Taniguchi, T.; Watanabe, K.; Kent, A. J.; Patanè, A., Coherent Acoustic Phonons in Van Der Waals Nanolayers and Heterostructures. *Phys. Rev. B* **2018,** *98* (7), 075408.

26. Cremons, D. R.; Plemmons, D. A.; Flannigan, D. J., Femtosecond Electron Imaging of Defect-Modulated Phonon Dynamics. *Nat Commun* **2016,** *7*, 11230.

27. Jellison, G. E., Optical Functions of GaAs, GaP, and Ge Determined by Two-Channel Polarization Modulation Ellipsometry. *Opt. Mater.* **1992,** *1* (3), 151-160.

28. Thomsen, C.; Strait, J.; Vardeny, Z.; Maris, H. J.; Tauc, J.; Hauser, J. J., Coherent Phonon Generation and Detection by Picosecond Light Pulses. *Phys. Rev. Lett.* **1984,** *53* (10), 989-992.

29. Nelson, K. A.; Fayer, M. D., Laser Induced Phonons: A Probe of Intermolecular Interactions in Molecular Solids. *J. Chem. Phys.* **1980,** *72* (9), 5202-5218.

30. Thomsen, C.; Grahn, H. T.; Maris, H. J.; Tauc, J., Surface Generation and Detection of Phonons by Picosecond Light Pulses. *Phys. Rev. B* **1986,** *34* (6), 4129-4138.

31. Othonos, A.; van Driel, H. M.; Young, J. F.; Kelly, P. J., Correlation of Hot-Phonon and Hot-Carrier Kinetics in Ge on a Picosecond Time Scale. *Phys. Rev. B* **1991,** *43* (8), 6682-6690.

32. Zeiger, H. J.; Vidal, J.; Cheng, T. K.; Ippen, E. P.; Dresselhaus, G.; Dresselhaus, M. S., Theory for Displacive Excitation of Coherent Phonons. *Phys. Rev. B* **1992,** *45* (2), 768-778.

33. Maznev, A. A.; Nelson, K. A.; Yagi, T., Surface Phonon Spectroscopy with Frequency-Domain Impulsive Stimulated Light Scattering. *Solid State Commun.* **1996,** *100* (12), 807-811.

34. Othonos, A., Probing Ultrafast Carrier and Phonon Dynamics in Semiconductors. *J. Appl. Phys.* **1998,** *83* (4), 1789-1830.

35. Harb, M.; Peng, W.; Sciaini, G.; Hebeisen, C. T.; Ernstorfer, R.; Eriksson, M. A.; Lagally, M. G.; Kruglik, S. G.; Miller, R. J. D., Excitation of Longitudinal and Transverse Coherent Acoustic Phonons in Nanometer Free-Standing Films of (001) Si. *Phys. Rev. B* **2009,** *79* (9), 094301.

36. Nian, J.; Chen, L.; Guo, Z.; Liu, W., Computational Investigation of the Lubrication Behaviors of Dioxides and Disulfides of Molybdenum and Tungsten in Vacuum. *Friction* **2017,** *5* (1), 23-31.

37.   Torchinsky, D. H.; Johnson, J. A.; Nelson, K. A., Alpha-Scale Decoupling of the Mechanical Relaxation and Diverging Shear Wave Propagation Length Scale in Triphenylphosphite. *J. Chem. Phys.* **2012,** *136* (17), 174509.

38.   Wen, Y.-C.; Ko, T.-S.; Lu, T.-C.; Kuo, H.-C.; Chyi, J.-I.; Sun, C.-K., Photogeneration of Coherent Shear Phonons in Orientated Wurtzite Semiconductors by Piezoelectric Coupling. *Phys. Rev. B* **2009,** *80* (19).

CHAPTER 6: CONCLUSION

6.1. Summary

We have developed a diffraction-limited pump-probe microscope to circumvent the limits of heterogeneity among samples to correlate structural features to ultrafast excited state dynamics on the nanoscale.[1-10] Spatially-overlapped pump-probe microscopy was used to study the distribution of physical properties along different positions within a single nanostructure, demonstrating that ultrafast optical properties can vary between nanostructures as a result of inhomogeneity in geometry and defect concentration. For example, exciton lifetime decreases substantially in WS_2 NFs due to defect sites at the NF edge where dangling bonds are formed. Additionally, in studies of germanium nanowires, we have shown that acoustic phonon modes are generated by impulsive excitation of thermal expansion of the lattice causing localized strain-induced changes in the band structure. The combined spatial and temporal resolution of the pump-probe microscope and its contactless measurement capability make it well-suited to capture the dependence of acoustic phonon frequency on nanowire diameter with high throughput.

Our spatially-separated pump-probe microscope configuration was used to directly visualize transport dynamics in nanomaterials by photoexciting a single structure in one location and probing it in another. Spatially-separated pump-probe experiments on germanium nanowires have enabled direct observation of the evolution of excited charge carriers and thermal energy generated in a localized diffraction-limited spot along the

nanowire axis. In these experiments, we have measured spatial heterogeneity in exciton and free carrier dynamics in tungsten disulfide and tungsten diselenide nanoflakes. We have also demonstrated the relevance and versatility of the microscope and spatially-separated pump-probe configuration by examining coherent acoustic phonon dynamics in germanium nanowires, tungsten disulfide nanoflakes, and tungsten diselenide nanoflakes. We have imaged the spatial evolution of vibrational motion along the axis of germanium nanowires and directly imaged the propagation of coherent acoustic phonon modes along WSe_2 NF.

All of these results collectively establish the necessity of the combination of high spatial and temporal resolution in experimental techniques to examine complex signals that are often obscured in the ensemble measurements. This kind of detailed information regarding optical, electronic, and mechanical properties of individual nanostructures will continue to evolve as materials become more complex.

6.2. Future Directions

While the work outlined in the previous chapters suggests a wealth of information is available to diffraction-limited techniques, the ability to monitor the evolution of the kinetic energy of electrons (not holes, or excitons) to provide insights to the energetics and defect densities in TMDCs is compelling. To this end, others have implemented electron velocity map imaging to monitor the emission of photoexcited electrons from silver nanocubes and gold nanorods.[11, 12] Pump-probe microscopy bridges the gap between the nanoscale and the macroscale and is a powerful tool for characterizing fundamental optical, electronic, and mechanical properties in a variety of complex systems. The use of spatially-resolved microscopies will continue to advance nanotechnologies into the future.

REFERENCES

1.   Gabriel, M. M.; Kirschbrown, J. R.; Christesen, J. D.; Pinion, C. W.; Zigler, D. F.; Grumstrup, E. M.; Mehl, B. P.; Cating, E. E.; Cahoon, J. F.; Papanikolas, J. M., Direct Imaging of Free Carrier and Trap Carrier Motion in Silicon Nanowires by Spatially-Separated Femtosecond Pump-Probe Microscopy. *Nano Lett.* **2013,** *13* (3), 1336-40.

2.   Gabriel, M. M.; Grumstrup, E. M.; Kirschbrown, J. R.; Pinion, C. W.; Christesen, J. D.; Zigler, D. F.; Cating, E. E.; Cahoon, J. F.; Papanikolas, J. M., Imaging Charge Separation and Carrier Recombination in Nanowire p-i-n Junctions Using Ultrafast Microscopy. *Nano Lett.* **2014,** *14* (6), 3079-87.

3.   Grumstrup, E. M.; Cating, E. M.; Gabriel, M. M.; Pinion, C. W.; Christesen, J. D.; Kirschbrown, J. R.; Vallorz, E. L.; Cahoon, J. F.; Papanikolas, J. M., Ultrafast Carrier Dynamics of Silicon Nanowire Ensembles: The Impact of Geometrical Heterogeneity on Charge Carrier Lifetime. *J. Phys. Chem. C* **2014,** *118* (16), 8626-8633.

4.   Grumstrup, E. M.; Gabriel, M. M.; Cating, E. M.; Pinion, C. W.; Christesen, J. D.; Kirschbrown, J. R.; Vallorz, E. L.; Cahoon, J. F.; Papanikolas, J. M., Ultrafast Carrier Dynamics in Individual Silicon Nanowires: Characterization of Diameter-Dependent Carrier Lifetime and Surface Recombination with Pump–Probe Microscopy. *J. Phys. Chem. C* **2014,** *118* (16), 8634-8640.

5.   Grumstrup, E. M.; Gabriel, M. M.; Pinion, C. W.; Parker, J. K.; Cahoon, J. F.; Papanikolas, J. M., Reversible Strain-Induced Electron-Hole Recombination in Silicon Nanowires Observed with Femtosecond Pump-Probe Microscopy. *Nano Lett.* **2014,** *14* (11), 6287-92.

6.   Grumstrup, E. M.; Gabriel, M. M.; Cating, E. E. M.; Van Goethem, E. M.; Papanikolas, J. M., Pump–Probe Microscopy: Visualization and Spectroscopy of Ultrafast Dynamics at the Nanoscale. *Chem. Phys.* **2015,** *458*, 30-40.

7.   Cating, E. E.; Pinion, C. W.; Van Goethem, E. M.; Gabriel, M. M.; Cahoon, J. F.; Papanikolas, J. M., Imaging Spatial Variations in the Dissipation and Transport of Thermal Energy within Individual Silicon Nanowires Using Ultrafast Microscopy. *Nano Lett.* **2016,** *16* (1), 434-9.

8.   Cating, E. E. M.; Pinion, C. W.; Christesen, J. D.; Christie, C. A.; Grumstrup, E. M.; Cahoon, J. F.; Papanikolas, J. M., Probing Intrawire, Interwire, and Diameter-Dependent Variations in Silicon Nanowire Surface Trap Density with Pump-Probe Microscopy. *Nano Lett.* **2017,** *17* (10), 5956-5961.

9.   Mehl, B. P.; Kirschbrown, J. R.; House, R. L.; Papanikolas, J. M., The End Is Different Than the Middle: Spatially Dependent Dynamics in ZnO Rods Observed by Femtosecond Pump–Probe Microscopy. *The Journal of Physical Chemistry Letters* **2011,** *2* (14), 1777-1781.

10.   Mehl, B. P.; Kirschbrown, J. R.; Gabriel, M. M.; House, R. L.; Papanikolas, J. M., Pump-Probe Microscopy: Spatially Resolved Carrier Dynamics in ZnO Rods and the Influence of Optical Cavity Resonator Modes. *J. Phys. Chem. B* **2013,** *117* (16), 4390-8.

11.   Schweikhard, V.; Grubisic, A.; Baker, T. A.; Thomann, I.; Nesbitt, D. J., Polarization-Dependent Scanning Photoionization Microscopy: Ultrafast Plasmon-Mediated Electron Ejection Dynamics in Single Au Nanorods. *ACS Nano* **2011,** *5* (5), 3724-3735.

12.   Grubisic, A.; Ringe, E.; Cobley, C. M.; Xia, Y.; Marks, L. D.; Van Duyne, R. P.; Nesbitt, D. J., Plasmonic near-Electric Field Enhancement Effects in Ultrafast Photoelectron Emission: Correlated Spatial and Laser Polarization Microscopy Studies of Individual Ag Nanocubes. *Nano Lett.* **2012,** *12* (9), 4823-4829.